GRANULAR ELECTRIFICATION ON EARTH AND OTHER WORLDS

A Dissertation
Presented to
The Academic Faculty

By

Joshua Méndez

In Partial Fulfillment
of the Requirements for the Degree
Doctor of Philosophy in the
School of Earth and Atmospheric Sciences

Georgia Institute of Technology

August 2017

GRANULAR ELECTRIFICATION ON EARTH AND OTHER WORLDS

Approved by:

Dr. Dufek, Josef
School of Earth and Atmospheric Science
Georgia Institute of Technology

Dr. Newman, Andrew
School of Earth and Atmospheric Science
Georgia Institute of Technology

Dr. Peng, Zhigang
School of Earth and Atmospheric Science
Georgia Institute of Technology

Dr. Ferrier, Kenneth
School of Earth and Atmospheric Science
Georgia Institute of Technology

Dr. Steffes, Paul
School of Electrical and Computer Engineering
Georgia Institute of Technology

Date Approved: August 20, 2017

To Gran.

ACKNOWLEDGEMENTS

I would like to thank:

Josef Dufek for his guidance, academic freedom, and support these last 6 years

The NSF GRFP and Blue Waters Fellowship programs.

My committee: Andrew Newman, Zhigang Peng, Paul Steffes, and Ken Ferrier

The Dufek Group: Mary Benage, Jenn Telling, Ozge Karakas, Joe Estep, Andrew Gase, Ryan Cahalan, Amelia Winner, Will Guinn, Gabe Eggers, Brena Halverson, Eric Breard, and James Cowlyn

A special thanks to Julian McAdams, whose creativity and skill are matched by few.

Other mentors: (GT) Paul Steffes, Carol Paty, James Wray, Louis Boulanger, Scott Elliot, and James Steinberg. (BU) Ted Fritz, Mark Horenstein, Paul Hall, Bob Kingsland, Malay Mazumder, Colleen Dalton, and Tommaso Toffoli

Friends at GT and Atlanta: Francesco Amato, Hansel Enriquez, Jaime Convers, Ke Qi, Kyle Xu, Steven Mitchell, Gregory Karahalis, and Alex Akins

Val and Chris Harper, who have been second parents to me these past 10 years

George McDonald for his unwavering support, wisdom, and kindness

My parents, who, despite the distance, have always been by my side. A mis padres, quienes a pesar de la distancia, siempre han estado a mi lado.

TABLE OF CONTENTS

LIST OF TABLES

LIST OF FIGURES

LIST OF SYMBOLS

ϵ_o	Permittivity
ϵ_r	Relative permittivity
γ	Townsend coefficient
ϕ	Work function
ρ	Density
σ	Charge density
τ_{RC}	Time constant
A	Area
C	Capacitance
d	Distance
$E_{breakdown}$	Breakdown field
EIR	Electrostatic-to-inertial ratio
F_e	Electrostatic force
g	Gravity
h	Distance
I	Current
K	Overpressure ratio
k	Dielectric constant
k_C	Coulomb's constant
m	Mass
p	Pressure
Q	Charge
r	Radius
t	Time
u_*	Saltation threshold

U_E Electrostatic energy

U_I Electrostatic energy

V Voltage or Volume

SUMMARY

When mobilized, granular materials, both natural and man-made, become electrified through a variety of processes. The phenomena resulting from such charging can be dramatic, as in the case of volcanic lightning, or quite subtle, like when fine ash particles clump together as they fall through the atmosphere. Despite being recognized in a plethora of natural systems, the microphysical processes underlying the electrostatic charging of granular materials still require clarification. In the present work, we experimentally explore electrostatic processes in both terrestrial systems and those on other worlds in our Solar System and beyond. On Earth, we focus on processes occurring in volcanic plumes, some of the most energetic granular flows on the planet. The motivation for this work is to aid in the development of novel tools that use signals from both lightning and slow-tarrying electric fields to monitor and probe the interior of volcanic plumes remotely. The work involving extraterrestrial systems, namely Saturn's moon Titan and the extra-solar world GJ1214b, explores how charging influences the dynamics of non-silicate granular flows and discharge processes in clouds of exotic materials. As a whole, this work demonstrates the diversity of electrostatic phenomena in granular flows and highlights the need for further research to elucidate their fundamental physical frameworks.

CHAPTER 1
INTRODUCTION AND BACKGROUND

1.1 Agenda

In the present work, I will delineate a set of experiments designed to elucidate specific aspects of granular charging in the context of natural processes. The first two thirds of this work will address electrification in volcanic plumes. Chapters 3 and 5 describe links between electrification and the fluid dynamics of ash flows. Chapter 4 describes important differences between triboelectric and fragmentation charging (two principal mechanisms thought to operate in volcanic plumes) in simulated volcanic jets. Finally, chapter 6 will explore fragmentation processes in greater detail.

The last third of this work will delineate electrification process on worlds with either vastly different surface conditions or exotic granular materials. In particular, I first will discuss how the electrification of organic sands on Titan may influence the geormophology of its dunes (chapter 8). I will conclude with a description of experiments elucidating charging processes in the putative salt clouds of GJ1214b, a super-Earth orbiting an M-dwarf star 13 parsecs from Sol (chapter 9).

Chapters 1,2 and 7 will provide the reader with background on both the fundamental physics of granular electrification and the environments being studied.

The present work has its foundations in 6 manuscripts (published, in review, or submitted) prepared during my time at Georgia Tech:

1. Méndez Harper, J., and J. Dufek (2015), *The Electrification of Volcanic Particles during the Brittle Fragmentation of the Magma Column*, Proc ESA Annu. Meet. Electrost. 2015.

2. Méndez Harper, J., and J. Dufek (2016), *The effects of dynamics on the triboelectrification of volcanic ash*, J. Geophys. Res. Atmospheres, 2015JD024275,

doi:10.1002/2015JD024275.

3. Méndez Harper, J., G. D. McDonald, J. Dufek, M. J. Malaska, D. M. Burr, A. G. Hayes, J. McAdams, and J. Wray (2017a), *Electrification of sand on Titan and its influence on sediment transport*, Nat. Geosci.

4. Méndez Harper, J., C. Cimarelli, V. Cigala, U. Kueppers, J. Dufek, and D. Gauidin (2017b), *Differentiating the roles of triboelectric and fractoelectric charging in the generation of volcanic lightning*, In Review.

5. Méndez Harper, J., J. Duefk, C. Cimarelli, R. Thomas, and D. Gauidin (2017c), *Inferring the structure of supersonic volcanic jets from discharge timing and location*, Submitted.

6. Méndez Harper, J. and J. Dufek (2017), *Triboelectrification of KCl and ZnS particles with applications to GJ1214b*, Submitted.

1.2 Electrified grains

The electrification of granular materials is poorly understood, yet most people are familiar with these electrostatic processes to some degree. Indeed, who hasn't opened a package filled with packing peanuts only to find bits of Styrofoam sticking every surface imaginable? Electrostatic phenomena in systems of mobilized granular materials may manifest at the meter (in the case of industrial settings), kilometer (in the case of volcanic lightning), or even megameters (in the case planetary formation through electrostatic aggregation of planitesimals), but they are supported by physical infrastructures with scales smaller than the size of a grain of sand. Indeed, charging must ultimately originate from the exchange and concentration of either electrons or ions. This difference in scales, spanning over 10 orders of magnitude, is certainly one of the reasons why so many aspects of granular electrification remain obscure. Yet, beyond the problem of size, more fundamental questions exist. Here, I enumerate only a few:

Figure 1.1: Spectacular lightning captured during an eruption of Rinjani. Creative Commons License, Oliver Spalt.

1. Why do insulating particles, composed of materials that are devoid of free charges, become electrified when rubbed together?

2. What are the main species being exchanged during particle-particle contacts, electrons or ions?

3. Does frictional electrification involve the fracture or spallation of material?

4. What role does environment play in the electrification of granular substances?

5. How do the dynamics of the granular systems influence their electrostatic behaviors?

Answering all of these questions in a single dissertation would, of course, be impossible. Thus, in the present work I will only address those pertinent to the agenda delineated above.

1.3 Electrification mechanisms for solid particles

1.3.1 Triboelectrification

Although frictional electrification is the oldest manifestation of electricity known to man, it still remains today quite obscure as to the mechanisms active. - Kunkel, 1950. When granular materials are forced to flow in air, colliding particles tend to acquire electric charges (Lowell & Truscott, 1986a) (Lowell & Truscott, 1986b) (Forward, Lacks, & Sankaran, 2009c) (Forward, Lacks, & Sankaran, 2009b) (Kok & Lacks, 2009) (Chen et al., 2014) (Iuga, Calin, Neamtu, Mihalcioiu, & Dascalescu, 2005) (Zhao, Castle, Inculet, & Bailey, 2003) (Moughrabiah, Grace, & Bi, 2012) (Yao, Zhang, Wang, Matsusaka, & Masuda, 2004). In industrial settings, for example, this transfer of charge may result in particles adhering to the walls of containers (Hendrickson, 2006) or forming aggregates. If the particles become sufficiently charged, an electrostatic discharge may occur Lacks and Sankaran, 2011. While tribocharging represents a hazard in some situations (Bartknecht, 2012) (Jones & Tang, 1987) (Glor, Lüttgens, Maurer, & Post, 1989) (Ohsawa, 2003) (Kwetkus, Sattler, & Siegmann, 1992), this process can also be exploited for a number of beneficial applications, such as power coating, particle separation, and self-assembly (Grzybowski, Winkleman, Wiles, Brumer, & Whitesides, 2003)(Horenstein, Mazumder, & Sumner Jr., 2013) (Telko, Kujanpaa, & Hickey, 2007) (Mountain et al., 2001) (Mammino, Johnson, Walters, & Perez, 1980) (Laurentie, Traoré, & Dascalescu, 2013) (Mayr & Barringer, 2006). Additionally, the magnitude of tribocharging can yield important information about granular flows, like particle concentration and flow rates. Experiments have shown that the transfer of charge from one material to another can vary greatly with chemical composition, impact velocity, physical aspects, environmental conditions, and other characteristics (Lacks & Sankaran, 2011). Such variability makes it difficult to assess which parameters most strongly affect charging. Efforts to characterize

contact or tribocharging have often yielded incongruent results. Complications like these have precluded the formulation of a consistent triboelectric model. As stated by Kunkel, 1950, the manner in which electrostatic charge arises is perhaps one of the oldest problems in the history of science.

A number of models exist for particle tribocharging. Here, we discuss three: *the condenser model* , *the trapped electron model*, and *the ion exchange model*. Some of the earlier work on triboelectrification dealt with the charging that occurs when materials of different compositions are either brought into contact or rubbed together. (Lowell & Truscott, 1986b) (Lowell & Truscott, 1986a) Much work has been done in this area because such modality of triboelectrification is present during the transport of particulates, such as pharmaceutical powders or agricultural products flowing through metal or plastic pipes, and, thus, has direct industrial applications (Ndama, Guigon, & Saleh, 2011) (Mazumder et al., 1997) (Kanazawa, Ohkubo, Nomoto, & Adachi, 1995) (Mahi et al., 2015) (Schwindt et al., 2017). Here, charge exchange is governed by the differences in surface work functions between the interacting substances. A material's work function is defined as the energy required to move an electron from a solid surface in vacuum to a point immediately outside said surface. When two surfaces of differing compositions are brought together, a potential difference develops and electrons will flow from the surface with the lower work function ϕ_1 to the one with the higher work function ϕ_2:

$$Q = CV_c = \frac{C(\phi_1 - \phi_2)}{e} \tag{1.1}$$

In Equation 1.1, Q is the amount of charge transferred, C is the capacitance which depends on the geometrical parameters of the contact, V_c is the potential differences arising from the difference in surface work function, and e is the elementary charge. Equation 1.1 suggests that the amount of charge exchanged will depend directly on

Figure 1.2: The polarity of charge acquired by two materials when rubbed together is determined by the difference in their work functions. The triboelectric series organizes materials based on the direction of charge transfer. A material close to the top of the series (say, rabbit's fur) will charge positively when rubbed against one at the bottom (polystyrene, for example), which will charge negatively. Image based on figure from Lacks and Sankaran, 2011

the mismatch between surface work functions. For two surfaces with the same work function this model predicts the charge will be zero, while very large charges can be accumulated on surfaces with wildly different work functions (such as metals and plastics). The triboelectric series (See Figure 1.2) is an empirical effort to categorize how materials will charge under the present model. Substances at the top of the series will become positively charged (that is, they will lose electrons) when rubbed with materials at the bottom of the series (these will gain electrons). Thus, when one rubs a balloon on one's hairy head, the triboelectric series predicts that the balloon will acquire a negative charge while one's hair becomes positively charged.

Condenser Model: Following the treatment by Matsusaka, Ghadiri, and Masuda, 2000, the contact region between two particles is treated like a capacitor (leading to the capacitance C in Equation 1.1. Consider for simplicity the impact of a particle with a plane surface. From Hertz elasticity theory, the contact area, A , and contact duration, Δt are given, respectively, as:

$$A = \pi a^2 \alpha \tag{1.2}$$

$$\Delta t = \frac{2.94}{v}\alpha \tag{1.3}$$

where the rebound coefficient is given as:

$$\alpha = [\frac{4}{5}\pi^2 \rho v^2 (k + k_s)]^{2/5}. \tag{1.4}$$

In the above expression, a is the particle radius, v is the velocity, ρ is the density, and k and k_s are the elasticity parameters for the particle and surface, respectively.

The capacitance, C between the particle and the surface is:

$$C = \frac{\epsilon_o A}{z_o} \tag{1.5}$$

Where, ϵ_o is the permittivity of the medium and z_o is the critical gap needed for charge transfer to occur and is a function of the unknown topography between both bodies. The transferred charge, ΔQ, can be shown to be:

$$\Delta Q = \frac{\pi \epsilon_o V}{z_o} [\frac{4}{5} \pi^2 \rho v^2 (k + k_s)]^{2/5} a^2 (1 - e^{\Delta t/\tau}) \tag{1.6}$$

In the above equation, V is the potential difference between particles and τ is the charge relaxation time of the particle. V is expresses as the following summation:

$$V = V_c - V_b - V_e - V_{ex} \tag{1.7}$$

where V_c is the potential difference arising from the particles' surface work functions ϕ_1 and ϕ_2, V_b is the potential produced by the space-charge induced by nearby particles in the surroundings, V_{ex} the potential from external fields, and V_e comes from image charges. For insulators, τ is very large compared to Δt and we can rewrite Eq. (1.6) as:

$$\Delta Q = \frac{\epsilon_o A V}{z_o} \frac{\Delta t}{\tau} \tag{1.8}$$

Trapped Electron Model: While the model described above works well for granular systems composed of chemically distinct particles, it cannot account for charging in particulate systems of identical composition. Indeed, as I mentioned above, Lacks and Sankaran, 2011, the identical work functions of these chemically-identical particles would inhibit any form of charge transfer. To account for these shortcomings, Lowell and Truscott, 1986a Lowell and Truscott, 1986b have indicated that triboelec-

tric charging in systems of compositionally homogeneous materials may be driven by the exchange of electrons trapped in high-energy states on one surface that migrate to vacant low-energy states on another during repeated collisions. Because, on average, every surface should have the same abundance of high-energy electrons (and vacant low-energy states), one would assume that the both surfaces would lose just as many electrons as they gain. For particles with identical surfaces areas, this situation seems to hold–both surfaces remain electrostatically neutral. However, when a geometrical asymmetry exists between both surfaces, as is the case for a small particle rubbing against a large grain, negative and positive charges become segregated. In particular, the trapped electron model predicts that small grains will charge negatively relative to large grains. A simple game analogy (proposed by Lacks and Sankaran, 2011) is useful in describing how these non-equilibrium states lead to particle-size-dependent charging behavior. To get the game started, you must go out onto the street and recruit a few hundred participants. You take the participants to the large open field at Piedmont Park, asking them to bring 1% of the savings in one dollar bills. This money is kept in their *left* pockets. Once gathered at the park, you blindfold each of the participants and ask them to walk around the field. Each time two participants collide, each person takes one dollar bill from his or her left pocket and gives it to the other person. Received bills are placed in *right* pockets, where they remain for the rest of the game. Atlanta, with a Gini coefficient of 0.57 (comparable to Suriname or the Central African Republic CIA, 2016), has the second highest income inequality of any major US city (Ponczek & Lu, 2016). Thus, some participants will be grotesquely wealthy, while many others will fall well below the poverty line. Regardless of their financial status, no one is ever forced to leave the game. Even when the poor run out of bills in their left pockets, their right pockets can still accommodate dollars. What happens after a few hours of playing this game? 1) The poor quickly deplete their left pockets. However, because they do not leave the game, they not only replenish this

wealth with the dollars collected in their right pockets, but actually receive a net gain of dollar bills. 2) The rich, on the other hand, may not consume all of their left pocket bills (Anne Cox Chambers, the richest person in the state (Forbes, 2016), would only empty her left pocket after 170 million collisions!). Indeed, the rich always give away dollars, but may not always collect money (for instance, during a collision with a poor person with no remaining dollars in his or her left pocket). Thus, over time, the rich suffer a net loss of money. Given the utter failure of neoliberalism (Mason, 2016) (Piketty, Goldhammer, & Ganser, 2014), economists should turn to granular electrostatics for better ideas on wealth redistribution. How does this game relate back to the question of triboelectrification in systems of chemically-identical particles? In this analogy, dollars represent electrons that are transfered during particle-particle collisions, impoverished folks are small particles, and the rich individuals are large grains. We note that while all particles have the same density of trapped electrons, small particles have fewer trapped electrons than large grains because of their smaller surface areas. Just as poor people become enriched with dollar bills, small particles become enriched in electrons (and negative charge) while large grains, like the city's capitalist class, suffer losses (becoming relatively positive). This process is depicted qualitatively in Figure 1.3: Mathematically, the charge exchange process can be described by an electron loss rule (Equation 1.9) and electron receive rule (Equation 1.10):

$$n_i^H(t) = \begin{cases} KA_{ij}\sigma_i^H, & \text{if } n_i^H > 0 \wedge |\sigma(n_i^H, n_i^L, t^+)| \leq \sigma_{max} \\ 0, & \text{otherwise} \end{cases} \tag{1.9}$$

.

$$n_i^H(t) = \begin{cases} KA_{ij}\sigma_j^H, & \text{if } |\sigma(n_i^H, n_i^L, t^+)| \leq \sigma_{max} \\ 0, & \text{otherwise} \end{cases} \tag{1.10}$$

In Equations 1.9 and 1.9, $A_{i,j}$ is the contact area between particles i an j, σ_i^H is the surface density of high energy electrons on particle i, while $\sigma(n_i^H, n_i^L, t)$ is the total

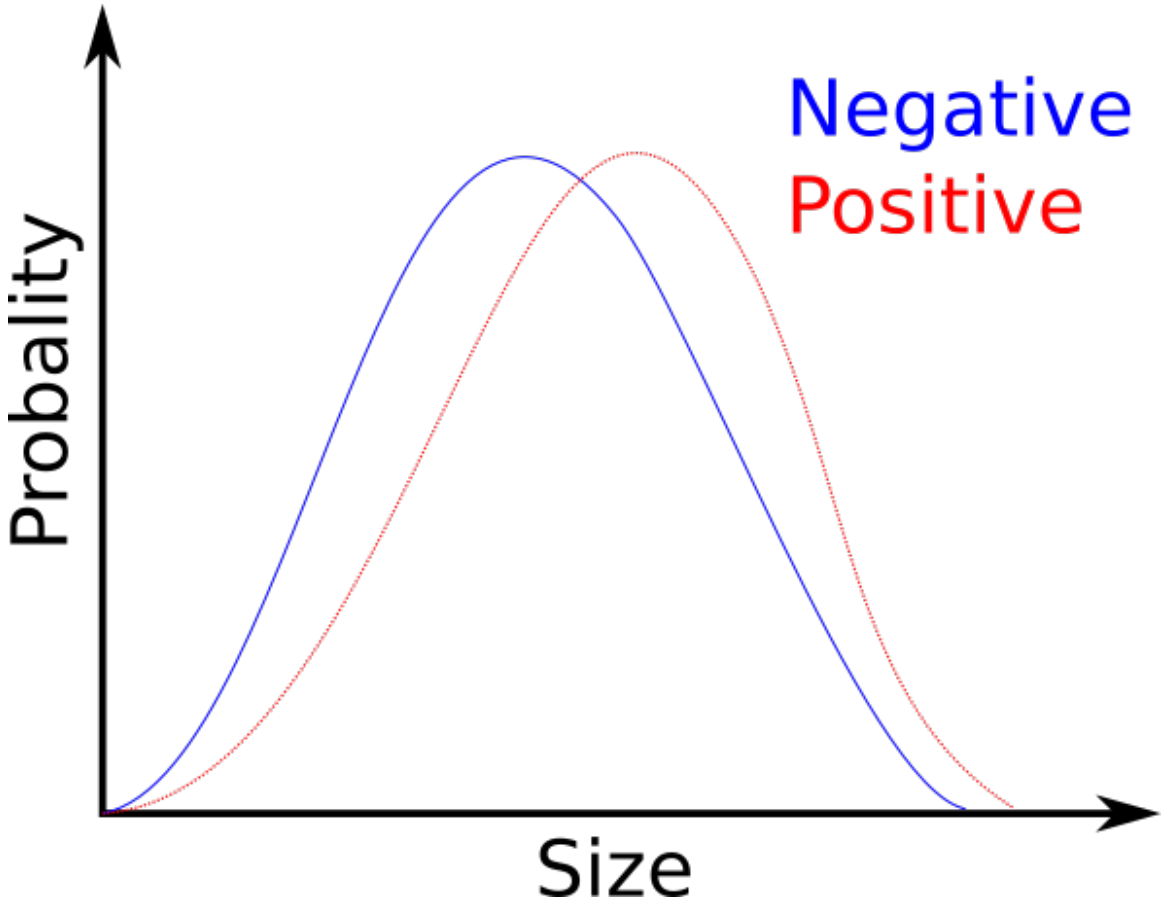

Figure 1.3: Size dependent bi-polar charging

charge density at some time t as a function of both low (n^L) and high energy state (n^H) electrons. A particle will only give up an electron during a collisions if 1) it is not depleted in high energy electrons and 2) if such exchange does not result in the particle having a charge density which exceeds the maximum charge density permitted by the atmosphere (I will return to this point later on). Likewise, I particle can only receive an electron if doing so does not result in a charge density which exceeds the maximum charge density. From Equations 1.9 and 1.9, the evolution of charge on particle i, Q_i, can be computed as:

$$Q_i = [(n_i^{H_o} - n_i^H) - n_i^L]q_e \tag{1.11}$$

where $n_i^{H_o}$ is the original number of electrons trapped in unfavorable energy states.

Ion Exchange Model: While the trapped electron model can account for charging in a wide variety of granular systems, it has important shortcomings that make it inapplicable in a general sense. Firstly, the model cannot account for the observed electrification in granular systems where particles are both chemically and mechanically (same size) homogeneous. Secondly, the model does no account for kinetic charging effects (e.g. more energetic flows becoming more electrified). Lastly, the model assumes that granular electrification arises entirely from electrons inherently trapped in materials. Such assumption appears be incomplete given the number experimental studies describing contact electrification processes mediated heavily or even driven by environmental factors (Waitukaitis, Lee, Pierson, Forman, & Jaeger, 2014) (Gu, Wei, Su, & Yu, 2013) (Xie, Bao, Jiang, & Zhou, 2016). Indeed, evidence exists that charging between colliding particles arises from a combination of spallation (small-scale material fracture) and molecular exchanges at the gas-solid interface (Lacks & Sankaran, 2011). In other words, the charge carriers transferred during contact may not be trapped electrons but ionic fragments which readily interact with adsorbed

water ions (hydroxyl and hydronium) harvested from the surrounding environment (Lacks & Sankaran, 2011) (Gu et al., 2013) (Xie et al., 2016).

A recently developed model (Gu et al., 2013) (Xie et al., 2016) suggests that the thin water films formed on micro-porous surfaces (such as sand or volcanic ash) concentrate ions, H^+ /OH^-, which are exchanged during particle-particle contacts. As a small grain and a large grain collide, some amount of their kinetic energy is converted to internal energy. The smaller particle experiences a larger temperature change than the big grain. Thus, ions flow from the high-temperature grain to the low-temperature one. However, because H^+ has greater mobility than OH^-, the hotter, small particle becomes depleted in positive charge carriers relative to the cooler, larger grain. This model has gained attention in because it not only explains the size-dependent charging observed in many granular systems, but predicts that the magnitude of charge transfer is dependent both on the kinetics of the system and on environmental conditions such as temperature and relative humidity (aspects not considered in the trapped electron model).

1.4 Fractoelectric charging

Another electrostatic process that has been recognized for some time involves charging when material is fractured. Such processes have been described extensively during the opening of cracks in materials such as rock, ice, metal, and polymers (Finkelstein, Hill, & Powell, 1973). However, a cohesive theory to explain why matter becomes electrified when fragmented has yet to be formulated. For rocks, previous work has pointed to the piezoelectric properties of some minerals (e.g. quartz) which generate potentials when strained (Takeuchi & Nagahama, 2002). Studies of precursory seismo-electromagnetic phenomena have suggested that charging of deformed rocks is produced by fluids passing (streaming potential) through newly-generated or modified pore networks (Park, 1996). Nonetheless, fracture charging has been observed in ho-

mogeneous substances containing neither piezoelectric materials nor fluids. Takeuchi, Nagahama, and Hashimoto, 2004 have shown that even materials of very high purity tend to become charged, attributing this electrification to the trapping centers inherently contained in most materials. Other, experimental efforts show that when a material is fractured, electrons, ions, and photons are emitted, leaving fragments highly charged (Dickinson, Donaldson, & Park, 1981), (Dickinson et al., 1988) (Gonzalez & Pantano, 1990) (James, Lane, & Gilbert, 2000).

1.5 Other electrification mechanisms

1.5.1 Photoelectric charging

Photoelectric charging refers to the process by which particles become electrified when exposed to radiation (Yair, 2008). Specifically, incident radiation can release electrons from the outer layers of a solid surface, leaving them positively charged. This processes is most effective under vacuum, where radiation is not attenuated by gas molecules. Photo electric charging has been invoked to explain the lofting of fine lunar sediments (Sickafoose, Colwell, Horanyi, & Robertson, 2001) (Abbas et al., 2007).

1.6 Induction charging

When particles are mobilized in an electric field, their surfaces become polarized to a degree dependent on their dielectric constant. Assuming a downward pointing electric field, the bottom halves of the particles become positive while the upper halves are positive (Note that the overall particle is still electrically neutral). During collisions, say when the bottom half of one particle comes into contact with the top half of another, these hemispheres may become neutralized. Thus, upon separation, the particles will retain a net charge. Under this mechanism, the polarity of particles

will be dependent on the electric field (Pahtz, Herrmann, & Shinbrot, 2010) (Lacks & Sankaran, 2011).

1.7 What limits charging in granular systems?

To a first degree, charging is limited by the dielectric breakdown of air(Lacks & Sankaran, 2011). Paschens law describes the gas pressure at which the insulating properties of air breakdown under the loading from an electric field.

$$V = \frac{Apd}{\ln(pd) + B} \tag{1.12}$$

Where p is the pressure, is the distance separating two charged objects (like the plates of a capacitor), and V is the breakdown voltage. A and B represent constants that depend on the composition of the medium. From this relation, it can be seen that when the product of p and d is high, higher voltages are required to produce an arc (Paschen, 1889). An electrostatic discharge occurs when charged carriers, electrons mainly, are accelerated by the electric field between two bodies held at different potentials. If this field is large enough, accelerated electrons obtain the energy required to ionize neutral gas atoms, producing more free electrons. The continuation of this ionization process results in an avalanche of electrons that flows from one potential to another (a current). However, if the pressure between the potential gap is too high, the mean free path is reduced. In this case, electron motion becomes randomized and no avalanche is produced. Similarly, when the pressure between the two bodies is low, the mean free path becomes very large (perhaps similar to the separation between the bodies). While electrons may be accelerated substantially, the chances of neutral ionization and electron cascading become small. Using the above principle, Matsuyama and Yamamoto, 1995 proposed that charge is transferred through a contact gap. Consider a particle with a small initial charge

colliding with a surface. Initially, the particles potential curve is below the Paschen curve for a given pressure condition. When in contact, charge is transferred between the surface and the particle. If the gained potential is large enough to intersect the Paschen potential, a discharge will occur as the particle moves away. This is known as *charge relaxation*. Arcing is inhibited when the particles potential drops just beneath the Paschen curve. However, in this case, the particle has acquired a net charged. Similarly, if a particle with a large potential (higher then the Paschen potential) approaches the surface arcing will precede the collision and no additional charge transfer will occur as the particle moves away.

CHAPTER 2

ELECTRIFICATION IN VOLCANIC PLUMES

Direct sampling of near-vent volcanic jets is difficult, costly, and dangerous. Thus, developing tools to probe the interior of plumes remotely is of paramount importance. One avenue that has much garnered interest in the last 20 years is the possibility of studying of volcanic clouds through electrostatic mechanisms (James, Lane, & Gilbert, 1998) (McNutt & Williams, 2010) (Van Eaton et al., 2016) (Mendez Harper & Dufek, 2016). A recent review study found that 27-35 % of eruptions were accompanied by lightning, suggesting the presence of highly-efficient charge generation and separation mechanism within plumes (McNutt & Williams, 2010). These mechanisms include triboelectrification, fragmentation charging, and charging related to the nucleation of hydrometeors. Because electromagnetic signals associated with charging can travel significant distances, changes in the ambient field as well as impulsive lightning signals can be used to monitor eruptions from afar and in poor weather conditions (James et al., 1998) (see Figure 2.2)

Volcanic eruptions have been known to produce lightning since antiquity. In Mesoamerican culture, for instance, the central deity Tezcatlipoca (Náhuatl: Smoking Mirror) was a trickster responsible for life but also destruction. Androgynous, Tezcatlipoca likely reflected physical processes surrounding the civilizations that arose in the Mexican highlands: smoking volcanoes which provided sustenance through fertile lands but also brought devastation to the landscape in the form of eruptions. To gain Tezcatlipoca's favor, the Nahuas of central Mexico would cry out "O master... May thy smoke, the cloud [of thy ire] cease; may the fire, the blaze [of thy rage] be extinguished (Baquedano, 2015)" It was through this dark cloud, his shadow, that Tezcatlipoca, also known as Tepeyollot ("Heart of Mountain"), brought illness and disease to pre-Columbian peoples. The connotation of Tezcatlipoca with the volca-

Figure 2.1: Tezcatlipoca, "Smoking Mirror", Codex Borgia

noes of the Trans-Mexican Volcanic Belt or with its products (obsidian, for example) is hard to miss. Yet, beyond being a metaphor for the ash clouds that emanated on a daily basis from Popocatépetl, that great mountain standing on the eastern side of Mexihco-Tenochtitlan, the cult around Tezcatlipoca may also have incorporated observations of the dramatic, , electrostatic processes that often accompany in large eruptions. Depicted in codices, the black figure of Tezcatlipoca, who is also Nenoc Yaotl ("The Enemy of Both Sides") and *Ipalnemoani* ("He By Whom We Live"), is missing a leg . In its place, emenates a smoking or burning serpent(Baquedano, 2015) (Olivier, 2003) a lightning bolt (Taube, 1992)–volcanic lightning or, as the Nahuas would have called it, *tlitepetlapetlani*. Yet, volcanic lightning did not remain in the realm of folklore for long. Perhaps the first recorded observation of he process was that of Pliny the Younger, who recorded a violent electrical storm during the paroxysm of Vesuvius that destroyed Pompeii in 79 AD (Pliny The Younger,

1963). Centuries later, pioneering field investigations were performed by (Symons et al., 1888), Hatakeyama, 1947, and Nagata, Sakuma, and Fukushima, 1948 who observed changes in the electric field during large eruptions and spark discharges. In the laboratory, experiments on triboelectrification were conducted by Hatakeyama and Uchikawa (Hatakeyama & Uchikawa, 1951) who described the charging of particles from the Aso and Asama volcanoes. Their experiments were the first to observe particle-size-sensitive charging phenomena in a volcanic material (as discussed in Chapter 1). More recently, similar experiments were conducted byKikuchi and Endoh, 1982 using Mt. Usu ash; these authors observed a similar size effect. The charge on particles has also been directly measured in the field by Gilbert, Lane, Sparks, and Koyaguchi, 1991 and Miura, Koyaguchi, and Tanaka, 1996 who found that grains could be electrified to potentials approaching the theoretical maximum. In the last decade, triboelectric charging of ash in a simulated conduit was explored by Cimarelli, Alatorre-Ibarguengoitia, Kueppers, Scheu, and Dingwell, 2014, who demonstrated that frictional and collisional charging alone can result in the production of discharges. Houghton, Aplin, and Nicoll, 2013 also found a correlation between the particle size distribution of an ash sample and the amount of charging. In the field, Thomas et al., 2007 has shown that volcanic lightning can be categorized in three modalities: vent lightning (comprising visibly-imperceptible discharges at the vent), near-vent lightning (discharges several 10s to 100s of meters in length occurring in the transition between the jet-thrust region and the plume), and plume lightning (large-scale lightning occurring at elevation in the plume. Behnke and Bruning, 2015 showed that these forms of lightning develop at different time within the eruption suggesting they are controlled by specific eruption parameters. Yet, despite an ever-growing corpus, many questions remain unanswered. For instance:

1. What are the principal electrification mechanisms in plumes?

2. Where and when do these processes contribute to the electrification of ash flows?

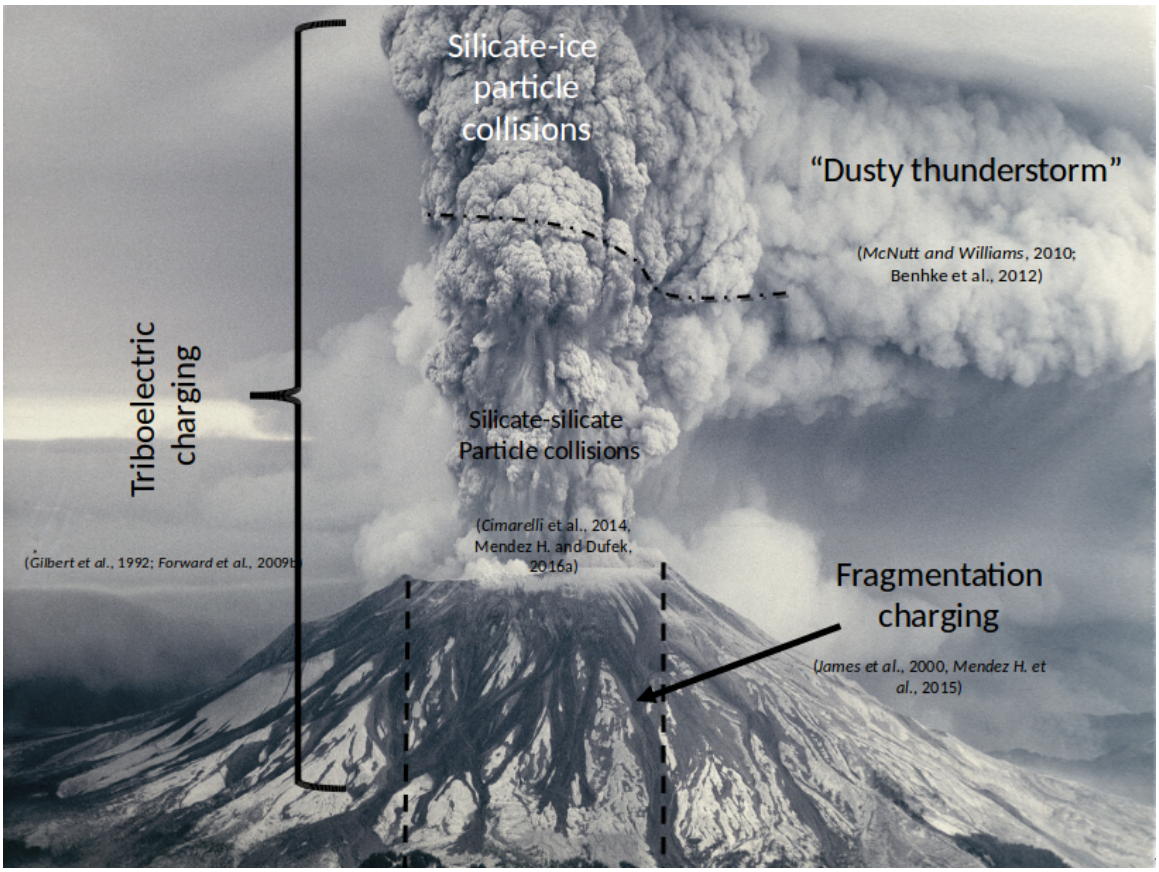

Figure 2.2: Charging mechanisms in plumes including fragmentation charging, triboelectric charging, and dusty thunderstorm charging

3. Does magma composition influence the electrostatic behavior?

4. What are the effects of environmental conditions in the plume on the generation of lightning?

5. What are the microphysical links between plume kinetics and discharge behavior?

In many ways, the first question needs to be answered before the others can be addressed. Although electrostatic processes in volcanic plumes have not been observed in-situ, a number of charging mechanisms have been proposed including triboelectrification (Kikuchi & Endoh, 1982) (Houghton et al., 2013) (Cimarelli et al., 2014) (Mendez Harper & Dufek, 2016), fragmentation charging (James et al., 2000)

(Mendez Harper & Dufek, 2015), charging similar to that found in thunderstorms (Arason, Bennett, & Burgin, 2011) Nicora, Burgesser, Rosales, Quel, and Avila, 2013, charging due to radioactivity Houghton et al., 2013, and induction charging Pahtz et al., 2010. However, even if we knew the exact electrification mechanisms operation in plumes, relating these to eruptive processes in volcanic systems is not straightforward because the physics behind many of the proposed charging mechanisms, such as triboelectrification or fragmentation charging, are themselves poorly understood. Indeed, both of these mechanisms appear to be modulated by a broad set of parameters including the physical and chemical properties of ash, the environmental conditions into which the flow penetrates, and the volatile content of the magma. Furthermore, research efforts in the industrial sector suggest that the electrification of granular materials is strongly dependent on the dynamics of the flow. Similar links between plume kinematics and electrostatics have recently been identified during eruptions of Augustine, Redoubt, and Sakurajima (Thomas et al., 2007) (Behnke et al., 2013) (Cimarelli et al., 2016). At both Augustine (2006) and Redoubt (2009), for example, a marked change in electrical activity was detected using a Lightning Mapping Array when the initial explosive phase of the eruption gave way to a buoyantly rising plume (Thomas et al., 2007) (Behnke et al., 2013) (Behnke & Bruning, 2015). Furthermore, observations at these volcanoes revealed three distinct forms of lightning, occurring at different times and within specific regions of the plumes. At Sakurajima, the frequency of discharges observed in jets was found to correlate with the overpressure magnitude at the vent (as inferred from infrasound) (Cimarelli et al., 2016) (Aizawa et al., 2016). While both volcanologists and atmospheric scientists agree that plume dynamics and electrification are related, quantitative models describing how these two processes are linked have yet to be developed.

CHAPTER 3
THE EFFECTS OF DYNAMICS ON THE TRIBOELECTRIC CHARGING OF VOLCANIC ASH

Published as: Méndez Harper, J., and J. Dufek (2016), *The effects of dynamics on the triboelectrification of volcanic ash*, J. Geophys. Res. Atmospheres, 2015JD024275, doi:10.1002/2015JD024275.

3.1 Introduction

Volcanic plumes, like many other turbulent and collisional granular systems in nature, are electrostatically charged (Hatakeyama, 1947) (Hatakeyama & Uchikawa, 1951) (Lane & Gilbert, 1992) (Miura et al., 1996) (Nicora et al., 2013) (Aizawa et al., 2016) (Cimarelli et al., 2016). Perhaps the most dramatic consequence of this electrification are the impressive lightning displays observed during some vigorous eruptions. While volcanic lightning and, by extension, charging has been reported for millennia (Pliny The Younger, 1963), the physics that generate and separate charge in plumes still require clarification. Studies of the distribution of volcanic lightning worldwide demonstrate that some volcanoes produce charged plumes more efficiently than others (McNutt & Williams, 2010). The observed variability in electrical behavior across eruptions and across volcanoes suggests that the generation and separation of charge is modulated by specific eruption parameters such as fragmentation behavior, the properties of the ejected materials (both ash and volatiles), environmental conditions, as well as the dynamics of the plume itself. Therefore, understanding the coupling between the key properties of an eruption and electrical activity, much of which can be studied remotely, may yield information about the internal dynamics of an eruption which would otherwise be opaque to observation (James et al., 1998). Indeed, Behnke and Bruning (Behnke & Bruning, 2015) have recently shown that lightning (and, by

association, electrification) could be used to infer changes in eruption kinematics. Additionally, understanding charging processes is important because electrostatics can profoundly influence the transport of ash in the atmosphere. For example, charges on small grains drives dry aggregation (James, Lane, & Gilbert, 2003) (Telling, Dufek, & Shaikh, 2013), causing grains to form aerodynamically larger particles which have shorter residence times in the atmosphere than single grains. Lightning can also fuse ash particles together, creating spherules (Genareau, Wardman, Wilson, McNutt, & Izbekov, 2015) which have drag coefficients different that those of angular grains.

Determining the principal electrification processes in plumes remains an active area of research. In reality, the production of lightning likely stems from a synergistic interplay between multiple charging mechanisms, some of which operate in specific regions of the eruptive system, during certain times (Thomas et al., 2007). Fractocharging is thought to be a principal charging process associated with fragmentation in the conduit and during disruptive particle collisions in the plume (James et al., 2000) (Mendez Harper & Dufek, 2015). Charging involving the interaction of ash and hydrometeors operates in the regions of plumes that reach sufficient altitude to condense and freeze magmatic and/or environmental water (Herzog, Graf, Textor, & Oberhuber, 1998) (McNutt & Williams, 2010) (Arason et al., 2011). Tribochargingfrictional charging between ash grainshas been described as an important electrification process in volcanic plumes (Harrison, Nicoll, Ulanowski, & Mather, 2010) (McNutt & Williams, 2010) (Cimarelli et al., 2014) (Houghton et al., 2013) because this kind of charging is unquestionably active throughout the entire eruptive system as long as there are particle-particle collisions. Beyond the large-scale temporal and spatial differences between these mechanisms, important dissimilarities exist at the grain scale. For example, size-dependent bi-polar charging (i.e. where large particles charge positively and small grains charge negatively, on average) appears to be a rather universal characteristic of triboelectric charging (Lacks & Levandovsky, 2007) (Forward et al.,

2009b) (Lee, Waitukaitis, Miskin, & Jaeger, 2015). Such size dependence, however, is not present in the fracture mechanism (i.e. a small particle is just as likely to charge positively or negatively, and vice versa (Dickinson, Jensen, & Jahan-Latibari, 1984) (James et al., 2000). Furthermore, there is evidence that small-scale processes can importantly tune large-scale electrostatic phenomena. The presence of fine ash in a hydrometeor-dominated system, for instance, has been observed to produce lightning that differs considerably from conventional thunderstorm lightning (Lang et al., 2013). In a similar manner, the three different lightning modalities that have been recognized during eruptions (vent, near-vent, and plume lightning (Thomas et al., 2007)) may be associated with particular small-scale processes, but concrete links between these have yet to be established. While tribocharging has been inferred to be one of the major electrification processes in plumes for decades (along with fragmentation and ice-based charging), little experimental work has been carried out to determine what parameters (chemical, physical, and hydrodynamic) modulate the charging of ash via this mechanism. We note that triboelectric processes in general, which encompass frictional and contact charging, are poorly understood phenomena. Tribocharging in granular systems composed of chemically distinct grains has been attributed to differences in the surface work function, the minimum energy required to remove an electron from a solid surface (Lowell & Rose-Innes, 1980) (Matsusyama & Yamamoto, 2006). Surprisingly, however, even systems composed of chemically identical particles (materials with the same work function) have been shown to charge (Lowell & Truscott, 1986a) (Lowell & Truscott, 1986b) (Kok & Lacks, 2009) (Lacks & Sankaran, 2011), although the degree of charging is often less than that observed in heterogeneous substances. In chemically homogeneous materials, charging might arise from the transfer of electrons bound in high-energy states on one surface to empty low-energy states on another (Lowell & Truscott, 1986b), from small-scale chemical variations on grain surfaces (Apodaca, Wesson, Bishop, Ratner, & Grzybowski,

2010), or perhaps from molecular-scale material transfer. Furthermore, charging in these systems appears to be controlled by the particle size distribution of the material, suggesting that asymmetric contact is necessary to produce electrification (Lacks & Sankaran, 2011) (Bilici, Toth, Sankaran, & Lacks, 2014). Indeed, experiments consistently show that in mixtures of different grain sizes the relative size of a grain determines its polarity, with small grains usually charging negatively and larger ones charging positively (Hasegawa & Takeuchi, 2000) (Lacks & Levandovsky, 2007) (Duff & Lacks, 2008) (Forward, Lacks, & Sankaran, 2009a) (Waitukaitis et al., 2014). In the volcanic context, pioneering experiments on triboelectrification were conducted by Hatakeyama and Uchikawa (Hatakeyama & Uchikawa, 1951) who described the charging of particles from the Aso and Asama volcanoes. Their experiments were the first to observe particle-size-sensitive charging phenomena in a volcanic material. Similar experiments were conducted by Kikuchi and Endoh (Kikuchi & Endoh, 1982) using Mt. Usu ash; these authors observed a similar size effect. More recently, triboelectric charging of ash in a simulated conduit was explored by Cimarelli et al., 2014, who demonstrated that frictional and collisional charging alone can result in the production of discharges. Houghton et al., 2013 also found a correlation between the particle size distribution of an ash sample and the amount of charging. While these recent studies have made extensive progress towards understanding frictional electrification in plumes, they are not without some limitations. In Cimarelli et al., 2014 charging was achieved by driving an ash sample through a metal pipe at high pressure. Given the relatively wide difference in metal and silicate surface work functions (which controls how much charge is transferred when two chemically distinct materials are brought into contact) (Shaw, 1917) (Cross, 1987), some of the observed discharges may have been a result of friction between the pipe walls and the sample as the latter was ejected rather than silicate particle-particle charging sensu stricto. Indeed, other experimental studies found that tribocharging between distinct ma-

terials produces enhanced electrification as compared to charging arising from the interaction of chemically identical substances (Forward, Lacks, & Sankaran, 2009d) (Liao, Hsiau, & Huang, 2011). Similar conditions are present in some of the early experiments of Kikuchi and Endoh (Kikuchi & Endoh, 1982) who used a metal ramp to electrify grains (although, we acknowledge that other experiments by these authors used ash-coated ramps to mitigate this problem). In Houghton et al., 2013, the investigators only considered the bulk charge of the granular material, measured by placing the entire fluidized sample into a Faraday cup. Because the bulk charge is the net sum of all the negatively and positively charges in a sample, the bulk charge only reveals whether a net transfer of charge to or from the material has occurred (perhaps from contact between the granular substance and a surface such as a pipe wall), not how much charging has occurred in the material itself. To illustrate this point, consider an ideal system in which interactions are strictly between constituent particles. The charges on single grains may become quite high after many collisions or may be rapidly redistributed, but, in order to satisfy conservation of charge, the bulk charge will always remain zero! As such, to characterize frictional electrification processes in volcanic eruptions, experiments must be conducted so that ash grains have minimal contact with foreign surfaces and the charge on individual grains, not the bulk material, must be characterized. In this work, we present a set of experiments designed to investigate the temporal aspects of volcanic ash charging due to silicate particle-particle collisions only. In a controlled environment, we assess how the dynamics of the granular interaction influence the electrostatic behavior of ash. Additionally, we measure the distribution of absolute charge in samples from three different volcanoes, allowing us to explore the sensitivity of charging to silicate composition. Our work is the first work to experimentally relate the dynamics of a fluidized sample of volcanic ash to remotely-captured electrostatic signals in a quantitative manner.

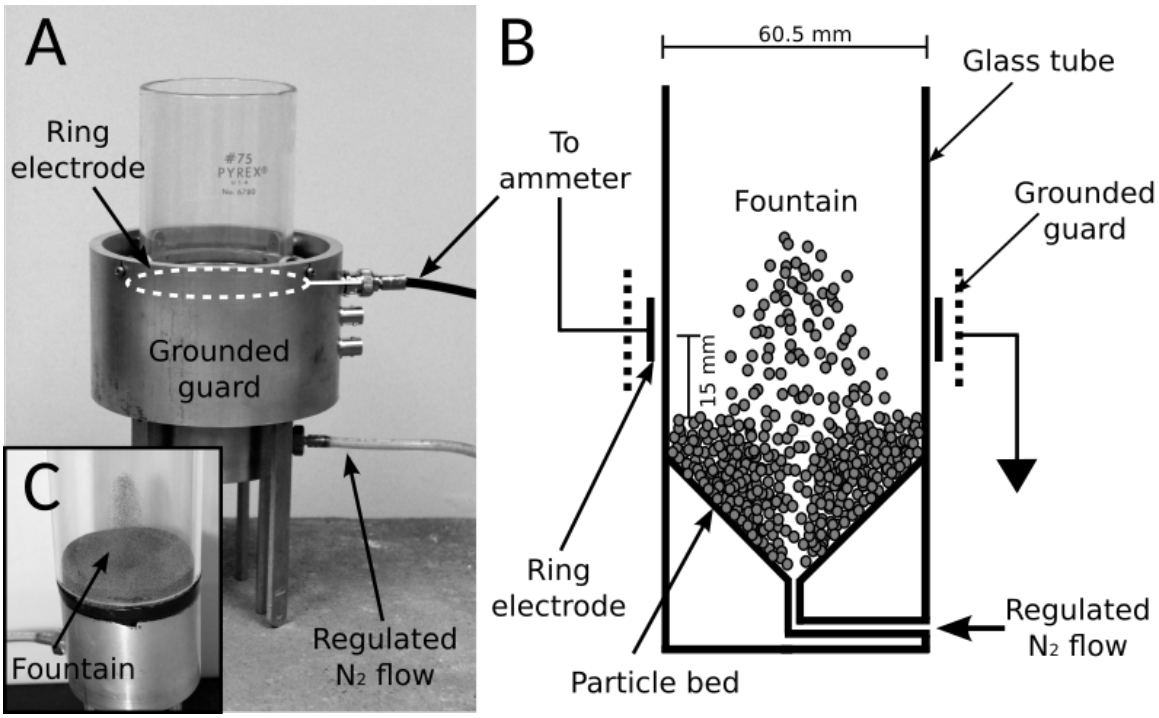

Figure 3.1: A) Photograph of the experimental setup. The upper section consists of a spouted bed designed to produce numerous particle-particle collisions while minimizing collisions with the walls. The time dependent charging is measured by a guarded aluminum ring electrode connected to a pico-ammeter. The interior workings of the fluidized bed are rendered schematically in B). Inset C) is a photograph of the apparatus with the ring guard removed revealing the particle fountain. Notice it does not contact the walls of the reactor

3.2 Methodology

Based on the work of Forward et al., 2009a, we constructed an instrument capable of characterizing the triboelectric charging of ash arising from particle-particle collisions. The instrument or reactor, rendered photographically in Figure 3.1a and shown in schematic form in Figure 3.1b, consists of a glass tube fitted onto a machined aluminum distribution cup with a 200 micron hole milled into its bottom. A shielded aluminum ring electrode is positioned around the glass tube, 1.5 cm above the lip of the distribution cup. The electrode is directly connected to the input of a 6485 Keithley picoammeter via a low-loss BNC cable.

The reactor can hold up 60 ml of ash. Before each experiment, the sample is

sprayed with an ionizing gun for 1 minute and then allowed to sit for an hour to minimize any initial charge imparted during handling. Once this period has elapsed, the apparatus is placed in a vacuum chamber. The effects of atmospheric water vapor are minimized by conducting the experiments in a highly dry (¡ 1 humidity), low pressure, nitrogen environment (20 kPa). To fluidize the bed and produce charging, a steady stream of nitrogen is forced through the 200-micron hole in the distribution cup for 60 minutes. In the resulting fountain, particles undergo collisions with each other and exchange charge triboelectrically. The diameter of the reactor is large enough to preclude particle-wall collisions, ensuring that the triboelectrification of the ash parcel results primarily from particle-particle interactions. The fountain passes through the center of the electrode (Fig 1a and 1b) but does not come into contact with it. When a charged particle enters the volume enclosed by the ring electrode, a current flows through the picoammeter to ground. As that same particle exits the sensing volume, a current of equal magnitude but opposite polarity is produced. The overall current measured by the picoammeter reflects the sum of all the currents associated with charged particles entering and exiting the electrode sensing volume at a given time. The picoammeter measures and time-stamps the current every 60-80 ms. While the time-averaged current in the electrode is zero amperes (consistent with the closed system of the apparatus), the instantaneous current can attain magnitudes of several 10s to 100s of pA (superimposed on a noise floor ranging between 0.1 and 1 pA). The temporal behavior of particle charging is assessed by analyzing the change in the standard deviation of this instantaneous current across small timescales (every 5 sec).

We performed experiments using ash from three volcanoes: Lawetlatla (Mt. Saint Helens - State of Washington, USA), Tonaltepetl (Fuego de Colima - States of Xalixco and Coliman, Mexico), and Tungurahua (Tungurahua Province, Ecuador) to examine the effect of ash compositions on charging (Note: In an attempt to preserve vanishing Native American heritage, the present work employs pre-Columbian names for the

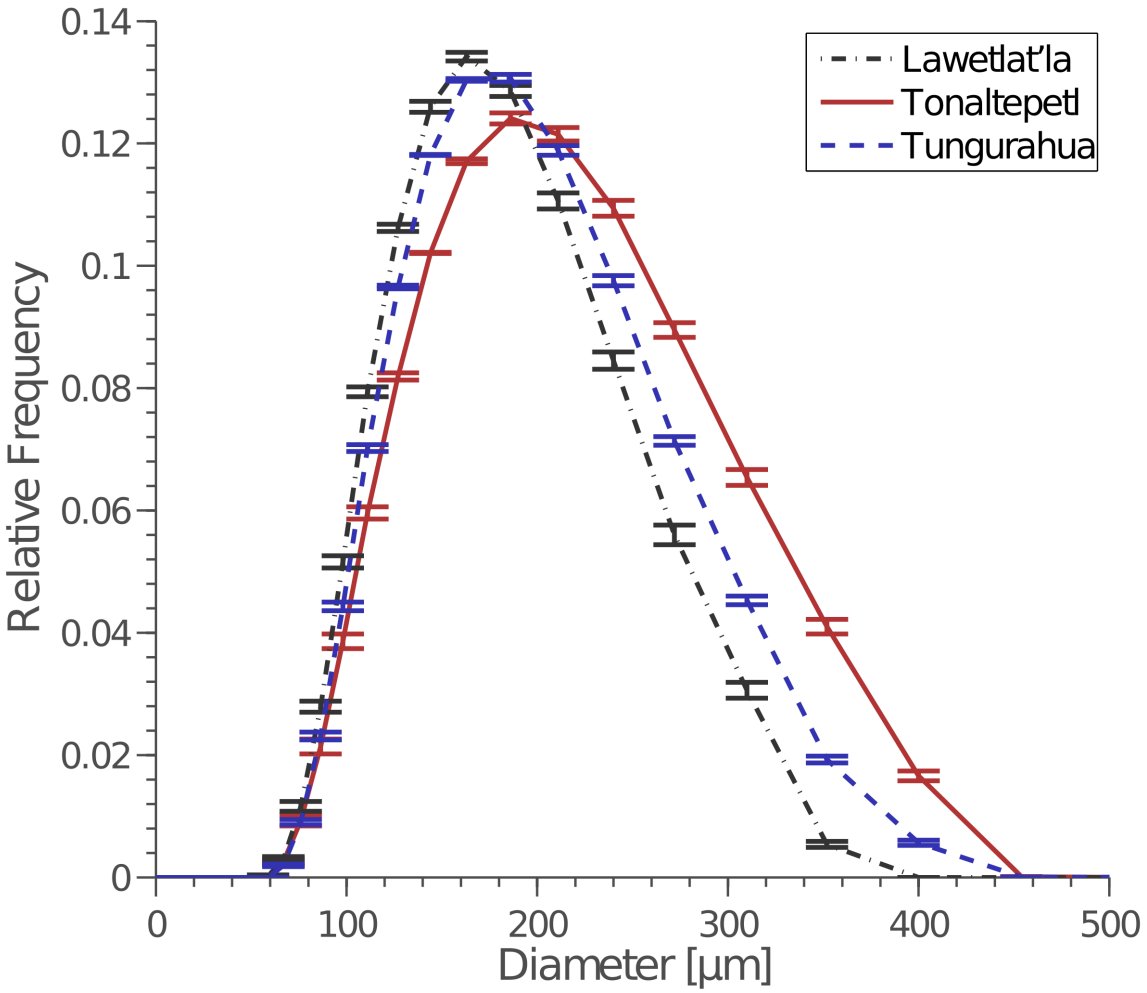

Figure 3.2: Size distribution of the three sieved samples. Material was sized using a Malvern MasterSizer 3000.

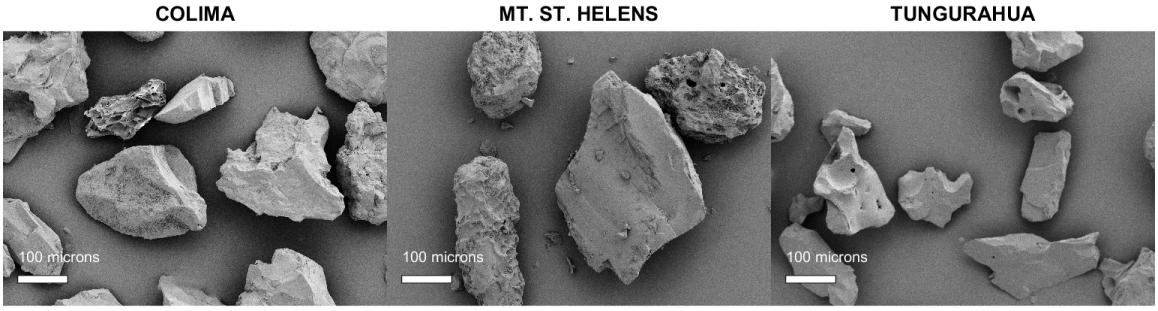

Figure 3.3: SEM images of the three ash samples. In general, particles have similar morphologies with varying degrees of porosity. Tonaltepetl (Colima) ash is from a 2014 eruption. The Lawetlatla (Mt. Saint Helens) ash sample comes from the 1980 eruption. Tungurahuas ash was collected in 2010.

volcanoes). The ash samples were sieved, achieving the particle size distributions shown in Figure 3.2 (measured with a Malvern Mastersizer 3000E). Tonaltepetl and Tungurahua particles are andesitic in composition, while the ash from Lawetlat'la is dacitic. The three ash samples have comparable densities (Tonaltepetl: 2.44 gm^{-3}, Lawetlatla: 2.57 gm^{-3}, Tungurahua: 2.45 gm^{-3}) and particle morphologies with varying degrees of vesicularity (See Figure 3.3), producing similar fluidization behaviors. The particle bed was excited under 4 different bed pressures (1.14, 1.40, 1.72, and 2.02 kPa). These driving pressures are in excess of the background 20 kPa in the vacuum chamber and were measured at the hole in distribution plate. Each sample was run under the same driving pressure 4 times. During an experiment, vessel pressure, the bed pressure, temperature, and humidity were maintained constant using PID controllers implemented in LabVIEW. As an example, 100 seconds of raw current data from an experiment using Tonaltepetl ash fluidized by a bed pressure of 2.02 kPa are shown in Figure 3.4. We note that the atmospheric parameters (including the low pressure, low humidity nitrogen environment), the particle size distributions, and the

gas flow rates were selected primarily to emphasize and isolate the charging effects arising from changing dynamics in the fountain comprising natural volcanic material. Thus, the fountaining geometry was not designed to represent any particular macroscopic region of a volcanic plume.

While the measurement system described above is an effective way to monitor the temporal aspects of charging and similar techniques are used extensively in industrial applications (Forward et al., 2009c) (Murtomaa et al., 2003), it is difficult to estimate the charge distribution on grains in the sample (it can only be used to make an estimate of the bulk charge). As mentioned previously, a charged granular material may be composed of particles with both negatively and positively charged particles and the current signal recorded by the picoammeter is the superposition of many currents induced by particles of both polarities. To measure the final charge distribution on individual ash grains, a second set of runs were conducted using the same fluidization and environmental parameters, but with the ring electrode replaced by a horizontal, copper airline. The airline has an inner diameter of 5 mm and is placed 7 cm away from the axis of the fountain, at a height of 3 cm above the bed (see Figure 3.5). After 60 minutes of fountaining (i.e. once the samples reached electrostatic steady-state), a solenoid was activated, allowing a small volume of nitrogen to pass through the airline. The burst of gas served to blow particles out of the fountain, while minimizing their contact with other surfaces. A similar measurement technique has been outlined previously by Bilici et al., 2014. The falling particles were then sampled by an array of 8 through-type Faraday cages or Faraday tubes connected to 8 charge amplifiers (Figure 3.5c). Grains traversing the Faraday tubes were collected in a small reservoir beneath the sensors and then sized using an optical microscope to extract circular-equivalent diameters. Each Faraday tube has a length of 10 mm and an aperture diameter of 5 mm. The operation of the charge amplifiers is described

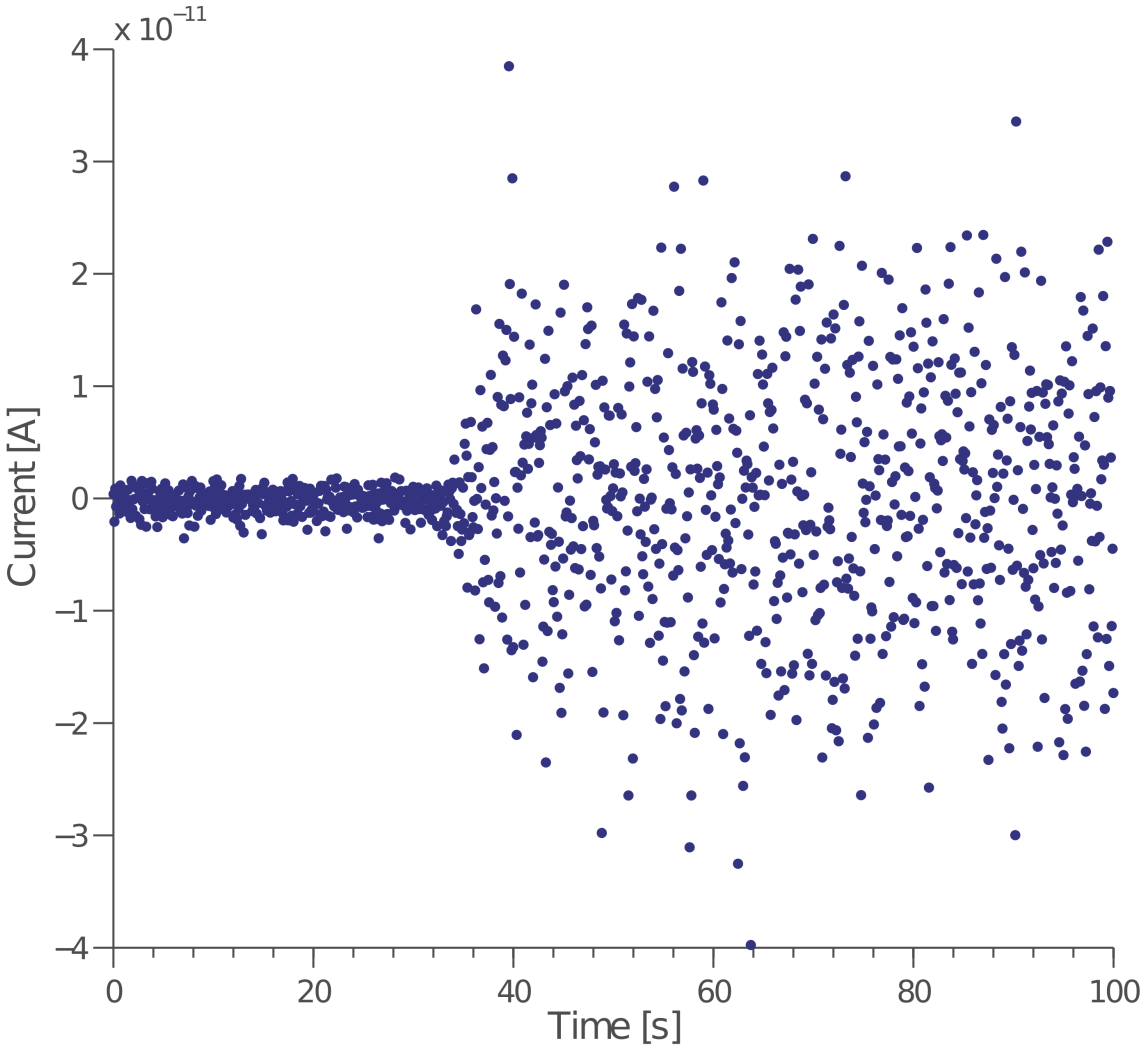

Figure 3.4: One hundred seconds of raw current data from the ammeter collected at the start of an experiment fluidized at a pressure of 2.02 kPa. Current values are sampled approximately every 60-80 ms. While the average current is zero, the magnitude of the excursions away from the mean grow with time. The uncertainty in the measurement is on the order of $10^{-13} - 10^{-12} A$.

by the following transfer function:

$$V_o = \frac{-Q}{C_f} e^{t/\tau_{RC}} \tag{3.1}$$

In Equation 3.1, Q is the charge of the particle enclosed by the Faraday tube, C_f is the input capacitance, t is time, and τ_{RC} is the time constant of the charge amplifier set by a capacitive/resistive feedback network. When a particle traverses the Faraday tube, the charge amplifier produces voltage pulses with magnitudes proportional to the charge on the grains (Chang, Kelly, & Crowley, 1995). Each channel can be sampled at 6 kHz and can resolve charges smaller than 10 fC. The small dimensions of the Faraday cup and high sampling rate mean that single grains can be detected.

Using this methodology, we directly sampled the distribution of charges in the fountain. An example of raw charge data from a run of Tonaltepetl ash fluidized at 2.02 kPa is shown in Figure 3.6. As seen, particles charged both positively and negatively. Sharp peaks are representative of single particle traversing the sensing volume. At times, two or more grains entered the sensing volume in rapid succession, producing overlapping voltage pulses (See annotation in Figure 3.6). Visual inspection of the raw data was performed to exclude all but the single, sharp pulses characteristic of the passage of individual grains.

3.3 Results and Discussion

3.3.1 Charging Rates

As previously described, the temporal charging behavior of a sample can be investigated by computing the change in standard deviation of the recorded current with time (the mean current remains zero throughout the experiment). Graphically, this procedure is depicted in Figure 3.7, yielding what we call a charging curve (computed for a sample fluidized at 2.02 kPa). At the onset of an experiment, the current's

Figure 3.5: A) Schematic depicting the methodology employed to characterize the charge on particles in the fountain in a non-contact manner. Grains are blown out of the spouted bed by a burst of air causing them to fall into an array of eight through-type Faraday cups. A charge amplifier connected to each of the Faraday tubes outputs voltage pulses with heights proportional to the charge on individual grains. B) Close-up photograph of particles being ejected from the fountain. C) Photograph of one through-type Faraday cup channel.

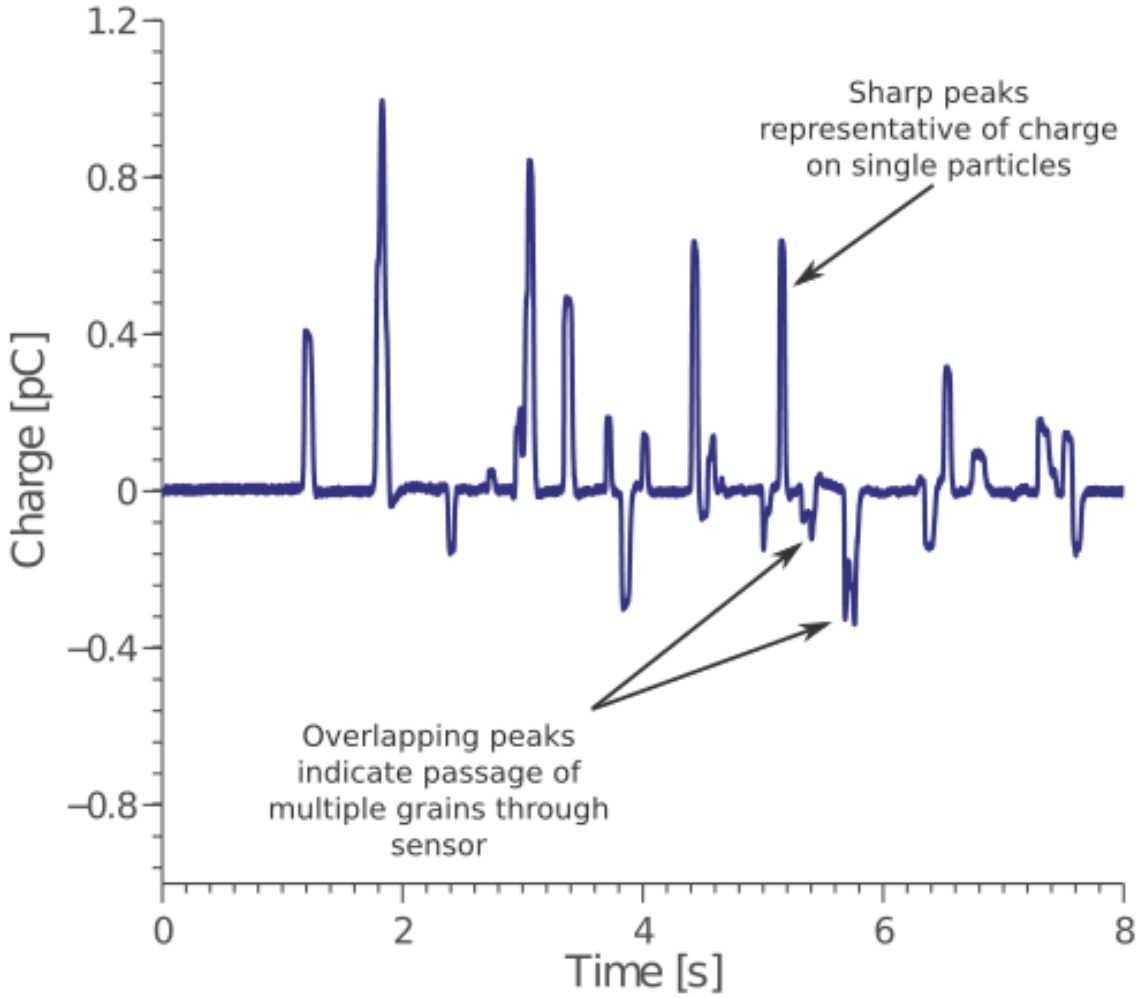

Figure 3.6: Particles blown out of the fountain fall into a set of 8 Faraday tubes, producing voltage pulses with heights proportional to the charge on their surfaces. The above figure shows data from one of the eight channels captured during a run using a Tonaltepetl (Colima) ash fluidized at 2.02 kPa. Notice that particles charge both positively and negatively. Pulses with multiple peaks or broad widths represent multiple particles passing through the sensing volume. This data is discarded.

standard deviation rapidly increases. After a few minutes, the standard deviation reaches a steady-state value and levels-off. The charging curves obey the following exponential relationship:

$$I(t) = I_s[1 - e^{-t/\tau}] \tag{3.2}$$

where $I(t)$ is the induced current's standard deviation, I_s represents the standard deviation of the steady-state current for a given driving pressure, and t is time. The time constant, τ, is defined as the time required for the signal to reach 63.2 of its steady-state value. For a given run, τ can found by fitting Equation 3.2 to the experimental data. Following convention, the particles in the spouted bed are said to have reached electrostatic steady-state after approximately 5 time constants. The time constants as functions of bed pressure for the three ash samples are shown in Figure 3.8a. High-speed videography of the initial minute of the experiments show that after initial overturn events and a brief period of pulsing (10 s after the start of an experiment), the fountaining becomes stable. The fact that fountaining transients are much shorter than the time it takes for the standard deviation of the current to reach steady-state indicates that the signals recorded by the picoammeter capture the triboelectric charging behavior of the fountaining granular sample and not unsteady flow conditions. Figure 3.8b plots the steady-state currents for the three ash samples versus driving pressure. The increase in steady-state current standard deviation with higher bed pressure results from the ash fountain becoming taller and wider, with more particles passing through the volume of the sensing electrode (i.e. it does not necessarily mean the particle fountain is more charged). Similar to results discussed elsewhere (Liao et al., 2011), we find that the charging time constant decreases with increasing energy input to the system (see Figure 3.8a), i.e. more energetic flows become charged with enhanced efficiency. In the present work, takes values between 2 and 3 minutes, with samples reaching electrostatic steady-state

in periods ranging from 10 to 15 minutes. Because charging is isolated to particle-particle interactions, decreasing time constants indicate that the contact frequency increases as the bed is fluidized at higher pressures. We note that previous work has shown that triboelectrification may arise from both direct particle-particle impact contacts as well as sliding particle contacts and that the electrification behavior may be different for each case. Given that it is impossible to characterize these contacts independently in the experimental setup, we employ the words contacts and collisions in the present work interchangeably to encompass both modalities.

As was the case with the current curves discussed above, the rate of charging can be described (after Hogue, Calle, Weitzman, and Curry, 2008) by an exponential:

$$q(t) = q_s[1 - e^{-t/\tau}] \tag{3.3}$$

where q_s is the steady-state charge and τ is the time constant. Alternatively, Equation 3.3 can be cast in terms of a discrete number of particle collisions (Pei et al., 2013)

$$q(n) = q_s[1 - e^{-kSn}] \tag{3.4}$$

In Equation 3.4, n is the number of collisions, S is the contact area, and k is a constant related to the particle size and contact potential that drives charge from one surface to another. In chemically heterogeneous systems, this potential stems from the differences in work functions. In granular media composed of identical insulators (where the effective work function is the same for all particles) the factors that give rise to this contact potential are less well defined. Experiments performed byMatsusaka et al., 2000, as well as the numerical work of Pei et al., 2013, have shown that rubber particles impacting a metal plane reach electrostatic equilibrium after several dozen collisions. Assuming a system of chemically identical insulating

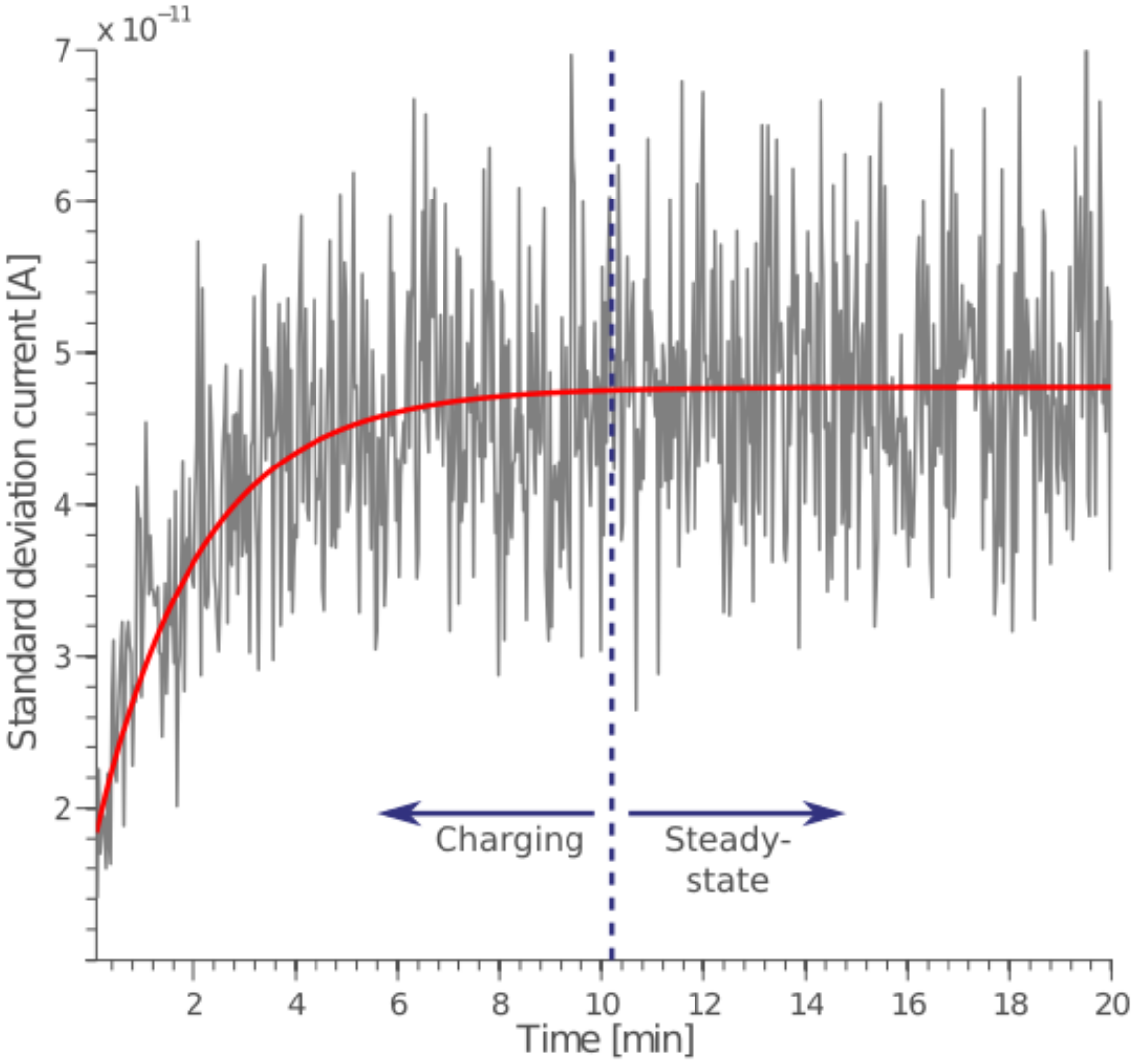

Figure 3.7: Example charging curve. The temporal aspect of charging can be quantified by potting the standard deviation of the current with time. As show above, at the onset of the experiment, the standard deviation climbs rapidly then levels-off after a several minutes. Charging curves can be described by the exponential function in Equation 3.2

particles reaches steady-state after a comparable number of impacts, the collision rates in our experiments would range from 0.04-0.06 collisions per particle per second in the lowest energy case to 0.07-0.1 collisions per particle per second for the greatest fluidization energy. Because of the similar effective work functions between silicate materials, triboelectric charge transfer amongst ash grains of the same composition is probably less efficient than that between dissimilar substances. In other words, a smaller amount of charge is transferred from one surface to another during impact and the number of collisions needed to saturate grains may be greater than those quoted here (perhaps by more than an order of magnitude). Thus, the crude calculation we present above represents the most efficient charge transfer scenario and serves only to set a lower limit for the collision rates expected in the experimental setup.

3.3.2 Absolute Charge Measurements

A second set of experiments was conducted to measure the distribution of charges in the fountain at steady-state conditions. For these runs, the glass tube and electrode arrangement were removed, exposing the fountain of particles. Using a small burst of air, particles were knocked out of the fountain, a process depicted in Figure 3.5a and b. The ejected particles then fell into an array of eight, millimeter-sized Faraday tubes, allowing us to directly measure the charges on individual grains (Figure 3.5c). Having passed through Faraday tubes, sampled grains were collected and sized using an optical microscope. The size distributions of the sampled particles for the three ash types are shown in Figure 3.9a. Comparison between these distributions and the original size distributions rendered in Figure 3.2 (represented by grey curves in Figure 3.9a) indicates that the sampled grain size distributions have an overall bias toward large sizes. We believe the bias has to do with the fact that larger particles, which are less well coupled to the burst (they have larger Stoke's numbers) fall out of the airstream faster than the small ones. Specifically, the smallest grains (less than 130

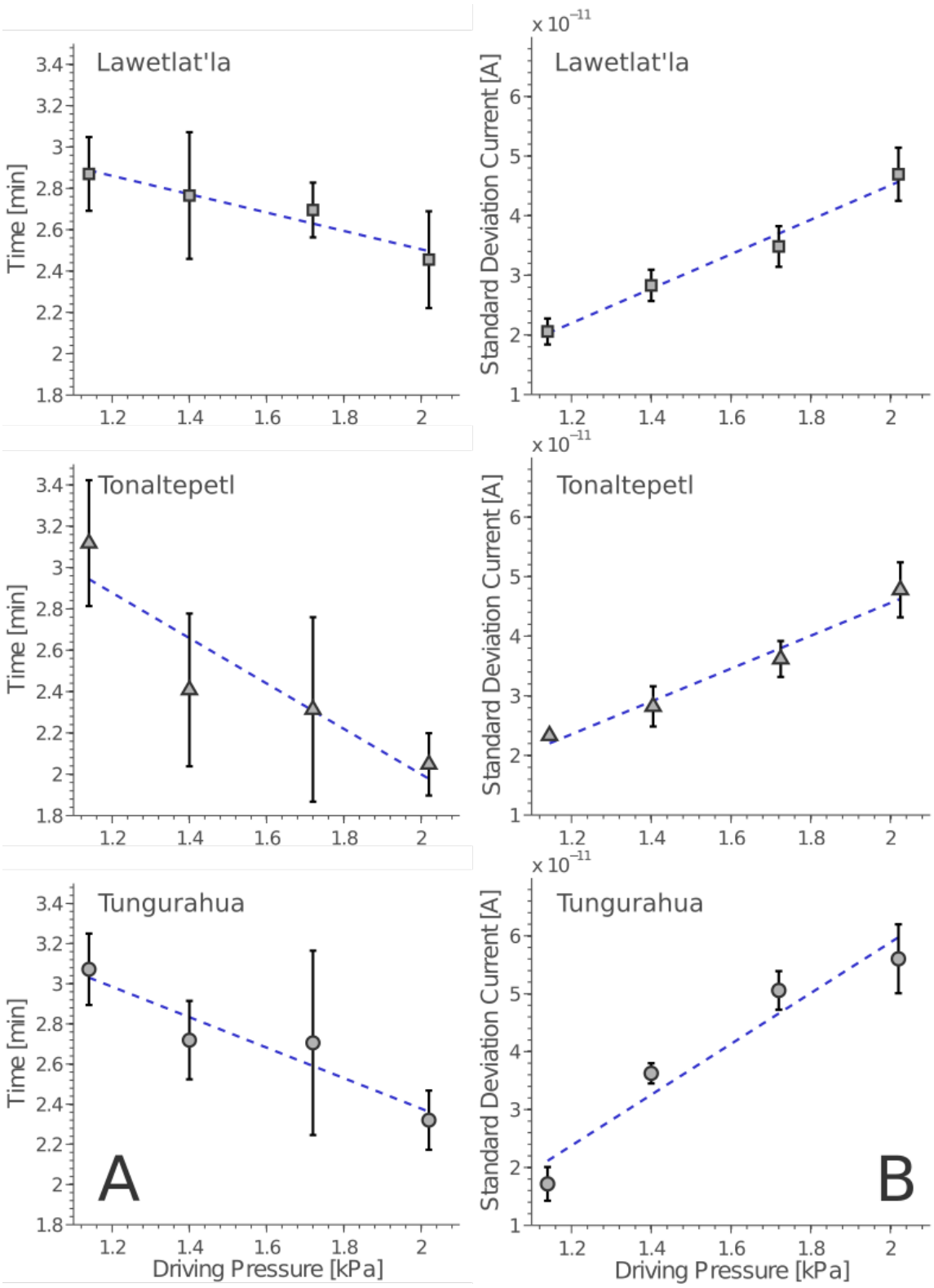

Figure 3.8: A) The time constant decreases with increasing bed pressure, demonstrating that more energetic flows become electrified in shorter periods. B) The measured current increases with bed pressure because more particles pass through the ring electrode in a given time. Note that there isn't a significant difference in behavior between samples.

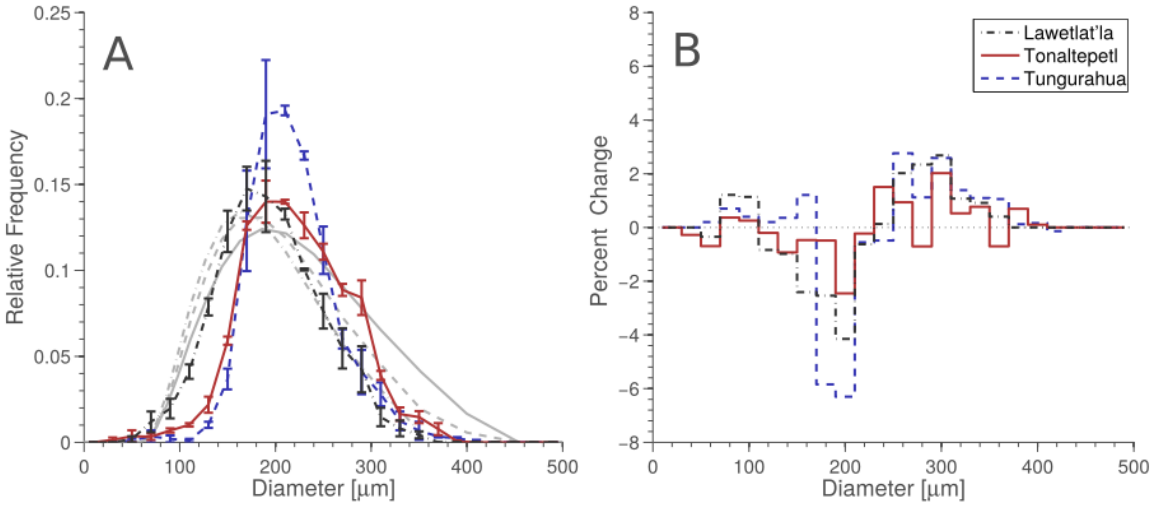

Figure 3.9: A) Size distribution of particles sampled from the fountain (color curves) superimposed on original size distributions (grey curves). The sampling method preferentially samples larger particles from the flow. The error bars in Figure 3.9a represent the variation in grain size between particles sampled from the highest (2.02 kPa driving pressure) and lowest energy fountains (1.14 kPa driving pressure). B) Relative percentage change in particle size between sampling during fountaining at 1.18 kPa and 2.02 kPa. Approximately 1000 particles were characterized per volcanic sample.

microns) may preferentially overshoot the Faraday cup array. Unfortunately, with the present arrangement, we have very little flexibility in capturing the full suite of small particles ejected from the plume. The error bars in Figure 3.9a represent the variation in grain size between particles sampled from the highest (2.02 kPa driving pressure) and lowest energy fountains (1.14 kPa driving pressure). The difference in grain size in the highest energy fountain relative to that of the lowest energy fountain is plotted in Figure 3.9b. As observed, blowing grains out of the highest energy fountain results in samples slightly enriched in larger particles while samples from the lowest energy flow are slightly enriched in smaller grains. This slight asymmetry likely has to do with the fact that the height of the fountain increases with increasing energy and the air burst, which remains at a constant height, samples grains from different segments of the fountain. For each sample, the charges on approximately 500-700 particles was characterized. Particles acquired both negative and positive charges.

The overwhelming majority of grains (¿90) carried charges on the order of or smaller. The most electrified grains obtained charges on the order of pico-Coulombs (). The charge distributions obtained for the three samples fluidized at the highest pressure are rendered in Figure 3.10. Charge distributions are essentially Gaussian with zero means. Although this cannot be discerned visually in Figure 3.10, we consistently detected slightly more (1 4) grains with negative charge than particles with positive charge. While we designed the experimental setup to specifically minimize grain interactions with foreign surfaces, it was inevitable that a small fraction of grains impacts the edge of the distribution cup as they were blown out. Thus, the slight skew toward negative charging may be a consequence of dissimilar-material tribocharging. However, this scenario is unlikely given that silicates tend to charge positively when brought into contact with either to metals or plastics. Another possibility is that particle-particle contacts in the fountain result in spallation at very small scalesi.e. our experiments may also incorporate fragmentation processes. While many studies suggest that both positive and negative ions and electrons are emitted during fracture (implying that such process does not bias the polarity of the parent material) (Dickinson et al., 1981) (Dickinson et al., 1984) (Enomoto & Chaudhri, 1993), James et al., 2000 inferred that positive ions were emitted in higher numbers during the fracture of pumice samples, leaving fragments with overall negative charge. A similar loss of positive ions in our work could account for the observed negative bias. A useful metric to compare the chargeability of materials is the surface charge density or the charge normalized to the surface area of the particle. Net particle charge density distributions were obtained by computing the joint probability of the sampled grain size (accounting for the variations in grain size due to sampling location in the fountain discussed in the previous paragraph) and charge probability distributions. For simplicity, the particles' surface areas needed for this calculation were computed from the circular equivalent diameters obtained from the microscopy analysis. The

charge densities for both the highest (dashed red) and lowest (solid blue) fluidization energies for the three volcanic samples are depicted in Figure 3.11 on a logarithmic scale. Although the charges on fractions of the smallest grains were not sampled (for the reasons described above), their absence may not affect the overall distributions in Figure 3.11 because the magnitude of the steady-state charge density is generally unaffected by grain size for particles larger than 10 microns (Hamamoto, Nakajima, & Sato, 1992). While small-scale variations exist between the low and high collision rate distributions, the range of steady-state charge densities seem to be unaffected by the energy input to the system. As reported in other fluidization experiments (e.g. Revel, Gatumel, Dodds, and Taillet, 2003), we find that varying the energy input system influences how long it takes for the granular material to reach steady-state, but does not influence the magnitude of the steady-state charge.

3.3.3 Steady-state charge densities on grains and the charge relaxation model

The result that the steady-state charge density is independent of energy input may seem surprising or even counterintuitive. After all, previous charging experiments involving single particle-particle collisions have demonstrated that the magnitude of the charge transfer correlates with the particle's kinetic energy at impact] (Matsusaka et al., 2000) (Matsusyama & Yamamoto, 2006) (Watanabe et al., 2006) (Liao et al., 2011). Yet, this positive relation between energy and charging has also been shown to exist only across a specific range of surface charge densities; once a particle has acquired a certain amount of chargesometimes termed the equilibrium or saturation chargeno further charge transfer occurs regardless of kinetic energy or the number of subsequent impacts (Matsuyama & Yamamoto, 1995) (Watanabe et al., 2006). In other words, the steady-state charge in a granular flow appears to be capped by parameters which are independent of collisional granular dynamics such as particle size and composition (Hamamoto et al., 1992), pipe diameter (in the case of pipe

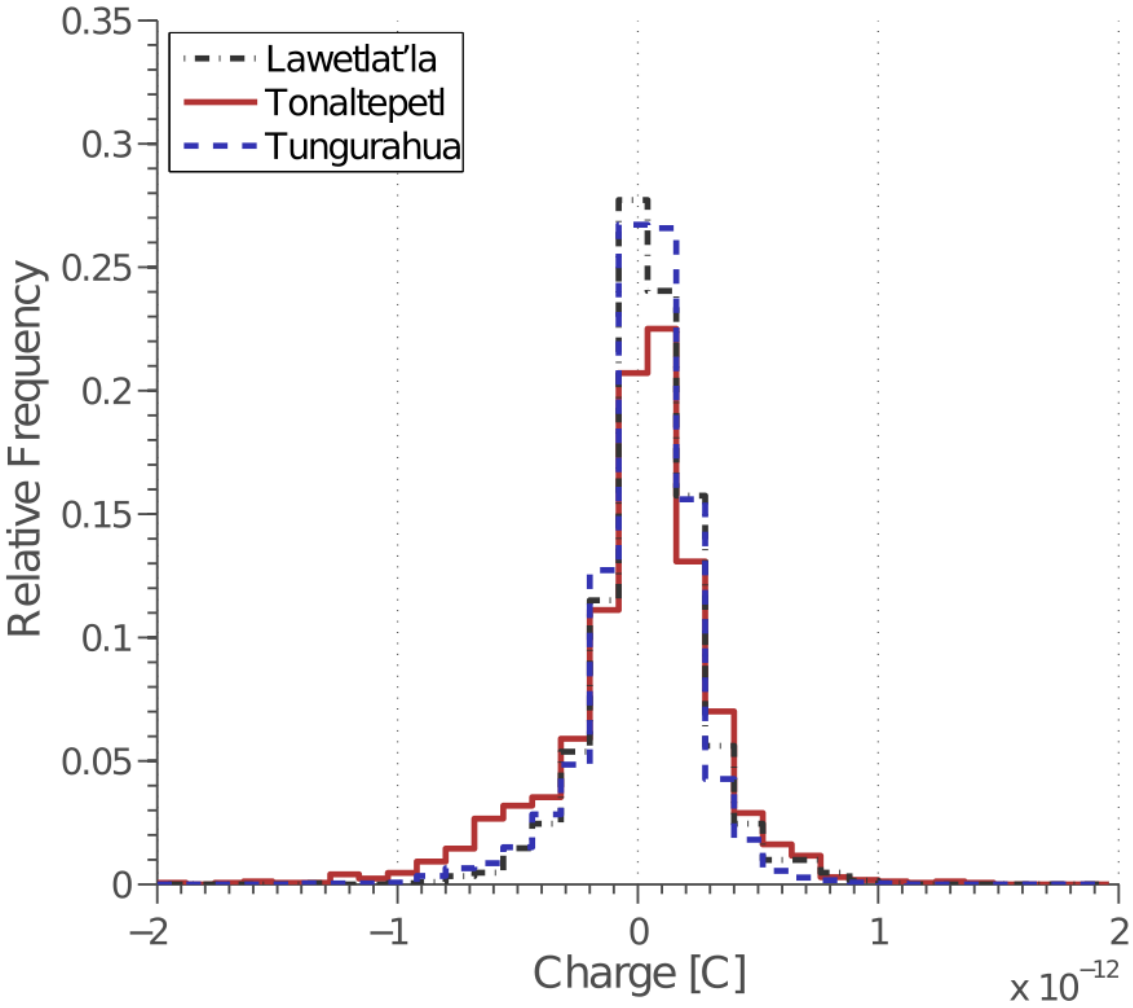

Figure 3.10: Typical charge distributions for the three ash samples. These distributions are from experiments run at the highest fluidization pressure (2.02 kPa). Notice that particles charge both positively and negatively. The charge on approximately 500-700 particles were characterized per sample.

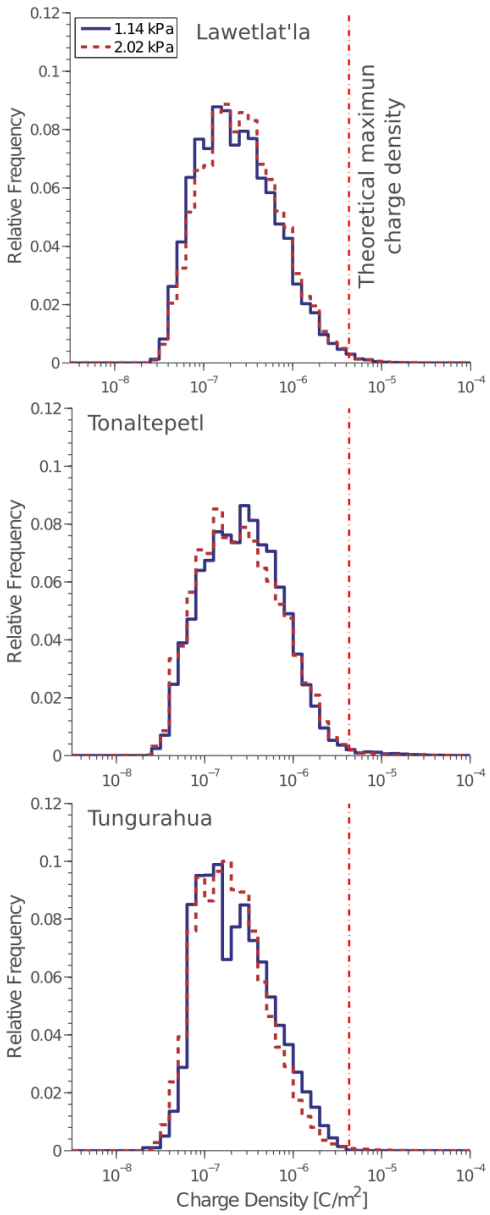

Figure 3.11: Absolute steady-state charge density distributions for the three samples for both the highest (red, dashed) and lowest (blue, solid) fluidization pressures. As can be seen, distribution of charges does not change with collisional rate per particle. The maximum charge density recorded is close to the limiting value of $4.3x10^{-}6Cm^{-}2$ (indicated by the red dashed lines). No great difference is discerned between the most and least energetic cases, suggesting that collisional rate and energy influences how fast the material charges but not the final electrostatic state.

transport) (Cross, 1987) (Matsuyama & Yamamoto, 2010), and/or the environmental conditions in which the flow takes place (Krauss, Horanyi, & Robertson, 2003) (Revel et al., 2003). For systems of particles which comprise a number of chemical species, the saturation charge may be limited by differences in relative work functions (Watanabe et al., 2006). Charge capping processes are less transparent in systems composed of identical dielectric grains. However, there is mounting evidence that environmental parameters largely determine the maximum charge on particles (Soares, Bertazzo, Burgo, Baldim, & Galembeck, 2008) (Burgo, Rezende, Bertazzo, Galembeck, & Galembeck, 2011). One of the dominant charge capping parameters in our experiments may be the breakdown limit of the atmosphere. The charge relaxation model, proposed by Matsuyama and Yamamoto (Matsuyama & Yamamoto, 1995) and supported by a number of experimental efforts (Matsusaka, Maruyama, Matsuyama, & Ghadiri, 2010), suggests that when two particles collide, some amount of charge is exchanged (this amount, as we have said, may increase with impact kinetic energy). As the grains rebound after contact, the potential difference between them increases. If separating particles are sufficiently charged, the potential between grains may rise above the Paschen curve, which represents the maximum potential that can be sustained between two charged bodies before breakdown occurs and is a function of both the pressure of the enveloping gas and the distance between the two surfaces (Raizer, 2011). When the particles' potential intersects the Paschen curve, some of the exchanged charge returns back across the gap between the grains. This process restricts the charge densities on the grains' surfaces to a constant, discharge-limited value. Charge relaxation is depicted schematically in Figure 3.12a. One of the principal consequences of the charge relaxation model is that a particle's equilibrium charge is determined by the atmospheric parameters; the flow energy, which sets the collision rate and perhaps the instantaneous charge transfer, merely serves to mediate how fast the potential curve is elevated to intersect the breakdown potential (Figure 3.12, b).

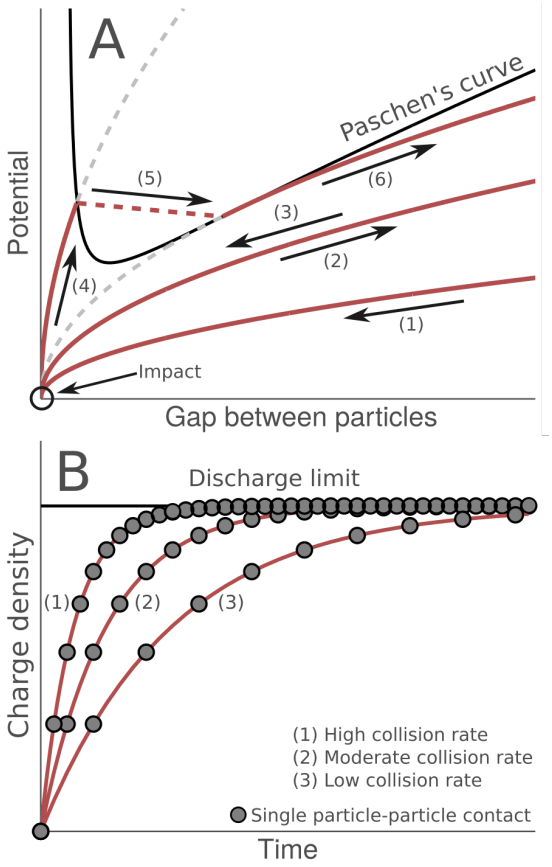

Figure 3.12: A) Schematic of charge relaxation model for a system of two particles modified from plotting the potential between two charged particles a function of distance between the grains. A particle with some initial charge approaches another particle along a potential curve that lies below the Paschen curve (1). At impact, some amount of charge is exchanged between the particles. Charged, particles rebound along another, steeper potential curve (2). No discharge occurs here because the potential curve remains below the Paschen curve. These two particles may again approach each other, impact and, exchange more charge (3). If this new charge is large enough, the particles will recede along a potential curve that intersects Paschen's curve (4). At this point, gaseous breakdown occurs (5) and some charge is recombined back across the gap until the particles' potential curve lies just tangent the Paschen curve (6). This potential curve (6) is representative of the maximum amount of charge that the particles can sustain in a given atmospherea limit independent of the dynamics of the system. B) Schematic representation of the time evolution of the charge on a particle with time according to the charge relaxation model (modified from). Grey circles represent individual contacts between particles and different curves represent different collision rates. During initial contacts, the particle exchanges some amount of charge but the total amount of charge remains below the discharge limit. After many collisions, the charge on the grain rises to the discharge limit.

In clean and dry conditions at sea level, the maximum field that can be sustained in air is approximately. This value, however, varies importantly as humidity (Nomura, Satoh, & Masuda, 2003) and pressure (Krauss et al., 2003) (Burgo et al., 2011) conditions change. The presence of particles in air can also depreciate the breakdown field, effectively limiting how much charge grains can collect (Al-Arainy, Malik, & Qureshi, 1994) (Deng et al., 2010) (Yao, He, Deng, Li, & Li, 2011) (Dascalescu, Samuila, & Tobazeon, 1996). Finally, the breakdown limit is different for different gases (Raizer, 2011). For our low-pressure nitrogen experiments, we computed the clean ionization field to be approximately using Paschen's Law (from tabulated constants reported in Raizer, Table 4.1 (Raizer, 2011)). This field corresponds to a maximum theoretical surface charge density (as computed from Gauss's Law, , where is the gas permittivity) of (for comparison, the maximum theoretical surface charge density is at sea level (Hamamoto et al., 1992)). The fact that the maximum charge densities recorded in our experiments approximate the maximum theoretical charge (demarcated by red vertical lines in Figure 3.12) hint that the steady-state charge distribution is controlled in part by the breakdown limit as described by the charge relaxation model.

If the breakdown of the gas is indeed responsible for capping the charge on grains regardless of flow energy, why are most particles charged well below the computed theoretical maximum charge? Several reasons likely contribute to this observation. Firstly, charge relaxation may not be related to a single breakdown curve. Ireland, 2007 (based on experimental evidence (Horn, Smith, & Grabbe, 1993)) has proposed that discharge onset and extinction are described by separate potential curves, with the extinction curve lying somewhat below the onset curve (Figure 3.13a, modified from Ireland (Ireland, 2009)). In this case, the steady-state charge on a particle is not restricted to a single discharge-limited value, but oscillates between values bracketed by the potential curve at extinction and the potential curve just below

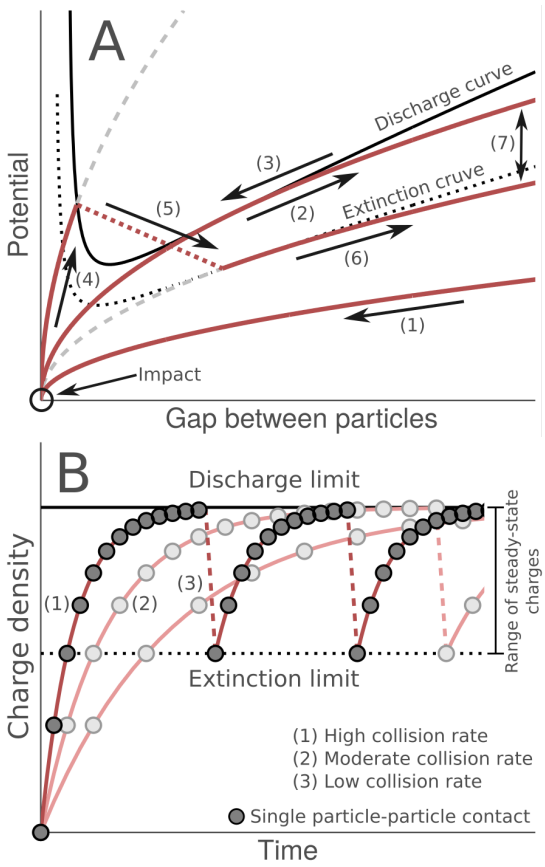

Figure 3.13: A) Proposed changes to the charge relaxation model as modified by Ireland (Ireland, 2009). A particle with some initial charge approaches another particle (or other surface) along a potential curve that lies below the breakdown limit (1). At impact, some extra amount of charge is transferred between the particles. The particles may again recede along a potential curve (2) that lies below or just below the discharge limit and no charge loss occurs. If the approach and collide again (3) gained charge may cause them to rebound along a potential curve that intersects the discharge curve (4). Once again, gaseous breakdown occurs and charge is recombined back across the gap (5). However, if the extinction curve (dotted, black) lies below the discharge curve (as suggested by experimental data of Horn, Smith, and Grabbe, 1993), the particles' potential may drop well below the discharge curve (6). Numerous additional particle collisions are then required to reach the discharge limit again (7). B) Schematic representation of the time evolution of the charge on a particle with time according to the charge relaxation model as modified by Ireland (Ireland, 2009). Grey circles represent individual contacts (with another surface or particle) and different curves represent different collision rates. After sufficient collisions, the charge on a grain rises to the discharge limit. Discharge causes the charge on the particle to fall to the extinction limit; because extinction is below the Paschen curve, additional collisions are required to produce subsequent discharges. At steady-state, the system is characterized by a continuous cycle of discharge and charge accumulation, resulting in particles with steady-state charges that take on a range of values, rather than a single one (figure modified from Ireland, 2009).

discharge onset (Figure 3.13b, modified from Ireland, 2009). Secondly, the apparent undersaturation may result from limitations inherent to the Faraday cup measurement setup. The maximum charge density () is derived by assuming that the charge on a particle's surface is of uniform polarity (the grain is covered entirely by either positive or negative charge carriers). Such assumption holds true for conductive surfaces on which charge is mobile; opposite charges readily neutralize each other and any excess charge (of a single polarity) is redistributed over the entire surface. Dielectric surfaces, on the other hand, can maintain coexisting patches of positive and negative charge for some period of time (Shinbrot, Komatsu, & Zhao, 2008) (Baytekin et al., 2011), with regions of one polarity masking the presence of others. This difference in charge retention between conducting and insulating grains is depicted schematically in Figure 3.14. The mosaic of charge on insulating surfaces occurs at the nanoscale (Baytekin et al., 2011) and is stable as long as the electric fields associated with it do not exceed the ionization limit. Recently, the patchiness nature of charge has been inferred to affect the dynamics of insulating grains of identical chemical composition (Lee & Jaeger, 2016). Because the Faraday tube employed in this work measures the overall charge (the sum of all the positive and negative regions) on a single particle passing through its volume, distinct regions of negative and positive charge on a grain's surface cannot be resolved even if these regions have surface charge densities close to the breakdown limit. Thus, a grain's total charge density will generally appear to be lower than the local charge densities.

To test the idea that the steady-state charge is controlled by the breakdown characteristics of the atmosphere, we ran a complimentary set of experiments with Tungurahua ash fluidized in an argon environment. The Paschen curve for argon lies below that of nitrogen (or air), meaning that the argon atmosphere has a weaker breakdown limit than nitrogen. Thus, one would expect to find smaller charges on particles fluidized in the argon environment than those run in nitrogen. A similar set

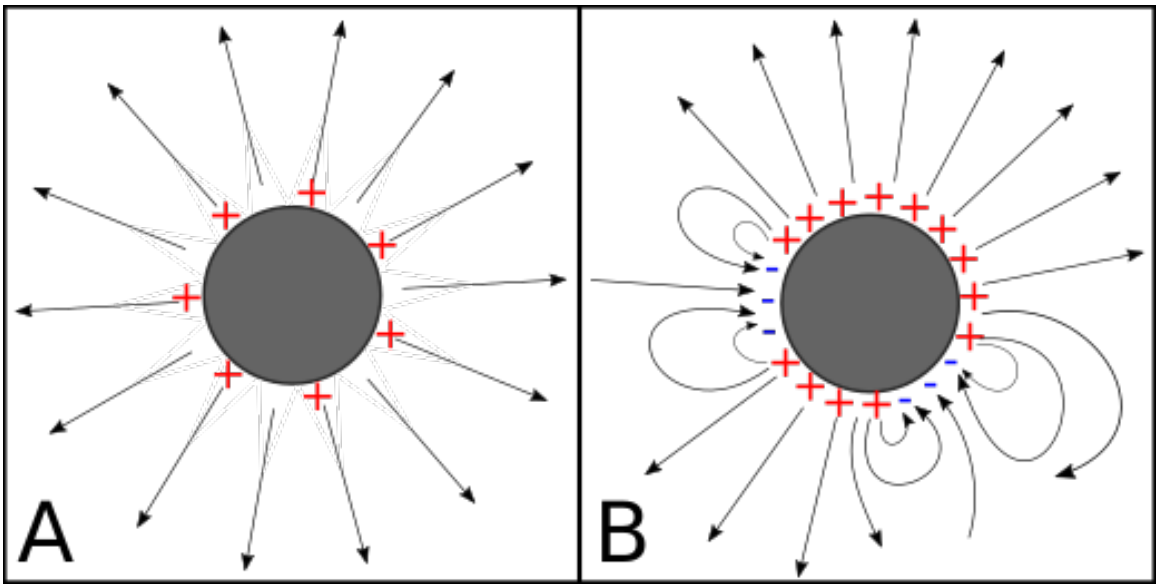

Figure 3.14: Schematic representation of a conductive and an insulating with the same net charge, but different local charge densities. A) A conductive particle allows for opposite charges to neutralize each other. Any excess charge is of a single polarity. B) An insulating grain may have coexisting patches of positive and negative charge. At the nano-scale the charge density may be close to the breakdown limit. Because the through-type Faraday cups measure the sum of all positive and negative charges on the grain, the charge density appears to be lower.

of experiments were conducted by Matsuyama and Yamamoto, 2010, however those authors used single particles rather than a granular flow. Based on the Paschen constants tabulated in Raizer, 2011 (Table 4.1), we compute that the maximum charge density on a surface in the clean low pressure argon atmosphere is. The distribution of charge densities from runs at the lowest and highest fluidization rates in both the argon (blue and dashed red) and nitrogen (solid grey and dashed grey) environments are plotted in Figure 3.15a. For reference, the theoretical maximum surface charge densities expected for both atmospheres (red: argon, light grey: nitrogen) are also rendered in Figure 3.15a. As in the nitrogen runs, we find that most particles have charge densities well below the theoretical maximum and can be explained by the processes previously discussed. However, the peak of the surface charge density distribution in nitrogen occurs at a value twice as large as that of argon. Interestingly, the theoretical maximum charge density of nitrogen is also approximately two times higher than that of the argon environment. We note that size distribution of particles sampled from the argon flow did not vary significantly from the distribution of particles sampled from the nitrogen flow (Figure 3.15b). Thus, the differences in charge density distributions do not likely stem from a size effect. The results of these last experiments support the premise that atmospheric properties, not dynamics, dominate the saturation charge in a granular flow.

3.3.4 The role of composition

The charging rates and charge densities are comparable for all three ash samples. This result supports previous studies which did not find strong correlations between the generation of lightning and magmatic composition (McNutt & Williams, 2010). While investigators have reported that triboelectric charging of synthetic materials is strongly affected by composition (Forward et al., 2009a), it is likely that the difference in chemistry between our samples may be insufficient to appreciatively modulate the

electrification. However, future work should explore the question of composition in greater detail.

3.3.5 Tribocharging in the volcanic context

Charge measurements on single particles have been performed by a number of investigators at erupting volcanoes. Gilbert et al., 1991 used an electrostatic separator to measure the charge on particles falling out of a plume at Sakurajima, obtaining surface charge densities near the theoretical maximum at sea level. Miura, Koyaguchi, and Tanaka, 2002 used a similar methodology at Sakurajima in 1995. These researchers found that particles were both positively and negatively electrified with maximum charge densities between . Like our measurements, the charge densities in that study had Gaussian distributions with zero means and the maximum charge density recorded approached the theoretical maximum for clean air at standard pressure and temperature conditions. Harrison et al., 2010 used a balloon sonde to make in-situ measurements of the charge environment in a 4 km-high Eyjafjallajkull plume. From their data, we estimate that the particles had maximum surface charge densities ranging from . The discrepancies in measured charge between campaigns may be attributed to the sampling location; while Gilbert et al., 1991 and Miura et al., 2002 collected data 2.5 5 km from the vent, the in-situ sonde data was obtained 1200 km away from the vent.

Our experiments show that as the energy of a granular flow is made larger, the particle collision frequency increases, resulting in more rapid or efficient electrification. Qualitatively, this behavior is similar to that observed by Behnke and Bruning (Behnke & Bruning, 2015) who suggest that electrical activity at Redoubt was modulated by changes in turbulent dynamics. In that study, the authors found that the rate of lightning production (which itself directly depends on the charging and charge segregation rates) can be linked to eruption energy. Namely, the highest discharge rates

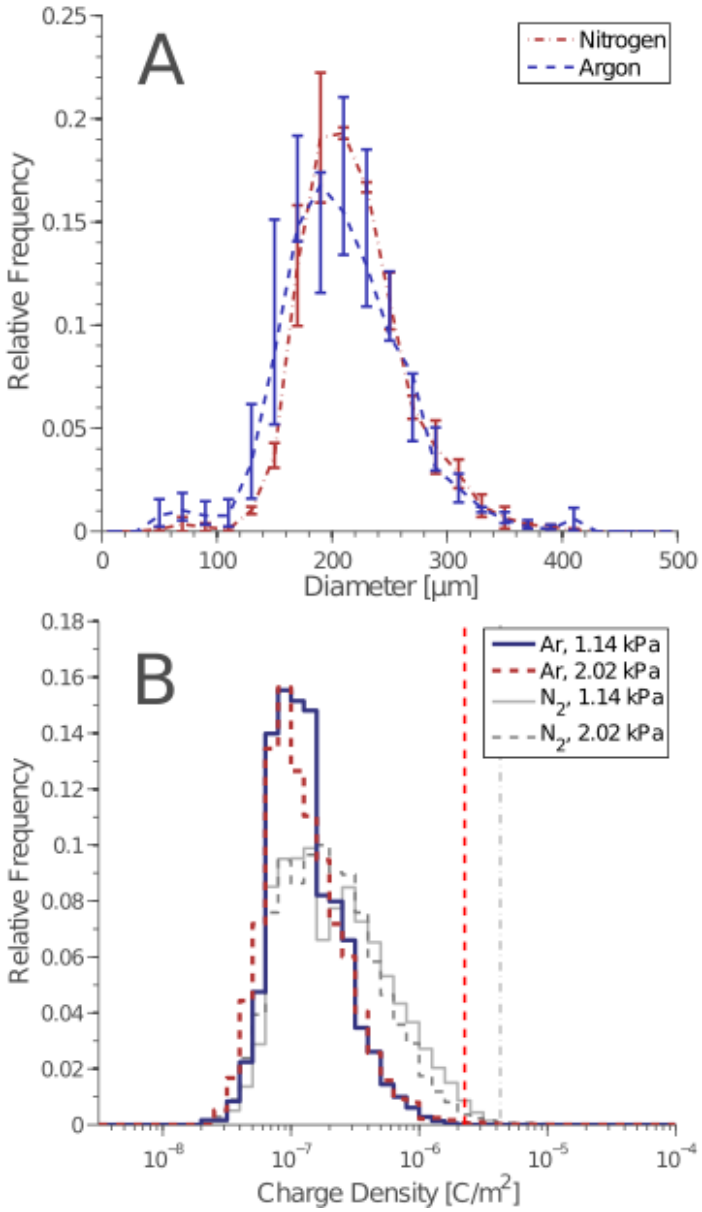

Figure 3.15: A) Absolute steady-state charge density distributions for the Tungurahua sample for both the highest (red, dashed) and lowest (blue, solid) fluidization pressures in an argon environment. The red, dashed, vertical line represent the maximum charge density in a clean argon environment. The grey curves are the charge density distributions for Tungurahua ash fluidized in nitrogen. Again, the distribution of steady-state charge densities in argon does not change with input energy. However, for the same energy range, particles in the argon environment charge to significantly lower levels than those in the nitrogen environment. These result indicate that the steady-state charge is mediated by the atmosphere breakdown properties. B) Comparison of size distributions from grains sampled from nitrogen (red, dotted/dashed) and argon (blue, dashed) flows reveals that differences in charge densities between gases is not related to a size effect.

in the Redoubt eruption occurred during the turbulent jet and convective phases when collision rates were likely high. Once gas-thrust forcing of the plume ceased, expelled ash fell subject to low-energy environmental winds causing collision and charging rates to drop. At that point, the authors described waning electrical activity. Analogous behavior was witnessed by Cimarelli et al., 2016 in Sakurajima plumes. This last work described a correlation between electrical activity and pressure at the vent. Although our work reinforces the idea that frictional charging is a primary electrification mechanism in plumes, triboelectric charging undoubtedly occurs in synchrony with other highly efficient electrification processes not specifically represented in our experiments. In the conduit and the gas-thrust regions, for example, triboelectric charging operates together with fractocharging, a process believed to impart a primordial charge to grains during the catastrophic breakup of the magma body. Much like tribocharging, many aspects of fragmentation charging are unconstrained. James et al., 2000 and Mendez Harper and Dufek, 2015 have shown that fragmentation charging is also a highly effective electrification mechanism capable of charging particles to their theoretical maxima and resulting in particle agglomeration. Furthermore, fractocharging is typically a very fast electrification process. As we have discussed, in a triboelectric-dominated process individual grains must undergo numerous contacts to reach charge levels close to the saturation limit. Depending on the collision rates (i.e. the energy of the flow), electrification may take a few milliseconds (Cimarelli et al., 2014) to several minutes, as in the present work. Conversely, fractocharging almost exclusively occurs on millisecond timescales because charge exchange or emission occurs solely fast during crack growth (Gonzalez & Pantano, 1990) (i.e. fractoemissions are not observed in slow fracture because emitted charge carriers have time to recombine with the newly created surface). Although electrification by fracture is undoubtedly present to some extent in all energetic eruptions simply because plumes are spawned by catastrophic fragmentation, the spatial and temporal distributions

of this mechanism are unknown. Beyond the conduit, fractocharging is likely constrained to regions where the collisional energy between pumice clasts is large enough to exceed the fragmentation criteria or result in copious comminution (Dufek, Manga, & Patel, 2012). Triboelectric charging, on the other hand, may be a more widespread electrification process because contact charging proceeds irrespective of whether material is being fractured or not as long as particles interact with each other. However, most rapid and efficient tribocharging likely occurs in regions where fractocharging processes are also present. Thus, determining the relative contributions of both mechanism becomes problematic (although some work suggests that frictional processes added to fracture electrification may in fact reduce the overall magnitude of charging (James et al., 2000)). We do note, however, that evidence exists to suggest that triboelectric charging involves spallation at the molecular scale, supporting the idea that frictional charging and fragmentation charging are but manifestations of a single process. With the available data, discerning the extent to which triboelectric charging and fractocharging contribute to the electrified state in a plume (or whether they are actually end members of a single process) remains difficult. Dedicated efforts should be undertaken to better constrain the relative efficiencies of these two mechanisms with or without the volcanic backstory. Outside of the conduit and gas thrust region in an expanding plume, tribocharging likely continues to electrify particles but at a decreased rate as collisions become less frequent and less energetic. Additionally, the rate of charge loss may become significant as the rising plume becomes more humid (Tada & Murata, 1995). At some point, the rate of triboelectrification in the plume likely slows enough to be dwarfed by other mechanisms, specifically those associated with the condensation and freezing of water. Strong evidence for ice-driven charging can be found in the data collected during the 2009 eruption of Redoubt.

Finally, the experiments in different gases, which effectively changed the discharge limit through Paschen's Law, suggest that the maximum amount of charge that can

be sustained by a particle in a volcanic plume depends on the properties of the surrounding atmosphere. Indeed, hypothetical volcanic plumes on other planetary bodies with distinct atmospheric compositions likely present different electrical behaviors than those on Earth. Charging rates in such plumes would depend importantly on the strength of the planetary atmosphere. Beyond gas composition, the Paschen limit of the gas is also affected by pressure. Thus, in a tall terrestrial plume (one which samples atmospheric pressures from near sea level to those near the tropopause), the maximum amount of charge that a constituent grain can sustain depends on where that grain is within the eruptive column. While charge exchange is efficient near the vent, the higher pressures in the region make the atmosphere more difficult to breakdown. The converse is true for altitude; charging may be hampered by infrequent collisions, but the thinner atmosphere may be easier to breakdown. Finally, the saturation limit, as has been stated, is also influenced by the number and size of particles present in the flow, temperature, and waterparameters which vary throughout the column. We hope to see experiments designed to explore how these parameters affect charging in volcanic systems.

3.4 Conclusion

Volcanic eruptions are often accompanied by lightning due to the charging of ash and/or hydrometeors associated with the volcanic plume. In this work, we have explored how fluidized samples of ash charge via triboelectric processes, documenting both the charging rates and steady-state charge densities as functions of the energy inputs into the system. In this work, great care was taken to isolate triboelectric effect resulting solely from particle-particle collisions. We demonstrate that the electrification behavior of volcanic material depends strongly on the average kinetic energy of the fluidized granular systems. Specifically, our experiments show that the time required to charge a parcel of ash (or other granular material) decreases with increasing

energy input. For the driving energies considered, the ash samples attain their equilibrium charges on the order of a few minutes. We ran experiments in both nitrogen and argon atmospheres. Across experiments conducted in the same gas, we find that the charge densities achieved constant equilibrium charge density distributions after several minutes of fluidization which were independent of the flow kinetic energy. The equilibrium distributions, however, changed dramatically between experiments run in different atmospheres. From these results, we infer that the steady-state charge in the granular media appears to be controlled primarily by the breakdown characteristics of the enveloping atmospheres, not dynamic processes in the fountain. Similarities between our experiments and those conducted with single particle impacts suggest that charge capping can explained by charge relaxation models. The fact that the gas composition plays an important role in charging may have implication for the generation of volcanic lightning on other planetary bodies. Our experiments and the results of other work (Cimarelli et al., 2014) show that triboelectric charging can be an efficient electrification mechanism in volcanic plumes. Because electrification by contact typically requires grains to undergo numerous collisions, triboelectric processes are likely most efficient in energetic regions of the volcanic system such as the conduit and gas-thrust region and may responsible for the generation of the so-called vent lightning (Thomas et al., 2007). While, the agreement between the dynamics-dependent electrical behavior in our work and that described during eruptions is compelling, we do note that the differences in scales, size distributions, and environmental parameters complicate a one-to-one comparison. Furthermore, other highly efficient charging processes, such as fragmentation charging, undoubtedly contribute to the electrostatic state of an emerging plume as well (James et al., 2000). Away from the vent, as the plume becomes more dilute, lower collisions rates likely limit the effectiveness of silicate-based tribocharging. In these regions, faster charging may be driven by electrification mechanism similar to those found in thunderstorms. Both of

these mechanisms are not accounted for in our work. Future experiments should be designed to specifically assess the relative effectiveness of triboelectric charging and other potential electrification mechanisms in plumes.

CHAPTER 4
DIFFERENTIATING THE ROLES OF TRIBOELECTRIC AND FRACTOELECTRIC CHARGING IN THE GENERATION OF VOLCANIC LIGHTNING

In review as: Méndez Harper, J., C. Cimarelli, V. Cigala, U. Kueppers, J. Dufek, and D. Gauidin (2017b), *Differentiating the roles of triboelectric and fractoelectric charging in the generation of volcanic lightning*, In Review.

4.1 Introduction

Lightning is commonly observed near the vent of an erupting volcano, suggesting that material is electrified efficiently in the conduit and in jet-thrust region (Thomas et al., 2007) (Behnke et al., 2013) (Aizawa et al., 2016) (Cimarelli et al., 2016). Two main charging mechanisms have been proposed to account for proximal electrical activity: 1) fragmentation charging accompanying both the brittle failure of the magmatic column and subsequent disruptive clast-clast collisions (James et al., 2000) (Mendez Harper & Dufek, 2015) and 2) triboelectric or frictional charging arising from particle-particle interactions (Houghton et al., 2013) (Mendez Harper & Dufek, 2016). Although experimental work over the last fifty years has served to elucidate the intricacies of these processes, the physics underlying both frictional and fracture-charging have not been described fully. Indeed, some work suggests that triboelectric and fragmentation charging may be end members of a single electrification process (Lacks & Sankaran, 2011). At present, more experimental work is necessary in order to settle such questions.

Despite the gaps in our understanding, the electrostatic behavior of systems in which material is clearly disrupted (the shattering of a glass pane, for example) can differ from that of systems where no apparent damage is observed (two surfaces

lightly osculating). James et al. (James et al., 2000), for instance, reported that simply breaking a material produces particles with larger charge magnitudes than the situation in which material is fractured and the fragments then interact frictionally. Furthermore, and perhaps more importantly, differences associated with how charge is distributed among particles of different sizes exists between fracto- and triboelectrification. Indeed, size-dependent bipolar charging (SDBC), by which smaller particles charge negatively relative to larger grains, is extensively reported in systems where friction dominates (Lacks & Levandovsky, 2007) (Forward et al., 2009b) (Forward et al., 2009a) (Lee et al., 2015) (Waitukaitis et al., 2014), but it is rarely associated with fracture processes (i.e. large and small particles are equally likely to carry positive or negative charge) (Dickinson et al., 1984) (Dickinson et al., 1988) (Gonzalez & Pantano, 1990) (Mendez Harper & Dufek, 2015). These differences are rendered schematically in Figure 4.1.

In the context of triboelectric charging, a consensus on the microphysical processes underlying SDBC has not been reached. One potential mechanism, proposed by Lowell and Truscott (Lowell & Truscott, 1986a) (Lowell & Truscott, 1986b), suggests that charge segregation based on size arises as electrons trapped in unfavorable, high-energy states on one surface transfer to vacant, low-energy states on another surface during particle-particle contacts. If small and large particles have the same initial surface density of high-energy electrons, smaller particles have fewer net high-energy electrons to give up than the larger ones. Thus, smaller grains receive more electrons than they lose, resulting in negative charging. Contrarily, large grains, with abundant high-energy electrons, have a net outflow of negative charge, acquiring positive charge relative to small grains. More recently, Gu et al. (Gu et al., 2013) have indicated that SDBC may not be driven by the exchange high-energy state electrons, but by the adsorption of water layers onto particle surfaces and the partitioning of OH^- and H^+ ions among small and large particles respectively. Under this model, partitioning

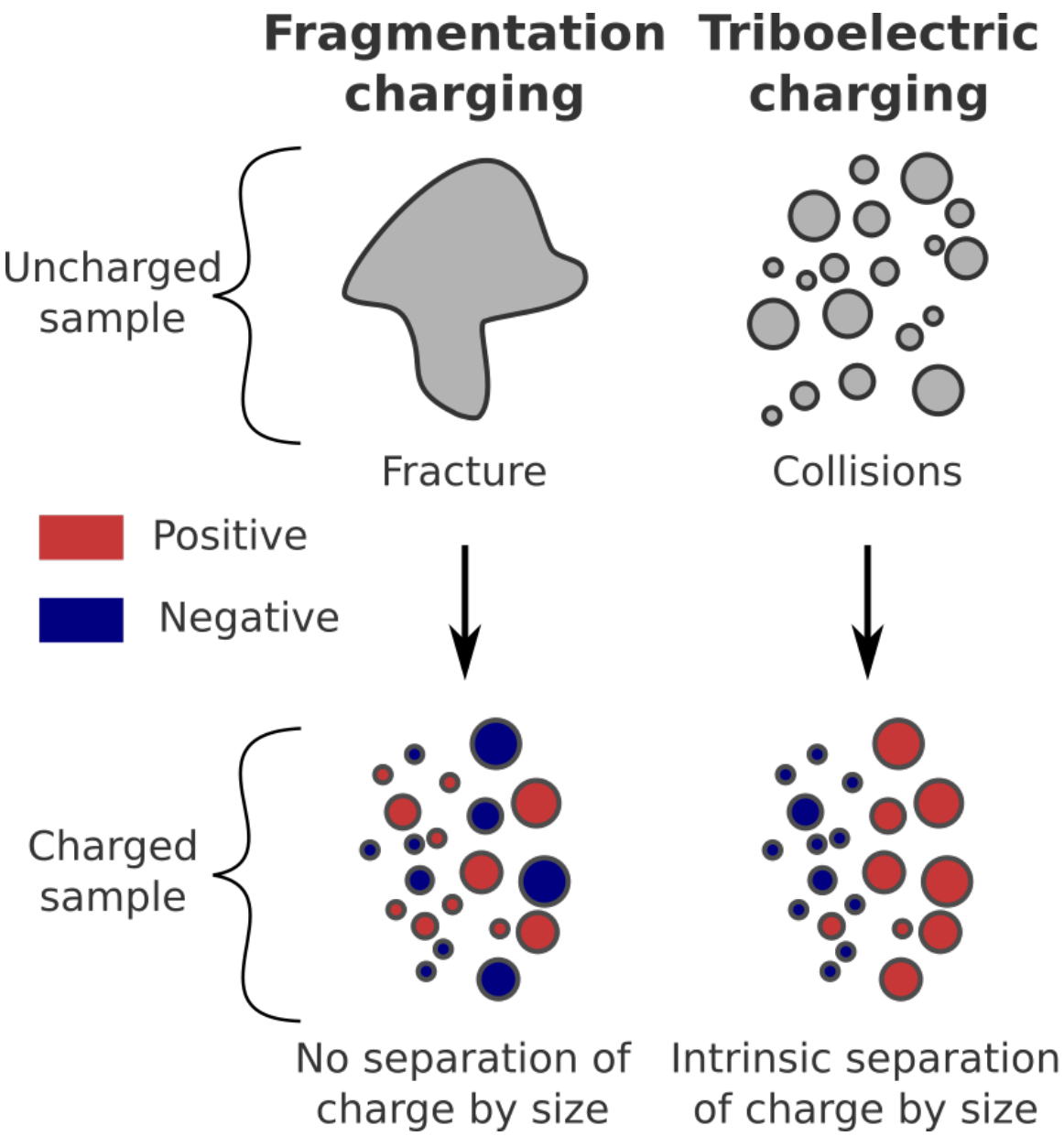

Figure 4.1: Schematic showing the difference in electrification behavior between tribocharging and fractocharging. Fragmentation processes (left) generate negative and positive charges distributed randomly among small and large grains. Conversely, triboelectric processes (right) produce charged flows demonstrating size-dependent bipolar charging, by which small particles charge negatively and large ones acquire positive charge.

of negative and positive charge is driven by the different mobilities of the hydrogen cation and hydroxyl anion, modulated by temperature differentials between small and large particles. This model has gained attention given that it can explain the non-linear relationship between atmospheric water content and charge magnitude on particles (Gu et al., 2013) (Xie et al., 2016).

Regardless of its microphysics, SDBC has been considered a critical processes in the generation of volcanic lightning because it provides a mechanism to efficiently separate particles of different polarities within the particle jet (James et al., 2000) (Behnke & Bruning, 2015) (Mendez Harper & Dufek, 2016). Indeed, compelling evidence for the importance of SDBC in volcanic flows can be found the shock-tube experiments of Cimarelli et al. (Cimarelli et al., 2014). There, the authors argue that discharges in scaled "volcanic jets" are dependent on the Stokes numbers of large and small grains. While large, momentum-driven particles remain concentrated in the center of the flow, small particles easily follow the diffluent eddies at the jet boundaries. If small and large particles maintain charges of opposite polarities, such size-based segregation would readily generate the large electric fields required to breakdown the intervening atmosphere. To test these hypotheses, the authors conducted experiments depleted in small grains. Without the small particles the jet became highly collimated and electrical activity was substantially diminished (Cimarelli et al., 2014).

Along with triboelectrification, fragmentation charging has been considered a principal electrification mechanism in volcanic eruptions. Yet, SDBC does not appear to be an inherent characteristic of fractocharging, complicating the generation of the coherent electric fields needed to produce spark discharges. Indeed, experiments have shown that when a material breaks, charged particles of both polarities (ions and electrons), as well as photons and neutrons, are emitted from the newly formed surfaces (Dickinson et al., 1984) (Dickinson et al., 1988) (Donaldson, Dickinson, & Wu, 1990) (Gonzalez & Pantano, 1990). This process, referred to as fractoemission, leaves

a patchwork of positively and negatively charged regions on a fragment's surface. To satisfy conservation of charge, the created area carrying negative charge must equal that carrying positive charge. Thus, probabilistically, many particles will have net charges close to zero coulombs. However, due to stochastic imbalances some grains will have a net negative or positive charge. Because newly created surfaces have no information about the size of the fragment they are attached to, a particle with non-zero charge, regardless of size, is just as likely to be positive as it is to be negative. We note that, while SDBC may not be an inherent property of fractocharging, fragments may display bipolar charging through secondary processes. Indeed, James et al. (James et al., 2000) hypothesized that, because particles of different sizes scavenge ions at different rates, large and small particles may acquire charges of opposite polarity. Additionally, Donaldson et al. (Donaldson et al., 1990) showed that charge generated though fractoemission can be separated in the presence of an electric field. Nonetheless, such bipolar charging hinges on parameters that may not always be available in volcanic plumes.

Here, we present the results of a series of experiments designed to further elucidate the links between tribo- and fractoelectric charging and volcanic lightning, as well as to ascertain whether or not SDBC is required to generate discharges in dusty flows. Our work demonstrates that while both mechanisms are capable of generating highly electrified particles, granular flows in which extensive fragmentation occurs (fractoelectrically-dominated system) generate fewer spark discharges than flows where particles comminute minimally (triboelectrically- dominated system). We find that frictionally dominated systems are more likely to generate discharges because of their inherent SDBC. This work, thus, directly relates discharge behavior to specific electrification mechanisms in a flow of volcanic ash for the first time. These findings are then used to reinterpret remotely captured lightning data obtained during the eruptions of Augustine (2006) and Redoubt (2009).

4.2 Methodology

The central piece of equipment used in this work was the shock-tube setup previously described by Cimarelli et al. (Cimarelli et al., 2014) to produce artificial volcanic lightning (Figure 4.2). The tube (20 cm in length, 2.8 cm in diamater) was loaded with approximately 75 ml of porous volcanic ash and then pressurized to 10 MPa with argon gas. Exceeding this pressure ruptured a set of diaphragms, causing the granular material to be ejected from the tube by explosive decompression. The process both fragmented the ash as gas expanded in pores and generated energetic particle-particle collisions in the subsequent jet. Such dynamics are analogous to those in the conduit and gas-thrust region of a volcanic jet. Thus, grains charged through a combination of tribo- and fractoelectric mechanisms. Each decompression event was recorded with a high-speed camera at a frame rate of 36000 fps, allowing us to capture discrete spark discharges in the flow. We employed industrially washed and sieved pumice quarried from deposits of the 13 ka Laacher See maar eruption in the Eifel Volcanic Field (Germany) with two different granulometries: fine (nominally 90-300 m) and coarse (nominally 300-1000 μm). Particle size distributions before and after each experiment were obtained with a Coulter LS230 laser sizer. Experiments were repeated four times with each granulometry.

Unlike previous efforts in which the shock-tube vented into a metallic collection chamber (Cimarelli et al., 2014), here we allowed the jet to expand into free air to minimize collisions between grains and foreign surfaces. A low-powered air stream was generated perpendicular to the flow 1 m above the nozzle. This artificial "wind" was used to deflect lofted particles away from the ejection axis (see Figure 4.2). Falling under the action of gravity, grains were sampled by two devices: 1) an array of eight miniature through-type Faraday cages (TTFC) capable of measuring the charge on individual grains previously described by Mndez Harper and Dufek (Mendez Harper

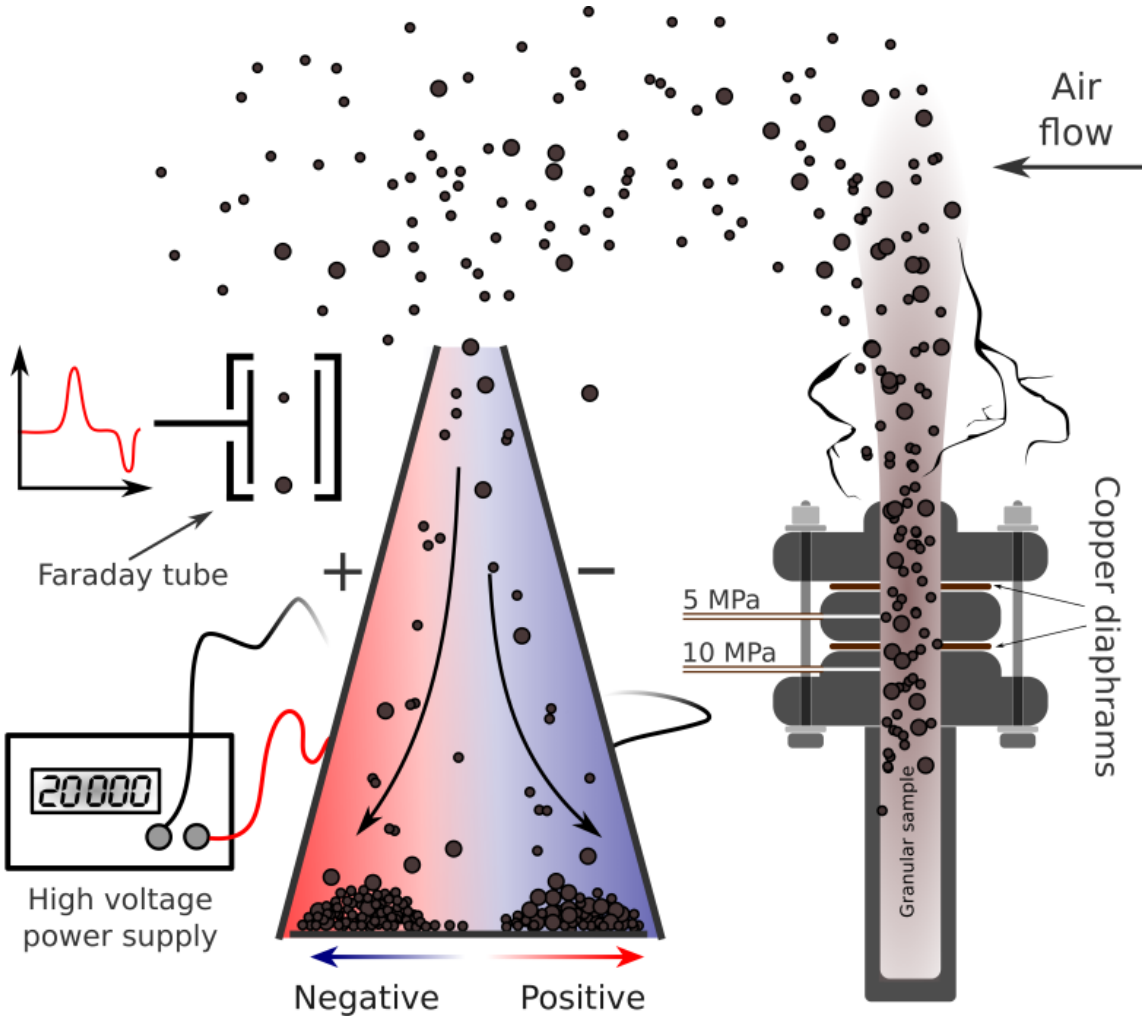

Figure 4.2: Schematic of experimental setup (See Cimarelli et al. (Cimarelli, Alatorre-Ibarguengoitia, Kueppers, Scheu, & Dingwell, 2014) and Méndez Harper and Dufek (Mendez Harper & Dufek, 2016) for more details).

& Dufek, 2016) and 2) an electrostatic separator consisting of two sub-parallel, 1 m-long copper plates with a potential difference of 20 kV between them. When a charged particle passed between these plates, its trajectory was modified by the imposed electric field. Negatively-charged grains were diverted toward the positive plate, while grains carrying positive charge drifted toward the negative plate. Thus, particles were separated by polarity and were collected in two bins placed at the base of the separator. Grains in each bin were then sized with an optical microscope to obtain spherical-equivalent diameters. Both the TTFC array and the electrostatic separator were placed 1.5 m downwind of the nozzle.

4.3 Results, Data, and Discussion

4.3.1 Evidence for different electrification mechanisms

Electrical discharges were observed in all experimental jets. The most evident difference in electrical behavior between the samples with fine grains and those composed of coarse particles involved the number of discharges produced per decompression event (see Figure 4.3a and 4.3b). Whereas experiments with the fine granulometry displayed innumerable small discharges, jets with coarse particles produced no more than a dozen discharges events per experiment. This observation is consistent with the findings of Cimarelli et al. (Cimarelli et al., 2014). Raw charge distributions (aggregating the data from the four experiments) for both granulometries are shown in Figure 4.4a (as measured by the TTFC). Particles charged both negatively and positively in both cases. Determining that a particular granulometry charged "more" than another based solely on charge data, however, is difficult because a grain's charge scales with the square of its radius. The propensity of a material to charge is better described by its surface charge density or the ratio of charge to surface area. The probability that a grain carries a particular charge density is given by the bivariate frequency distribution computed from the distributions of grain surface area and charge

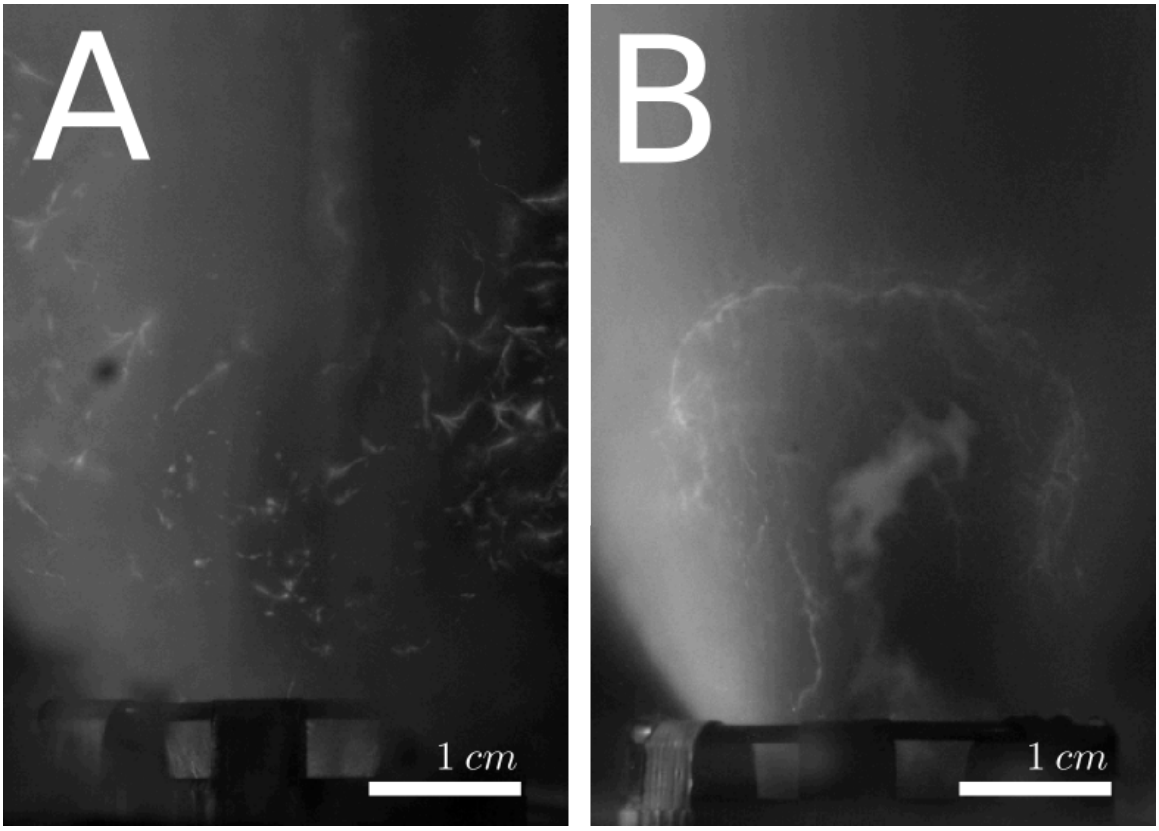

Figure 4.3: a) Composite image of all discharges in a flow with the fine granulometry. b) Composite of all discharges on in the flow with coarse particles. Composites span 10 ms.

(Mendez Harper & Dufek, 2016) (Mendez Harper, McDonald, et al., 2017). Cumulative charge density distributions for both granulometries are rendered in Figure 4.4b. Somewhat surprisingly, we find that experiments with both granulometries produced similar charge density distributions. Congruent with charge measurements during explosive volcanic eruptions (Miura et al., 1996) (James et al., 2000) (Mendez Harper & Dufek, 2016), both these distributions span several orders of magnitude: 10^{-8} - 10^{-3} Cm^{-2}. While the maximum charge densities registered in our experiments exceed the theoretical limit for flat surfaces (2.7×10^{-5} C m^{-2}), we note small particles (< 100 μm) can sustain charge densities well over 100×10^{-5} Cm^{-2} (Takahashi, Kobayashi, & Yamazaki, 1990) (Hamamoto et al., 1992).

The fact that experiments with both granulometries produced electrified particles

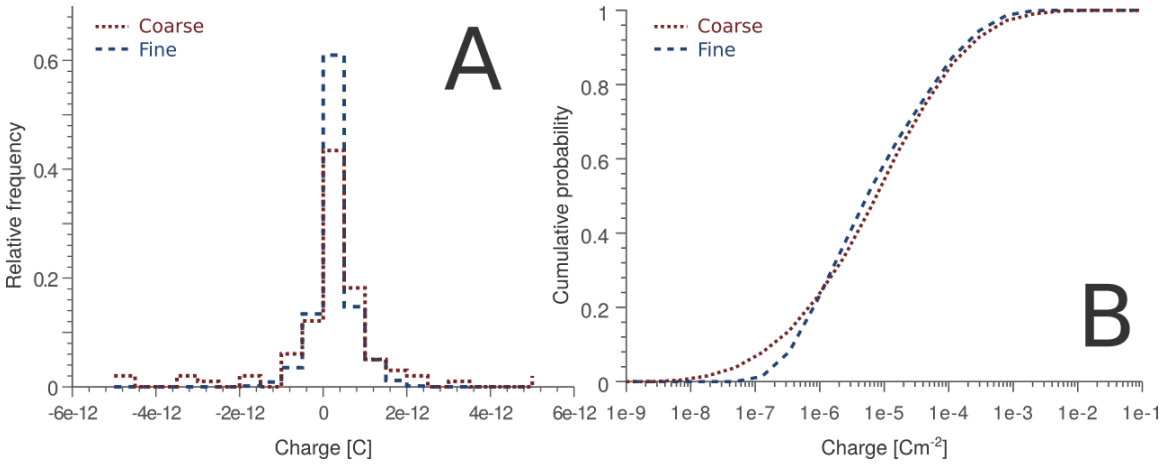

Figure 4.4: a) Distributions of raw charge for both fine and coarse granulometries. b) Cumulative charge density distributions for both fine and coarse granulometries.

with comparable surface charge density distributions, but generated notably different electrical responses is puzzling. This apparent contradiction can be explained, however, by relating particle size to charge polarity. The size distributions of negative and positive particles associated with the coarse and fine granulometries are rendered in Figure 4.5a and 4.5b, respectively (as measured using the electrostatic separator). Each distribution integrates size data from the four experiments. The most significant difference between the two graulometries is that there is no evident SDBC in experiments with 300-1000 μm grains, whereas it is clearly observed in the experiments with 90-300 μm particles. As we have discussed previously, size-dependent bipolar charging effectively generates the electric fields needed to breakdown air. Conversely, when SDBC is not present, charge is randomly distributed on particles of different sizes and the conditions conducive to breakdown are harder to achieve.

Particle size distributions before and after an experiment are shown in Figure 4.5c and 4.5d for the fine and coarse samples, respectively. What is immediately visible from Figure 4.5c-d is that there is a greater relative change in size in experiments using the coarse granulometry than in experiments with the fine granulometry. The higher propensity of coarse grains to fragment can be attributed to a size effect (Lajtai, 1972)

(Carter, 1992). During the decompression event, gas in the pores expands, placing stress on the surrounding material. Coarse particles are more likely to harbor larger voids than small particles. The presence of these large cavities reduces the failure stress, making coarse grains more likely to fragment under a given pore pressure. The increased probability of fragmentation (and the associated fractoelectrification) in flows with coarse grains would explain the absence of SDBC in these experiments. This behavior stands in contrast to that of jets with fine particles; the small change in particle size suggests that fragmentation charging played a lesser role in grain electrification. Indeed, the presence of SDBC and copious spark discharges observed in the jets with fine particle attests to a system controlled by minimally-disruptive frictional interactionsi.e. classical triboelectrification.

4.3.2 Fracto- and triboelectric charging in the volcanic context

In volcanic flowsespecially within the gas thrust regionboth triboelectric and fragmentation charging undoubtedly operate in concert, and likely coexist with other electrification mechanisms not addressed in this work (for example, inductive charging (Pahtz et al., 2010) or charging associated with radioactivity (Houghton et al., 2013)). While isolating contributions from each mechanism in a plumes overall electrical panorama remains complicated, the insight gained from our experiments allows us to reanalyze field data from novel vantage points. Succinctly, electrical phenomena observed during the Augustine (2006) (Thomas, Saleh, Guigon, & Czechowski, 2009) and Redoubt (2009) (Behnke, Thomas, Krehbiel, & McNutt, 2012) (Behnke & Bruning, 2015) eruptions suggest that the electrostatic behaviors associated with triboelectric and fractoelectric charging described above may be reflected at the large scale. For instance, the initial explosive phases of these eruptions were dominated by nearly-continuous radio frequency (RF) emissions in the VHF range (as measured by lightning-mapping arrays; LMA). Such emissions produced no visible signatures and

had sources at or near volcanic vents, suggesting they reflected charging processes in the volcanic conduits (Thomas et al., 2007)-perhaps, fragmentation charging. While, as we have said, the lack of SDBC in a fracture-dominated incipient jet may complicate the generation of large-scale spark discharges (i.e. lightning), the local electric fields near the surfaces of newly-created particles likely generate extensive corona discharge (by which charge is vented directly to the atmosphere) or small-scale sparks between grains. Referred to also as partial discharge, corona often generates such continuous RF emissions (Bartnikas, 1990), a property which has been exploited in industrial applications to detect failures in high voltage equipment (such as power transmission lines) (Moore, Portugues, & Glover, 2003) (Reid, Judd, Fouracre, Stewart, & Hepburn, 2011). Additional evidence that the "RF hum" emissions at Augustine and Redoubt were associated with fragmentation in the conduit resides in the fact that these signals abated as activity transitioned from explosive to passive venting (Thomas et al., 2007) (Behnke et al., 2013) (Behnke & Bruning, 2015). In other words, as explosive fragmentation concluded, so did the production of particles charged via fractoemission, resulting in a congruous drop in radiated VHF energy.

At both volcanoes, the end of explosive activity ushered in periods of relative electrical silence (as observed with LMAs) (Thomas et al., 2007) (Behnke et al., 2013) (Behnke & Bruning, 2015). These lulls were short-lived, however, and were filled a few minutes later by renewed RF emissions. Unlike the signals generated during the explosive phases, the new radiation consisted of discrete pulses representative of individual lightning strokes or spark discharges. A number of elements hint that triboelectric charging was at least partly responsible for electric activity during this phase. Firstly, the durations between the cessation of the continuous and impulsive RF and the initiation of discrete pulses (5-10 minutes) are consistent with timescales associated with triboelectric charging in experiments (Forward et al., 2009c) (Mendez Harper & Dufek, 2016). Secondly, lightning strokes had lengths of several hundred

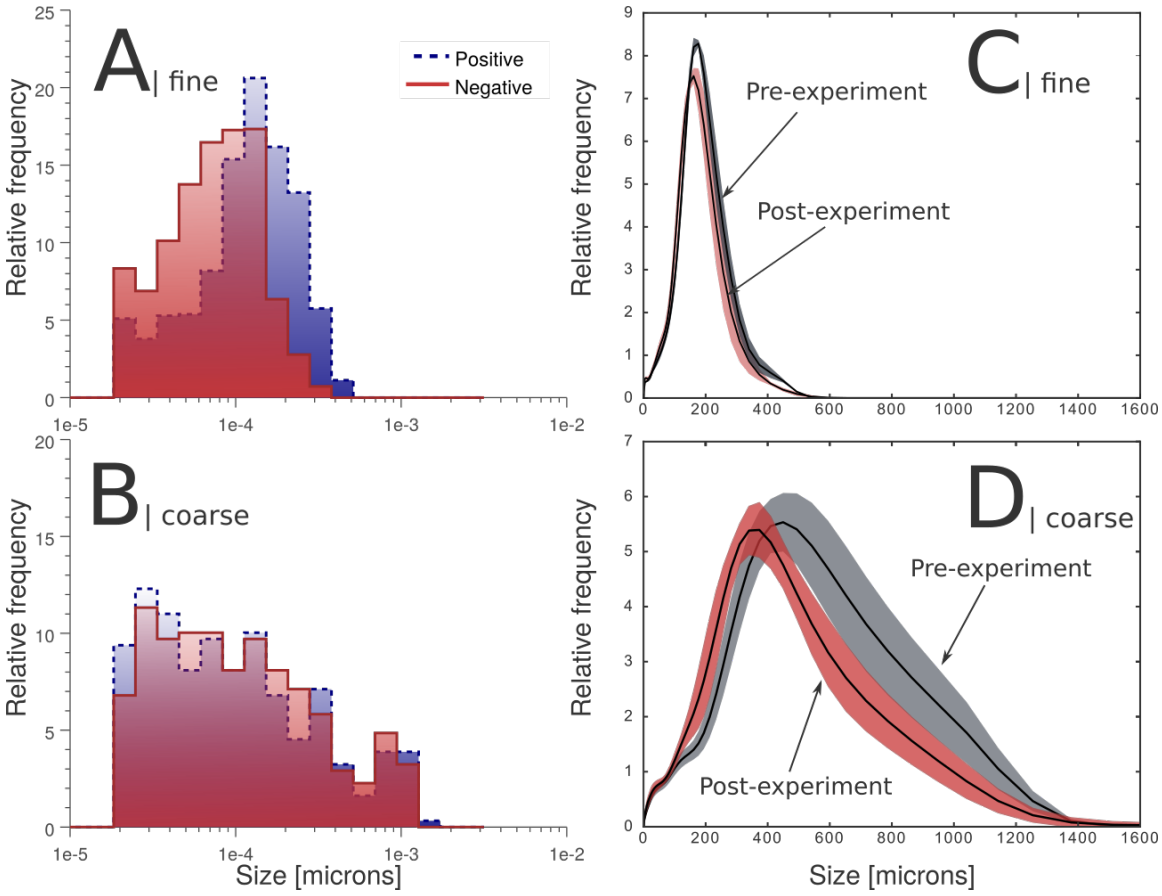

Figure 4.5: a-b) Size distributions associated with both negative and positive charges in both granulometries. Note the clear size-dependent bipolar charging in the experiments with the fine granulometries. SDBC is not observed in the experiments with the coarse granulometry. c-d) Total size distributions before and after experiments. Experiments with coarse grains undergo a greater degree of size reduction, suggesting that electrification in this case is driven by fragmentation. Such processes explain the lack of SDBC in these flows

of meters to several kilometers, suggesting the presence of efficient charge separation mechanisms. Such segregation could be achieved through SDBC and the separation of small and large particles by kinetic and gravitational effects. Thirdly, many of the discharges were concentrated in the downwind plume where the collisional energies associated with particle interactions would likely be too small to result in fracture. We note that the important differences in scale between our experiments and volcanic jets complicate direct comparisons between both systems. Indeed, as we have said above, other electrification mechanisms likely exist in real jets that are not represented in our experiments. Furthermore, the longer timescales involved in volcanic eruptions make it possible that charge segregation mechanisms other than SDBC may operate in nature. For instance, while the periods between the explosive and plume phases at Augustine and Redoubt were extended enough to allow triboelectrification, they were also sufficiently long to allow charge to be segregated via alternate processes such ion harvesting (James et al., 2000) or those involving hydrometeors (Arason et al., 2011) (Nicora et al., 2013). The short timescales of the shock-tube experiments (<1 s) and absence of ice in our experiments preclude us form commenting on the effects of these secondary processes. Regardless these limitations, however, our experiments do provide a focused glimpse of the roles individual electrification mechanisms play in the generation of volcanic lightning for the first time. Our work suggests that 1) triboelectric and fractoelectric charging are indeed separate mechanisms and that 2) their unique signatures can be identified within complex granular flows like volcanic jets.

4.4 Conclusions

Here, we have shown that triboelectric and fragmentation charging, while generating highly charged particles, demonstrate unique electrostatic behaviors. Specifically, fracture processes produce charged particles which may be negative or positive irre-

spective of fragment size. The resulting chaotic charge distribution among particles complicates the production of large-scale spark discharges the unless secondary processes (such as ion scavenging) are present, but may be conducive to extensive corona generation or visually-imperceptible sparks between individual grains. Conversely, triboelectric charging inherently demonstrates size-dependent bipolar charging, facilitating the existence of coherent electric fields in a granular flows as particles of different sizes carrying charge of opposite polarity are separated. Corona discharge associated with the fragmentation of the magma body could explain the nearly-continuous radio frequency emissions observed during the explosive phases of Augustine and Redoubt eruptions. The transition to more impulsive RF emissions (associated with lightning strikes in the plume) concluding the explosive phases of these volcanoes suggests the activation of efficient charge segregation mechanisms. One possibility is that the volcanic systems transitioned to triboelectric regimes under which particles underwent frictional, but minimally disruptive interactions, and where size-dependent bipolar charging became active.

CHAPTER 5
INFERRING THE STRUCTURE OF SUPERSONIC VOLCANIC JETS FROM ELECTROSTATIC DISCHARGES

Submitted as: Méndez Harper, J., J. Duefk, C. Cimarelli, R. Thomas, and D. Gauidin (2017c), *Inferring the structure of supersonic volcanic jets from discharge timing and location*, Submitted.

5.1 Introduction

Electrostatic processes are a common in volcanic eruptions (Hatakeyama & Uchikawa, 1951) (Thomas et al., 2007) (McNutt & Williams, 2010) (Aizawa et al., 2016) (Cimarelli et al., 2016). Although the microphysics of granular electrification have not been described fully, recent field campaigns have described pathways linking granular hydrodynamics to electrical responses in volcanic flows (Behnke et al., 2013) (Behnke & Bruning, 2015) (Woodhouse & Behnke, 2014) (Cimarelli et al., 2016). Understanding these connections remains a prominent goal in volcanology because electrical activity can be monitored remotely. Thus, lightning may serve as a tool to probe the internal, obscured dynamics of large eruptive flows (James et al., 2000). Indeed, observations during the Augustine (2006) and Redoubt (2009) eruptions suggest that electrostatic processes co-evolve with changes in flow behavior (Thomas et al., 2007) (Behnke & Bruning, 2015). In particular, both Alaskan peaks produced two distinct electrical behaviors during their eruptions: 1) initial, quasi-continuous outbursts associated with individual explosions followed by 2) more intermittent, although spatially-extensive, lightning storms in maturing plumes. The second modality, comprising near-vent and plume lightning, typically generates brilliant flashes several hundreds of meters to kilometers in length and emits impulsive radio frequency (RF) signals (Fig. 5.1a). Lightning in this modality occurs anywhere between a few hundred of meters above

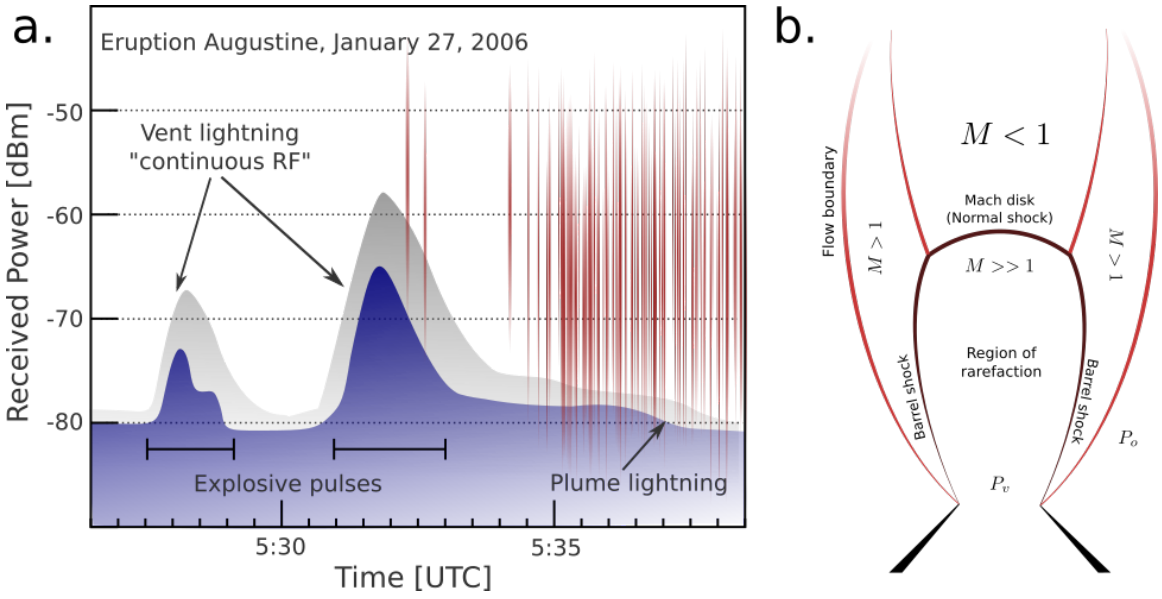

Figure 5.1: Electrical activity during the 2006 eruption of Augustine and the structure of an underexpanded jet. a, Data collected with a Lightning Mapping Array during the January 27, 2006 eruption at Augustine (Thomas et al., 2007) showing the spectral differences between vent and plume lightning. While plume lightning manifests itself as discrete, impulsive signals (red, vertical lines), vent activity appears as a "continuous" signal rising from the noise floor. As can be seen, vent-lightning signals correlated with the duration of explosive events (one at 0528 UTC, a second at 0531 UTC). Figure modified from Thomas et al., 2007. b, Structure of an under-expanded jet, showing the region of rarefaction between the vent and the normal shock.

the vent to kilometers away in the distal plume. Because of their discernible nature and similarity to thundercloud lightning, both near-vent and plume lightning have been the focus of the most recent volcanic lightning studies (Cimarelli et al., 2016) (Aizawa et al., 2016) (Van Eaton et al., 2016). In contrast, the first modality lightning, referred to as vent discharges, are more obscure. Revealing themselves en masse as a persistent RF hum at a distance, vent discharges have been described as a myriad of small, visually-inappreciable flashed located at or just above the volcanic vent (Thomas et al., 2007) (Behnke et al., 2013). Interestingly, proximal discharges seem to fall in tempo with discrete explosions (Fig. 5.1a) and the rate of discharges increases with the magnitude of overpressure at the vent (Thomas et al., 2007) (Behnke & Bruning, 2015).

The proximal loci and timing of vent discharges suggest that this electrical activity directly reflects processes at the volcanic source. The small length-scales and high rates (several dozen events per millisecond) associated with vent discharges hint that the volumetric charge density in proximal volcanic jets may be as much as an order of magnitude larger than that found in thunderclouds or distal plume regions (McNutt & Williams, 2010) (Aizawa et al., 2016). This is perhaps unsurprising given that explosions likely generate large amounts of charge per unit surface area through elevated rates of fracto- and triboelectric charging (James et al., 2000) (Cimarelli et al., 2014). Thus, proximal discharges likely reflect conventional or dielectric breakdown processes11. Yet, abundant electrical activity may not only reflect efficient charging mechanisms in the conduit and jet-thrust region. Indeed, here we show that the compressible fluid dynamics associated with powerful explosions contribute significantly to discharges in proximity to the vent.

5.2 Background and Methods

Energetic volcanic blasts often produce flows which are supersonic and overpressurized or underexpanded (Ogden, Wohletz, Glatzmaier, & Brodsky, 2008) (Kieffer, 1981) (Orescanin, Austin, & Kieffer, 2010). Such conditions occur when the pressure at the vent is higher than the ambient by at least a factor of 2 (Orescanin et al., 2010). Upon emerging from the conduit, the jet undergoes Prandtl-Meyer expansion, accelerating to elevated Mach numbers (i.e. supersonic) and decreasing rapidly in both density and pressure (Ogden et al., 2008) (Owen & Thornhill, 1948) (Adamson & Nicholls, 1959) (Orescanin & Austin, 2010). Indeed, the pressure in the flow may drop below atmospheric by up to one or two orders of magnitude (Fig 5.2a) (Ogden et al., 2008) (Orescanin et al., 2010). This rarefaction is expected to have important consequences for breakdown processes in the jet. According to Paschens Law, the maximum charge density, Q/A, on a surfacethat is, the number of charge carriers per unit areathat can

be sustained by an enveloping gas before conventional electrical discharge proceeds is roughly inversely proportional to pressure (for pressures of up to 13-20 atmospheres) (Paschen, 1889) (Dwyer & Uman, 2014) (Manning, ten Kate, Battel, & Mahaffy, 2010) (Helling, Jardine, Stark, & Diver, 2013). At sea level, for instance, the charge density at breakdown, $Q/A_{max} = \epsilon_r \epsilon_o E_{breakdown}$ (here, ϵ_r is the relative permittivity of the gas, ϵ_o is the permittivity of free space, and $E_{breakdown}$ is the breakdown field), has a value of 2.66×10^{-5} Cm^{-2} (Hamamoto et al., 1992). At 6 km above sea level, however, the theoretical maximum charge density is about half this value (Marshall, McCarthy, & Rust, 1995). In underexpanded jets, as the pressure in flow downstream of the vent decreases, so does the breakdown strength of the gas. In other words, the maximum sustainable pressure on surfacesash particles, for instance–traversing through this region is expected to diminish with distance away from the vent.

Rarefaction in underexpanded jet, however, does not proceed indefinitely, but terminates in a normal shock (Mach disk) (Ogden et al., 2008). There, the fluid speed becomes subsonic and a sudden increase in pressure and density takes places (Fig. 5.1). During this stepwise jump in pressure, there is a corresponding increase in the breakdown strength of the gas. The position of the shock has been shown to be function of the vent diameter d_v as well as the overpressure factor $K = P_v/P_o$ (where P_v is the pressure at the vent and P_o is the atmospheric pressure) (Ogden et al., 2008) (Kieffer, 1981) (Adamson & Nicholls, 1959) (Orescanin & Austin, 2010). For a pseudo-gas approximation relevant to volcanic eruptions, the elevation of the Mach disk has been described as: $h = C d_v K^{0.5}$, where C is a constant with values ranging between 0.67 and 0.85 (Ogden et al., 2008) (Orescanin et al., 2010). Using this relation, the pressure variations in jets for $C = 0.85$, $K = 2, 5, 10$ and $d_v = 100m$ is exemplified in Fig. 5.2b. While details of this expression will change as the pseudo-gas assumption is relaxed, the general form of this expression should remain valid. The amount of fine-grained particles available in most volcanic eruptions suggests that this expression is

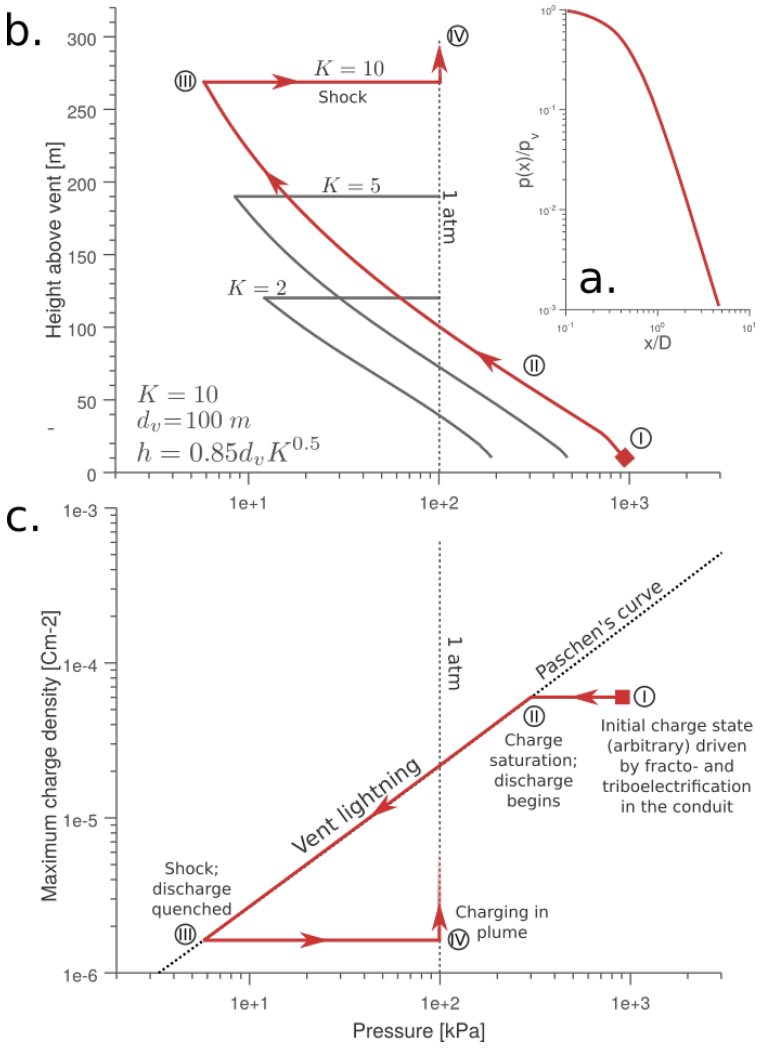

Figure 5.2: Variation in pressure within the underexpanded jet and associated electrostatic effects. a, Normalized pressure variation along the centerline of the jet as a function of distance normalized by the vent diameter (modified from Owen and Thornhill (Owen & Thornhill, 1948)). b, The pressure variation in a jet as function of altitude for 3 different K factors, 2, 5, 10, for and . Note rarefaction during the expansion and the stepwise recompression at the shock. c, The proposed discharge mechanism in a jet with K = 10. A grain at high pressure starts off undersaturated in charge. As the pressure in the jet drops during expansion, the ability of the gas to hold charge is also diminished. At some point, the potential on the particle intersects the Paschen curve and discharge is initiated. Charge loss continues as long as the pressure continues to drop. At the shock, the pressure rapidly climbs and discharge is cut off. Subsequent charging is due to electrification in the plume.

likely appropriate for many eruptions. To gain a qualitative understanding of how changes in pressure influence the charge structure of a jet, consider the case when K = 10 (Fig. 5.2b). For this overpressure, the theoretical maximum charge density that can be collected by a surface is 10^{-4} Cm^{-2} (see Supplementary material). For arguments sake, assume that mechanisms in the conduit are not completely efficient and the material emerges from the vent in an undersaturated condition (point I in Fig. 5.2c). Because the charge density is below the Paschen limit (noted in blue), the surfaces electrostatic state is stable; the grain does not lose charge. However, as the jet expands and the pressure drops, the ability of the atmosphere to retain charge depreciates. At some pressure (point II in Fig. 5.2c), the value of particles charge density intersects Paschens curve. Here, the parcel finds itself in a charge saturated condition. Any further reduction in pressure results in discharge to keep the charge density just below the Paschen limit. When two particles of opposite charge get close they will produce a strong electric field that can go above the Paschen limit and there will be a spark discharge between the two and the length-scales of discharges are expected to be small. Discharge processes are maintained as long as the pressure in the jet continues to drop. Note that higher overpressures at the vent lead to deeper pressure overshoots and require ash surfaces shed greater amounts of charge (Fig. 5.3). Upon reaching the shock, the pressure in the jet increases precipitously. Charge loss is abruptly cut off as the Paschen limit climbs well above the potentials associated with the charge-depleted grain (point III). The shock effectively quenches the discharge. Past the shock, the undersaturated grain may again collect charge as it undergoes collisions with other particles in the plume or as other electrification mechanism become active (point IV). The tight coupling between fluid dynamics and electrostatics processes described above suggests that vent discharges retain information on the structure of the overpressurized volcanic jet. We find compelling evidence for this interplay using the experimental apparatus described by Cimarelli et al., 2014.

The setup consists of a shock tube capable of holding 200 cm^3 of volcanic ash. For these experiments, we employed commercially-processed pumice (from the Laascher See volcano in Germany) with a nominal grain size of 90-300 μm. The material was pressurized (to a pressure of 10 MPa) in the shock tube, then ejected by explosive decompression (a process comparable to a volcanic explosion). This process generated a dusty jet with abundant electrical discharges (Fig. 5.3c and 5.3d). Using a high-speed cameras and pressure transducers we inferred both the geometry of the structure of the jet and the tracked spark discharges in the flow. We find that discharges exclusively occur within the region of rarefaction (between the vent and the normal shock) where the dielectric strength of the atmosphere is weakened (Fig. 5.2b). Thus, the maximum elevation of discharges place constraints on the location of the first normal shock, and by extension, the structure of the supersonic jet. Because the gas-particle flow is sourced from a finite reservoir, the underexpanded jet structure collapses with time (Orescanin & Austin, 2010) (Orescanin & Austin, 2010). This causes the region of rarefaction (and the Mach disk) to ultimately shrink toward the vent. Such process is also recorded in the discharge data in our experiments; the maximum elevations of discharges in the flow decreased over time. As the shock structure disappeared completely, electrical activity ceased.

5.3 Discussion and Conclusions

Campaigns at erupting volcanoes report electrical activity analogous to that observed in our experiments. At both Augustine4, Redoubt5 vent discharges were registered during explosions with strong acoustic and seismic emissions suggesting overpressures at the vent (Fig. 5.1; see methods). Additionally, geometrical analysis of explosive-phase signals imply that vent discharges occurred within a few tens-to-hundreds of meters of the vent (Thomas et al., 2007) (Behnke et al., 2013). These altitudes are consistent with the inferred locations of the equilibrium shock associated with

individual explosions (as inferred from infrasound data). Indeed, for the largest events at Augustine and Redoubt, we estimate that the shocks would have had elevations of 50 and 200 m, respectively (see methods). Abating seismic and acoustic signals marked the end of overpressure conditions at the vents. As the flows became pressure-balanced, the regions of rarefied gas in the jets would have collapsed, increasing the dielectric strength of the gas and limiting the probability of discharge. The fact that the RF hums associated with vent discharges concluded at the end of the explosive phases (Thomas et al., 2007) (Behnke et al., 2013) (Behnke & Bruning, 2015) is consistent this hypothesis.

Between the vent and the shock, the charge density on grains is required to decrease by several orders of magnitude (Fig. 5.2). One implication of this deep charge loss is that the normal shock separating the supersonic jet and the overlying subsonic plume represents a barrier across which a large fraction of the electrostatic history is lost. Thus, while fragmentation and triboelectric charging may be very efficient in the conduit and just above the vent, they primarily drive electrostatic processes in the proximal regions of the plume (provided the eruptive source is over-pressurized relative to the atmosphere). Such inferences find support in some observations. At Augustine, large-scale plume lightning did immediately follow the eruptive phases, but was delayed for several minutes after the conclusion of vent discharges (Fig. 5.1 a) (Thomas et al., 2007). These doldrums suggest that material was depleted in charge upon leaving the gas-thrust-region and that time was required for alternate electrification and breakdown mechanisms (perhaps, involving ice) to come into effect (Arason et al., 2011) (Nicora et al., 2013). However, other eruptions have displayed more complex behaviors. At Redoubt, for instance, a distinction between vent and plume lightning phases also existed, but it was less obvious (Behnke et al., 2013), whereas at Sakurajima no time delays existed between onset of eruptions and large scale spark discharges (we note that published investigations at Sakurajima did not

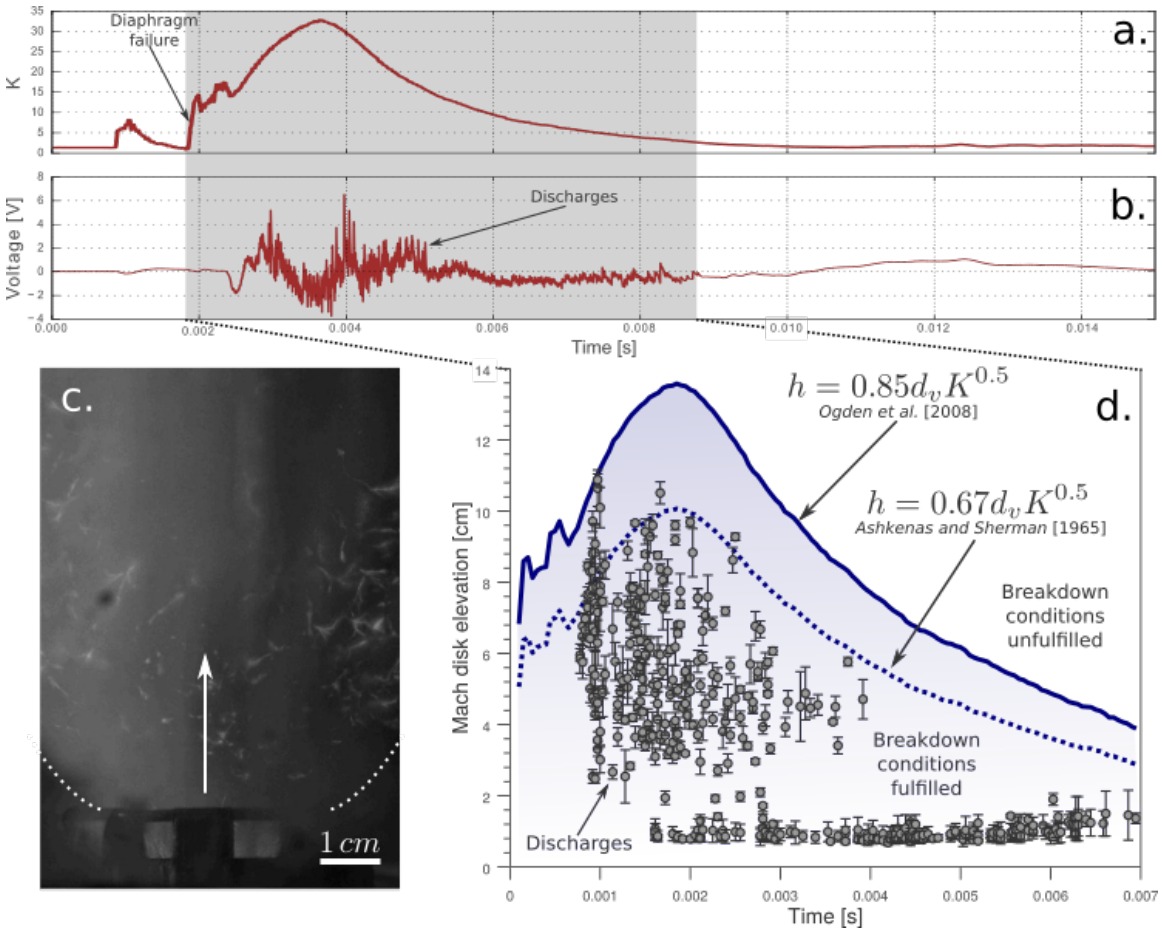

Figure 5.3: An experimental visualization of vent discharges. a, Overpressure factor, K, at the vent during a shock-tube experiment. b, Discharges as recorded by the electrostatic ring sensors as high-frequency pulses. Note that discharges appear only when overpressures exist at the vent. c, Time-lapse photograph (6 ms) of all discharges observed in the scaled jet. d, Location of discharges in the underexpanded jet as a function of time. For all time, discharges remain in the region bounded between the vent (at y = 0 cm) and the normal shock (solid or dotted lines) because this area satisfies the conventional breakdown criteria. As the shock structure collapses, the elevation of discharges also decreases. Discharges are extinguished as the overpressure factor approaches K=2.

involve the acquisition of LMA data (Aizawa et al., 2016) (Cimarelli et al., 2016) and, as such, we are unable to comment on the existence of RF hum during explosions). The extensive spark discharges in Sakurajimas jets (hundreds of meters long) imply that efficient charge separation mechanisms became active in concert with energetic blasts. These variations in discharge behavior likely reflect processes that are not accounted for in our model. For instance, the overlapping explosive and plume phases at Redoubt may underscore long explosive phases or pulsing at the vent(Behnke et al., 2013) (Behnke & Bruning, 2015) while the immediacy of spark discharges at Sakurajima may be indicative of broader grains size distributions in the jet allowing for the generation coherent electric fields with enhanced efficiency (Cimarelli et al., 2014) (Forward et al., 2009a). Future investigations at volcanoes using a diverse set of instruments, including infrasound transducers, LMA, and electric field meters, will undoubtedly help clarify some these questions.

5.4 Supplementary material

5.4.1 Pressure variation in a underexpanded jet

The pressure drop with distance from an underexpanded nozzle has been described in detail by Owen and Thornhill (Owen & Thornhill, 1948) and Adamson and Nicholls (Adamson & Nicholls, 1959). Using the numerical method of characteristics, Owen and Thornhill tudied the pressure variation in an overpressured jet venting into vacuum (Fig. 5.2a). Those authors showed that their result represented "a universal solution, in so far as it applies to that area, of any similar jet with a finite pressure ratio, $K = P_t/P_o$ (i.e. the ratio of the atmospheric pressure to total pressure), which is bounded by the orifice and the first wave front from the orifice boundary which registers the existence of an external pressure outside the jet"(Owen & Thornhill, 1948) In other words, the pressure variation as a function of distance from the vent prior to the Mach disk, $P(x)/P_v$ (where $P(x)$ is the static pressure at some point

downstream of the jet and P_v is the static pressure at the vent), should hold for all K ratios and the size of the region of similarity increases with an increasing pressure ratio (Fig. 5.3a). Such statement was verified by comparison to experimental jets with finite pressure ratios. The analysis of the pressure variation in volcanic jets starts from this principle of universality.

5.4.2 Paschen's Law

Paschens law describes the relationship between the breakdown voltage in a gas and the pressure of the gas and the separation between two charged surfaces (Paschen, 1889). Alternatively, Paschens law can be expressed in terms of the greatest sustainable electric field (Helling et al., 2013):

$$E_b = \frac{Bp}{ln(\frac{Apd}{ln(1/\gamma+1)})} \tag{5.1}$$

where p is pressure, d is the distance between two charged objects, γ is the second Townsend coefficient (10^{-2}), and B and A are constants with values of 1.14×10^4 $kPa^{-1}m^{-1}$ and 2.77×10^5 $VkPa^{-1}m^{-1}$, respectively (Stentman, 2004). On Earth at sea level (101 kPa), the potential difference required to cause an arc between a meter-wide gap (i.e. $d = 1m$) is close to 3 MV, or a field of 3 MV/m. This value decreases with pressure drop27. If the pressure is decreased to 10% of its nominal value, the maximum, the breakdown field is 0.28 MV/m, while at a pressure of 1% of nominal, the dielectric strength is only 0.035 MV/m. From the breakdown field, the maximum charge density can be computed as $Q/A_{breakdown} = E_b\epsilon_r\epsilon_o$. Thus, the maximum charge density at STP is 2.66×10^{-5} Cm^{-2}, at 10% of nominal is 2.42×10^{-6} Cm^{-2}, and at 1% is 3.14×10^{-7} Cm^{-2}. Breakdown is controlled by the number available free electrons that can be accelerated by the electric field and have sufficient energy to ionize neutral gas molecules during collisions. In a high pressure gas, the mean free path is short and free electrons collide often, but their motion becomes randomized and

they rapidly lose energy. Thus, higher voltages are required to initiate a cascade breakdown. As the pressure drops, the mean free path increases and electrons do not lose as much energy during collisions; lower voltages are required initiate breakdown. At pressures of up to 20 bar and modestly sized gaps, an almost a linear relationship between pressure and breakdown voltage exists. Beyond these pressures, Paschens classical formulation tends to overestimate the strength of the gas and corrections must be made (Cohen, 1956). Paschens law has also been shown to fail at extremely rarefied conditions. These conditions, however, do not concern the present discussion.

5.4.3 Shock tube experiments

The central piece of equipment is the shock-tube setup previously described to produce artificial volcanic lightning(Cimarelli et al., 2014). The tube was loaded with approximately 200 cm^3 of ash and then pressurized to 10 MPa with argon gas. Exceeding this pressure ruptured a set of diaphragms and the stored granular material was ejected from the tube by explosive decompression. The process produces energetic, possibly disruptive, particle-particle collisions. Such interactions are analogous to those in the gas-thrust region, causing grains to charge through a combination of tribo- and fractoelectric processes. Each decompression event was recorded with a high-speed camera at a frame rate of 36,000 fps allowing us to capture discrete spark discharges in the flow. Discharges were also characterized by a conducting ring placed a few millimeters above the vent and connected to a high-speed data acquisition unit. Similarly, the pressure at the vent was tracked throughout the experiment. For these experiments, we used ground pumice from the Laacher See maar in the Eifel Volcanic Field (State of North Rhine-Westphalia, DE) with a nominal granulometry of 90-300 microns.

5.4.4 Field observations of vent discharges at Augustine and Redoubt

Field data pertinent to the 2006 Augustine eruption and 2009 Redoubt eruption used in this work is presented in detail inThomas et al., 2007 and Behnke et al., 2013, respectively. Electrical activity at both of these volcanoes was monitored with Lightning Mapping Arrays (LMA). Atmospheric discharges produce very high frequency (VHF) radio emissions which can be studied with LMA remotely. One of the advantages of using this technique is that radio frequencies, unlike optical wavelengths, can propagate through dusty media with little hindrance. In broad terms, activity at both mountains was similar. Both volcanoes produced two distinct phases in activity: an explosive or vent phase followed by a plume phase after a small delay (although, as we have said, the distinction between the two phases was clearer at Augustine). Explosive phase radiation, quite intense and nearly continuous, was correlated to individual explosions using seismic and acoustic measurements. Due to their small scale-lengths and proximity volcanic crater, vent discharges during the explosive phase were not resolved optically. Pressure waves associated with traveling atmospheric shocks produced during individual eruptions were recorded at 3 km from Augustine vent and 12 km from Redoubts vent. Assuming simple geometric spreading, the pressure at the vent, P_v, can be estimated using a reference distance of 1 m: $P_v = P_m r_m / r_v$ (Medici, Allen, & Waite, 2014). Here, P_m is the magnitude of the pressure observed at the measurement location, r_m is the distance from the source, r_v is the reference distance. Note that these are gauge pressures. The overpressure ratio is the given as: $K = (P_v + P_o)/P_o$. Not all overpressures, however, result in sonic conditions at the vent or the formation of normal shocks. From this information, the structure of the under expanded jet can be constructed. We note that overpressure estimations presented above assume a line-of-sight between the acoustic radiator and the receiver. Because, infrasound is typically sourced from within the conduit, line-of-sight conditions are rarely possibly. Thus, acoustic waves are modified as they interact with

crater morphology and cone structure (Lacanna & Ripepe, 2013) (Yokoo, Suzuki, & Iguchi, 2014). For example, observations at Stromboli revealed topography could attenuate pressure waves by as much as an additional 11 dB at a distance of 250 m from the vent (i.e. a change in power level close to a factor of 10)(Lacanna & Ripepe, 2013). Furthermore, atmospheric conditions including wind direction and speed have been shown to influence infrasound measurements at a distance. Thus, the pressure ratios estimated here likely underestimate the true overpressures at the vent. Fig. 5.1a shows electrical data from an eruptive event at Augustine during January 27, 2006 (0524 UTC). The peak pressure associated with this event measured at a distance of 3.2 km from the vent was 83 Pa (McNutt, Tytgat, Estes, & Stihler, 2010). The reduced pressure is then 265 kPA and the overpressure factor is K = 3.65. Assuming the vent at Augustine has a diameter ranging between 20-50 m, the size of the rarefied region can be estimated from the height of the normal shock: $h = Cd_vK^0.5$. For this span of parameters the elevation of the Mach disk ranges between 30 and 80 meters. A similar procedure can be applied to Redoubt. Acoustic sensors placed 12 km from the vent captured pressure signals with maximum amplitudes of 250 Pa (McNutt et al., 2013). This implies that shocks had maximum elevations that ranged between 90 and 280 meters above the vent. At Sakurajima, blasts generated transient overpressure ratios as large as 18. Unfortunately, the conduit diameter of Sakurajimas Showa crater is poorly constrained (more so than that of the other two volcanoes in the present discussion), complicating the estimation of the shock height. Assuming a conduit diameter ranging between 30-50 m, the maximum shock elevations would have ranged between 100 and 200 meters. As mentioned in the main text, LMA data is not available for this eruption, making it impossible to comment on the presence or extent, both temporal and spatial, of vent discharges. However, Sakurajima explosions did produce near-vent lightning which was recorded with a high-speed camera. This activity, located at elevations of up to 350 above the

crater rim, occurred in both the region of rarefaction and above the shock (for the conduit diameters assumed above) (Aizawa et al., 2016) (Cimarelli et al., 2016). The existence of spark discharges several meters in length a few milliseconds after explosions suggests that efficient, broad-scale charge separation mechanisms were present in Sakurajimas jets. Such behavior stands in contrast to that observed at Augustine, where spark discharges occurred with delays of minutes after the eruption onset4. These discrepancies may be ascribed to differences in grain size distribution between volcanoes. Recall that in granular flows small particles often charge negatively, while large grains charge positively (Forward et al., 2009a) (Lacks & Levandovsky, 2007) (Lee et al., 2015). Thus, an eruption producing a highly polydisperse flow would more effectively generate large scale electric fields as large and small particles become separated gravitationally or hydrodynamically. Such may be the case for Sakurajima. Conversely, a more monodisperse flow would require more time for large and small particles to separate and produce the electric fields needed to breakdown air. This may have been the situation at Augustine.

CHAPTER 6
THE ELECTRIFICATION OF VOLCANIC PARTICLES DURING THE BRITTLE FRAGMENTATION OF THE MAGMA COLUMN

Published as: Méndez Harper, J., and J. Dufek (2015), *The Electrification of Volcanic Particles during the Brittle Fragmentation of the Magma Column*, Proc ESA Annu. Meet. Electrost. 2015.

6.1 Introduction

Volcanic plumes, like many other turbulent granular systems in nature, have the tendency to become electrostatically charged. Perhaps the most dramatic and evident consequence of this electrification are the impressive lightning displays often observed during vigorous eruptions. While volcanic lightning has been reported for millennia, the physics that generate and separate charge in plumes still require clarification. Observations of volcanic lightning storms during the 2006 Augustine eruption (Thomas et al., 2007) and the 2009 Redoubt eruption (Behnke et al., 2013) have revealed two principal discharge modalities: i) Small (1-10 m in length), chaotic discharges localized near the volcanic vent (within the gas-thrust region) and ii) larger, more organized strokes generated within the elevated regions of the plume. The production of plume lightning has been attributed to electrification mechanisms similar to those described in conventional thunderstorms, specifically processes involving the interaction of ash and hydrometeors (Arason et al., 2011). Conversely, the physics that generate the observed near-vent lightning remain more elusive. Cimarelli et al. (Cimarelli et al., 2014) have reproduced volcanic lightning experimentally by accelerating a volume of ash at high pressures using a shock tube, suggesting that volcanic material becomes electrified by triboelectric charging (Cimarelli et al., 2014) (Mendez Harper & Dufek, 2016). A second electrification method, often referred to as fracto-

emission or fragmentation charging, deals with the generation of charge during the brittle disruption of magma in the volcanic conduit (James et al., 2000). Magmatic fragmentation is initiated as a melt rises to toward the surface. As the hydrostatic pressure decreases, volatiles exsolve to form bubbles. For silica-rich magmas, which undergo extensive polymerization, the rate of bubble growth is often too fast for the melt to respond visco-elastically, resulting in the catastrophic breakup of the magma into a granular flow composed of fine, glassy particles suspended in a gas matrix. Fragmentation of the ascending magma column, and the associated charging of particles, occurs several kilometers in depth, precluding any direct observation of these processes (James et al., 1998). Electromagnetic phenomena associated with fragmentation are not unique to volcanic systems. Similar processes have been described extensively during the opening of cracks in materials such as rock, ice, metal, and polymers (Finkelstein et al., 1973). However, a cohesive theory to explain why matter becomes electrified when fragmented has yet to be formulated. For rocks, previous work has pointed to the piezoelectric properties of some minerals (e.g. quartz) which generate potentials when strained (Takeuchi & Nagahama, 2002). Studies of precursory seismo-electromagnetic phenomena have suggested that charging of deformed rocks is produced by fluids passing (streaming potential) through newly-generated or modified pore networks. Nonetheless, fracture charging has been observed in homogenous substances containing neither piezoelectric materials nor fluids. Takeuchi et al., 2004 have shown that even materials of very high purity tend to become charged, attributing this electrification to the trapping centers inherently contained in most materials.

While fragmentation charging is widely quoted in the literature as one of the principal drivers of volcanic lightning (James et al., 2000) (Thomas et al., 2007) (James et al., 2008) (Behnke et al., 2013) (Behnke & Bruning, 2015), little experimental work has been performed on the subject. Perhaps the most important, if not the

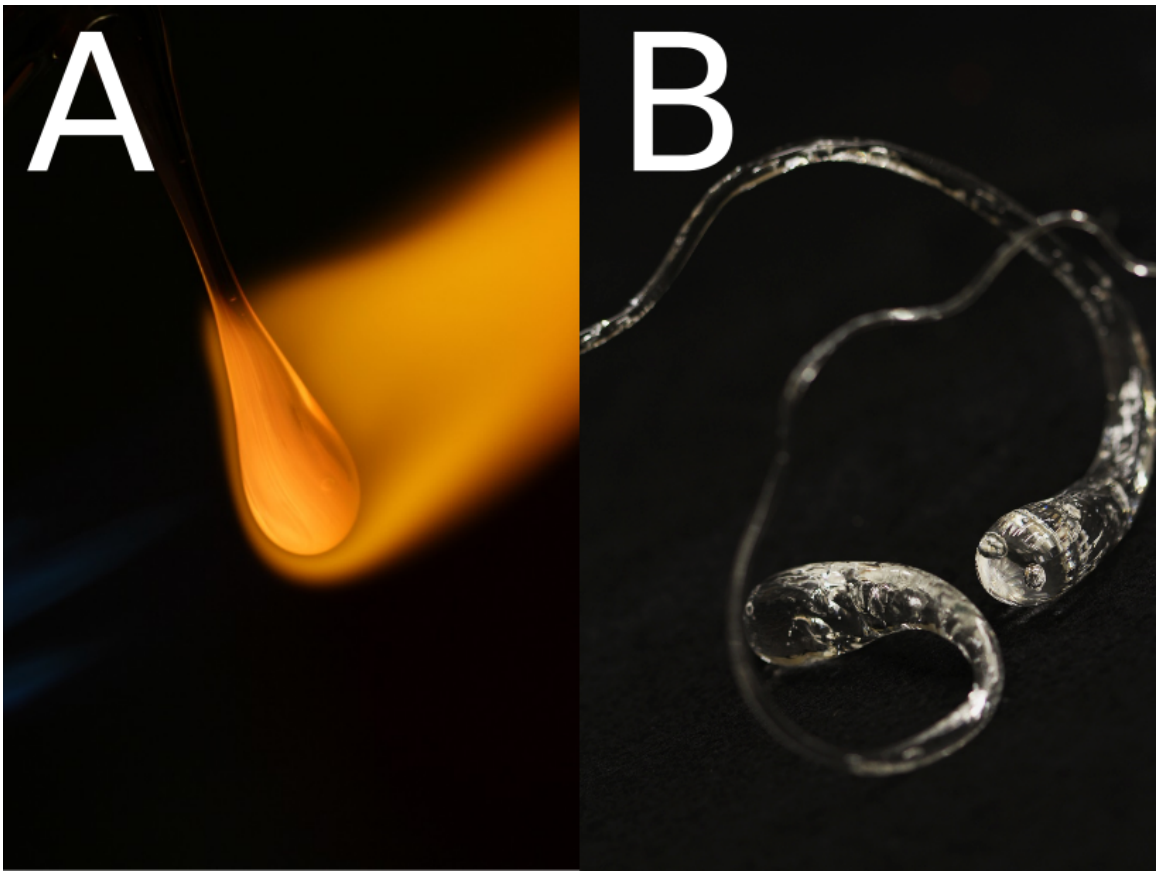

Figure 6.1: A) Prince Ruperts drop (PRD) are fabricated by pouring a droplet of molten glass into water. When the liquid glass enters the water, heat is lost at a fast rate from the glass' surface, causing the exterior to solidify rapidly. The interior, still fused, cools more slowly, but its contraction is inhibited by an already-solidified outer shell (Chandrasekar & Chaudhri, 1994) (Chaudhri, 2009). This differential cooling generates high compressive pressures in the drop's exterior, balanced delicately by tensile stresses in its core. The large compressive stresses in the outer shell make a drop "strong enough to withstand the sledgehammer." The tail, however, has a compressive layer that is much thinner. If this delicate filament is cut with a set of pliers, damage to the the inner tensile core generates the rapid growth pre-existing microcracks in the glass fueled by the release of stored elastic energy. "The whole [Prince Rupert's drop] explodes. And where, a moment before, you had unbreakable glass, now you have grains of glass in every corner of the workshop–in your eyes, if you are not careful–and what is left in your hand, you can crumble without danger" (Carey, 1989).

only, endeavor designed to quantify fracto-emission charging of volcanic material has been that of James et al., 2000. By disrupting pieces of pumice (either by impacting or by grinding two pumices together), those authors determined that particles could achieve charge-to-mass ratios close to their theoretical maxima. However, these experiments cannot distinguish triboelectric charging and fragmentation charging, two distinct processes that can generate charging in granular materials. In this work, we attempt to quantify the charging of particles driven solely by fragmentation processes. Unlike the experiments escribed in James et al., 2000, our work produces charged particles via explosive fragmentation. We show that particles acquire charges close to their saturation values and that such charging leads to the formation of aggregates. These results have important implications for the both the generation of lightning during volcanic eruptions and for understanding ash transport and residence in the atmosphere.

6.2 Methods

We developed a methodology to assess the electrification of a granular material due to fragmentation processes, while minimizing the effects of other electrification mechanisms. To produce charged particles via fragmentation, a set of 30 soda-lime Prince Ruperts drops were disrupted in a controlled environment. Prince Ruperts drops (PRD) are meta-stable, tadpole-shaped structures formed by quenching molten glass in water (Chandrasekar & Chaudhri, 1994) (Chaudhri, 2009) (see Fig. 6.1). The residual stress in the glass caused by the difference in cooling rate between the surface of a drop and its interior gives PRDs some particular characteristics. While the drops head is extremely strong (it can purportedly withstand several repeated hammer blows), the whole structure explodes violently into micron-sized particles if the delicate tail is even slightly damaged. Under linearly polarized light, the stress in the glass manifests itself as colorful fringes (birefringence, see Fig. 6.1) (Chaudhri, 2009).

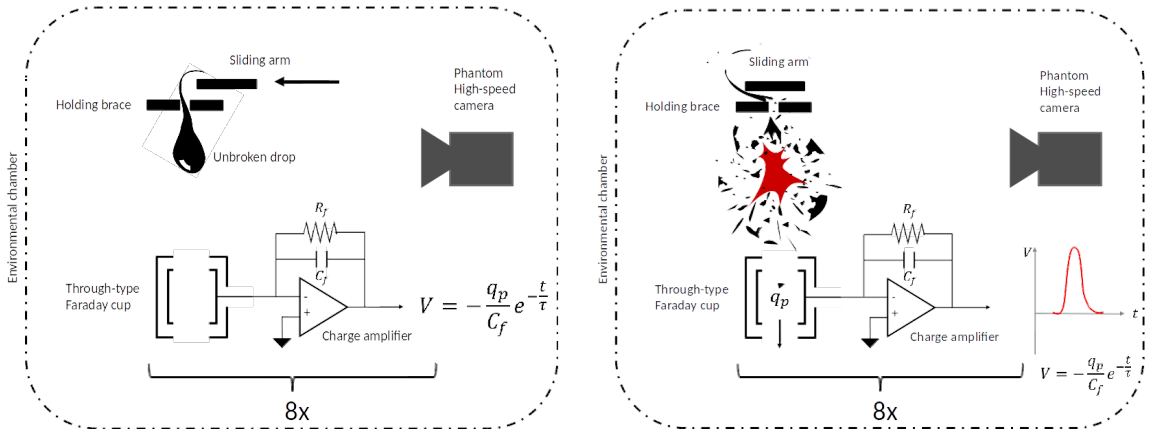

Figure 6.2: Schematic of the experimental apparatus. The Prince Rupert's drop is suspended over a set of 4 Faraday cups. An aluminum vane driven by a stepper motor is used to break the drop's delicate tail, causing explosive disintegration. The charge on particles falling into the Faraday cups is measured by a high-resolution charge amplifier.

Unlike previous experiments, in which disruption of glass (pumice) was produced by a net input of mechanical energy (by abrading or impacting the sample), the fragmentation of a PRD is driven entirely by the release of stored thermal stress. Indeed, the mechanism of PRD disruption is closer to the fragmentation of a melt during an eruption, which is also driven by stored stress in the material (stemming from the exsolution of volatiles and bubble growth) (Liu, Cashman, Rust, & Gislason, 2015).

The fragmentation apparatus is shown schematically in Fig. 6.2. At the onset of an experiment, a PRD is suspended by the tail in an aluminum holder positioned 15 cm above a set of four Faraday cups. A stepper motor is employed to spin an aluminum vane which nicks the tail of the drop. Damage to the tail causes the PRD to shatter explosively. Particles resulting from the fragmentation event are expelled in roughly all directions and a small fraction of these fall into the Faraday cups. The apparatus is housed within an environmental chamber in which we control humidity (25) and monitor temperature and pressure. A Phantom high-speed camera is used to record fragmentation events at a frame rate of 2,000 fps. The four Faraday cups were fabricated from 3/8-in square brass tubing and are mounted directly onto a

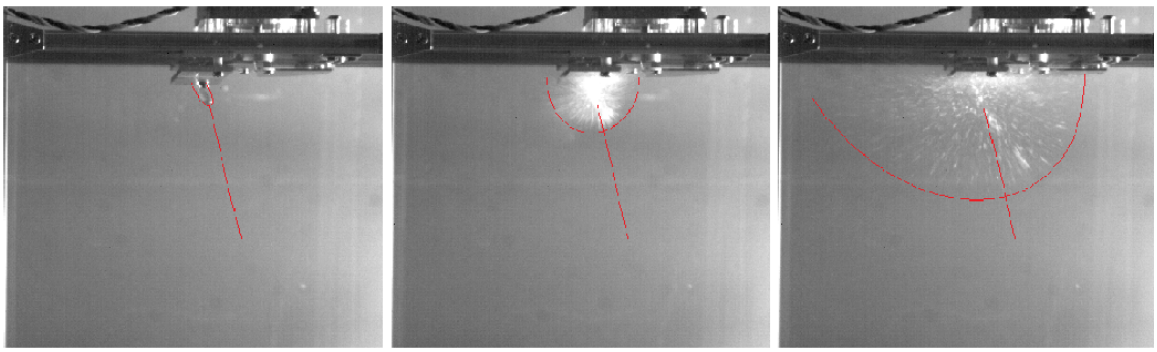

Figure 6.3: A sequence of images from a high-speed recording of the disruption of a PRD. Frames are spaced by 2ms. Red curves indicate the explosion front.

PCB which also hosts a high-resolution four-channel charge amplifier. We use an amplifier based on the design presented in Watanabe et al., 2006 with a resolution of approximately 1 fC/mV (Mendez Harper & Dufek, 2016). The charge amplifier has a time constant of 0.5 seconds. The output of the amplifier is recorded using a high-speed data acquisition card and a LabVIEW program.

6.3 Results and Discussion

Fig 6.3 displays a select number of frames from a high-speed recording of the explosive disintegration of a Prince Ruperts drop. The first frame shows an unbroken drop. In the second frame, the drop has been ruptured by the rotating vane and the cloud of particles can be seen expanding away radially in the third frame. The time between frames in Fig. 6.3 is 2 ms. The velocity of the explosion front (indicated in Fig. 6.3 by the red line) varied between runs, and was estimated to be 13-60 m/s using freely available PIV code (OpenPIV). The size distributions of the particles produced during the fragmentation of a drop were measured by taking photographs of the particles collected in the four Faraday cups and then processing them with Matlab (Fig. 6.2). Particle diameters ranged from a few microns to several millimeters, with the majority of particles having diameters smaller than 100 microns. The average particle size as determined from the photographic analysis was approximately 80-100 microns. The

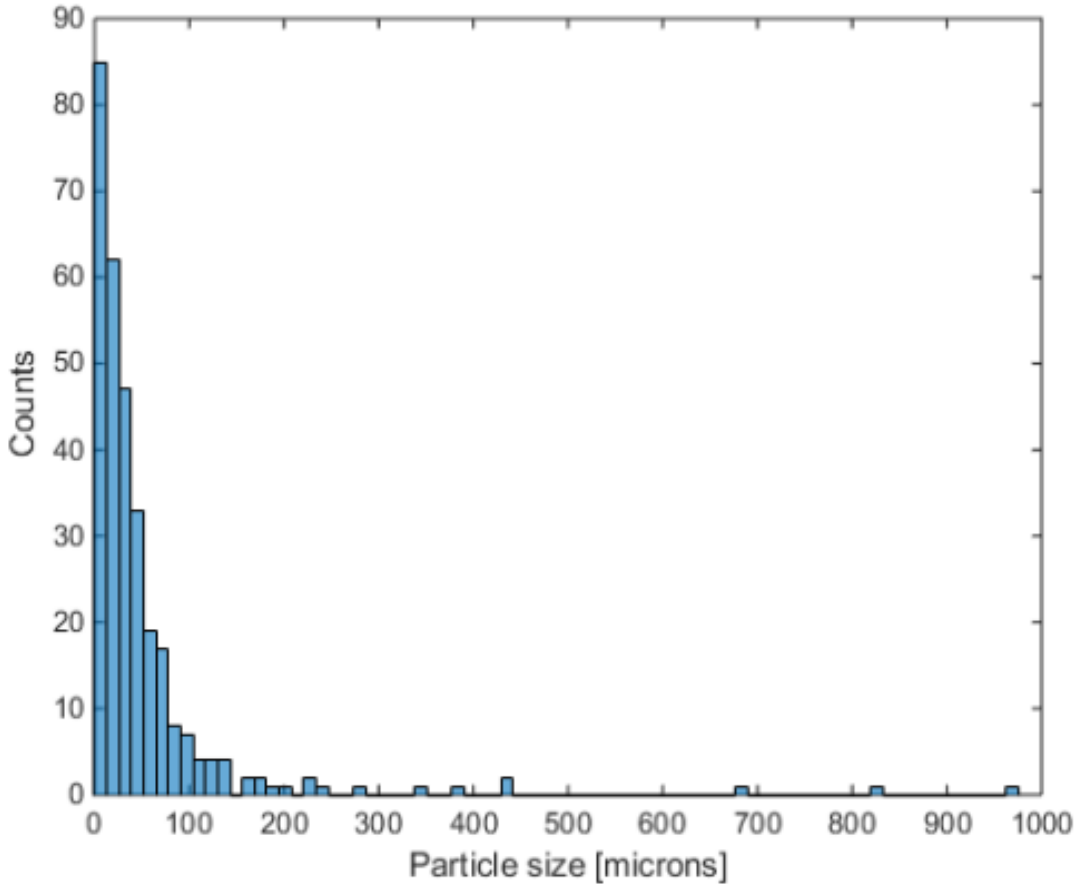

Figure 6.4: Size distribution of particles collected from the four Faraday cups at the end of an experiment.

size distribution of particles is comparable to the size distributions of natural ash described in the literature (e.g. Horwell, 2007, Houghton et al., 2013), supporting the idea that the disruption of a PRD has dynamics similar to those in real volcanic fragmentation events. The morphology of some particles from the experiments can be seen in Fig. 6.5.

Fig. 6.6 shows an example of raw data collected by the DAQ from one Farday cup during a typical run. The abrupt changes in a lines voltage indicate the passage of charged particles into the Faraday cup (arrows in Fig. 6.6). This voltage then decays back toward zero according to the time constant of the charge amplifier. Particles generated in the fragmentation event charge both positively and negatively, acquiring

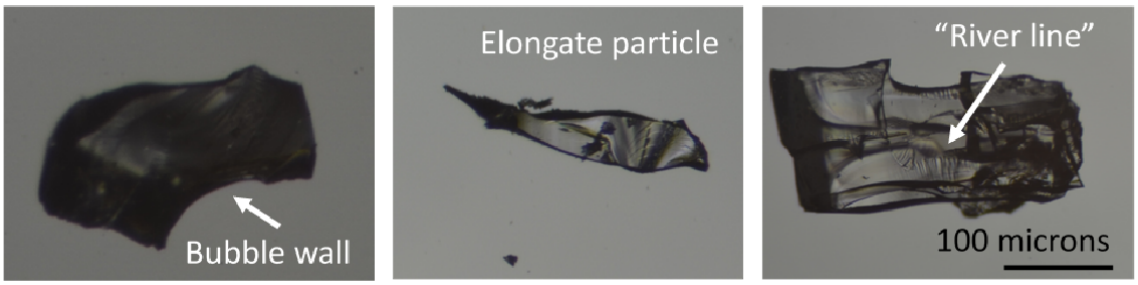

Figure 6.5: Particles from a fragmentation event displaying morphological similarities to real ash particles.

charges of up to several pico-Coulombs. Fig. 6.7 show a histogram of the specific charge for a run, computed by dividing the raw charge distribution by the average glass particle mass (assuming a density of 2600 kg m^{-3}).

For spherical particles, the maximum amount of charge that can be held their surfaces before breakdown of air occurs is given by $Q_{max} = 12\pi\epsilon_o ER^2$ (Hamamoto et al., 1992). For particles of several tens to hundreds of microns, as those produced by the disruption of a PRD, the maximum charge that can be sustained is on the order of 10^{-12} to 10^{-11} C. Alternatively, the maximum specific charge expected on such grains would lie between 10^{-4} - 10^{-3} C/kg. While most of the particles acquired *average* specific on the order of 10^{-5} - 10^{-4} during a disruption event, charge-to-mass ratios of up to 10^{-3} were observed for a few cases (See Fig. 6.7). The average specific charges obtained in our experiments are comparable to the specific charges detected on particles falling out of plumes. During an eruption of Sakurajima in 1995, for example, Miura et al., 2002 found that particles were both positively and negatively electrified, with specific charges of up to 10^{-5} C/kg (Miura et al., 2002). Gilbert et al. made similar measurement, obtaining charge-to-mass ratios ranging between -5 and 6×10^{-4} C/kg (Gilbert et al., 1991).

The previous experiments investigating fragmentation charging conducted by James et al., 2000 yielded maximum specific charges with magnitudes comparable to those in our experiments. Nonetheless, in that work, a higher proportion of particles were

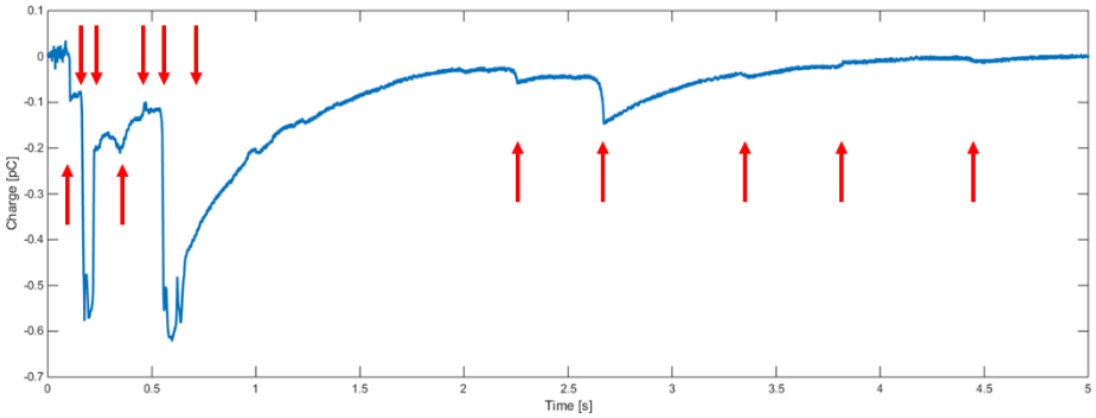

Figure 6.6: Raw data as collected from one of the Farday cups during a run. The abrupt changes in line voltage (red arrows) indicate the passage of charged particles into the Farday cup.

found to have charge-to-mass ratio greater than 10^{-3} C/kg. As mentioned above, those experiments produced charged particles by colliding or grinding two pumice samples together. The reason for these higher particle charges is likely due to the presence of additional charging mechanisms in their experiments (namely conventional frictional and contact electrification). Because both fragmentation and triboelectric processes were involved in that work, the experiments of James et al. (James et al., 2000) are more representative of the charging that occurs immediately after the main fragmentation event. Once the magma column has been ruptured, pumice pieces undergo further break-up as they transit the length of the volcanic conduit due to clast-clast collisions and collisions with the conduit wall. This comminution produces high volumes of ash and reduces the overall size of pumice clasts exiting the vent (Dufek et al., 2012). We believe that the experiments described in James et al., 2000 reflect the charging associated with post-fragmentation comminution, while our work, in which tribocharging is minimized, is more representative of charging associated with the main fragmentation event itself. Microscopic analysis of the fragmented samples revealed the presence of aggregates or agglomerates (See Fig. 6.8). In most cases, aggregates were observed to be composed of a large central particle with a number of

smaller particles clustered around it. This arrangement suggests that larger particles hold charges that are opposite in polarity to those held on smaller particles. A similar conclusion was reached by James et al., 2000, who found that aerodynamically-small particles tended to acquire charges of opposite polarity to those on larger fragments. Alternatively, charge may not be distributed uniformly on a particles surface, resulting in a patchwork of positive and negative charge which attract small particles of both polarities. Regardless of how charge is arranged, the presence of agglomerates in our experiments indicates that aggregation processes in volcanic plumes become active shortly after the material leaves the vent. Given that aggregates represent effectively larger particles, the formation of these electrostatically-bound structures has important implications for the residence time and transport of ash in the atmosphere (Telling et al., 2013).

6.4 Conclusion

In this work, we presented preliminary results on the electrostatic charging of glass particles via fragmentation processes to better understand the electrostatic processes occurring in plumes. We found that particles achieved charge-to-mass ratios similar to those detected during real eruptions. The specific charges in our experiments were slightly smaller than those observed in previous fragmentation experiments. We attribute the difference to the fact that additional charging mechanisms were operating in that work. Finally, the charges acquired by particles during the disruption of PRDs fomented the formation of aggregates.

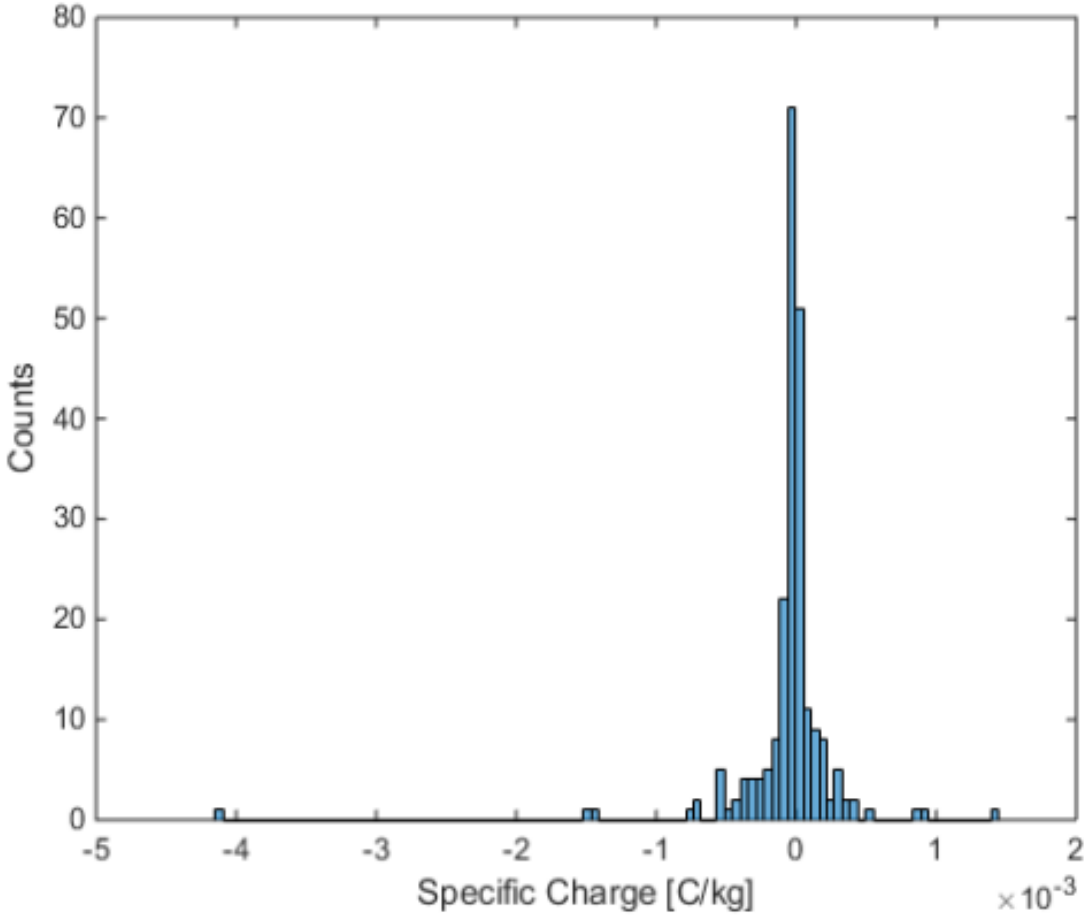

Figure 6.7: Histogram of charge-to-mass ratios computed for a typical PRD disruption.

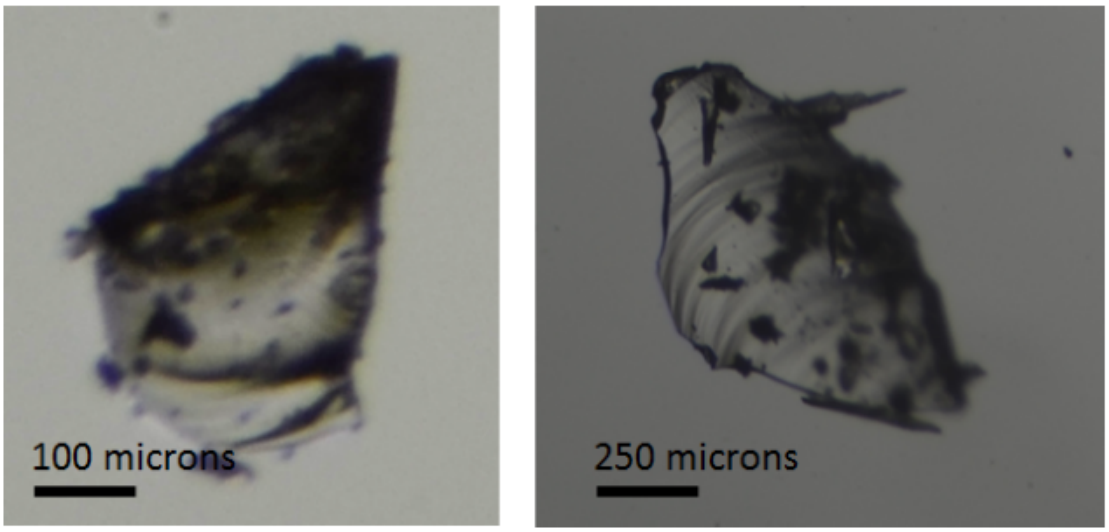

Figure 6.8: Photographs showing two aggregates formed by electrostatic forces.

CHAPTER 7

GRANULAR RESERVOIRS ON OTHER WORLDS

7.1 Titan

7.1.1 Introduction

Cassini-Huygens revealed Titan to be a geomorphologically active moon, replete with dune fields, liquid at the surface, and sedimentation from the atmosphere. The active surface processes produce many landforms reminiscent of those on Earth, albeit driven by hydrocarbons instead of water. However, the chemistry and physical properties of hydrocarbons may give rise to many important and unexplored differences compared to processes on Earth, where water phases and silicate weathering and transport shape the surface. One process that has only minor geomorphic impact on Earth, but which preliminary calculations and experiments have shown to be important is the electrical charging of hydrocarbon particles (Lorenz et al., 2006) (Mendez Harper, McDonald, et al., 2017).

7.1.2 The Titan Atmosphere-Surface Hydrocarbon Cycle

Likely sources of organic molecules on the surface of Titan result from materials produced by photochemical processes in Titans upper atmosphere. High in the atmosphere of Titan, solar radiation and energetic particles initiate complex photochemical cascades that ultimately generate larger organic molecules and complex organic products (Waite et al., 2007) (Lavvas, Coustenis, & Vardavas, 2008) (Krasnopolsky, 2009) (Krasnopolsky, 2014) as shown in Fig. 2. Many of these products incorporate nitrogen into their structures (Imanaka & Smith, 2010). The primary materials that are generated include ethane (C_2H_6), propane (C_3H_8), acetylene (C_2H_2), and hydrogen cyanide (HCN). Higher order nitriles such as acetonitrile, acrylonitrile, and

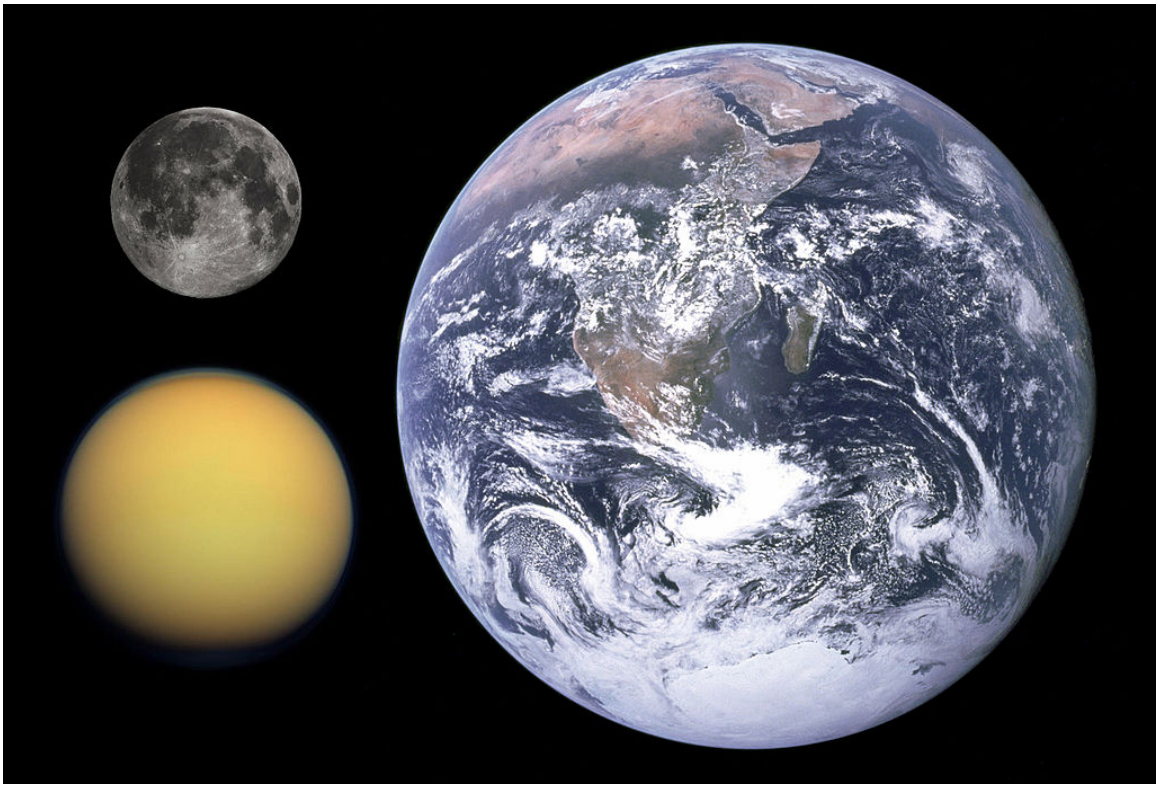

Figure 7.1: Titan compared to Earth and the moon. NASA.

cyanoacetylene are also produced. Many of these molecules are condensable and eventually deposit on the surface of Titan. In addition to discrete molecules produced in the atmosphere, more complex materials may form the haze particles composing the atmospheric haze layers surrounding Titan. Laboratory experiments on Earth have energized gas mixtures of nitrogen and methane that simulate the atmosphere of Titan and other planets under a variety of conditions to produce complex organic molecules known as tholins (Cable et al., 2011). Tholins are laboratory materials though to be analogs of complex materials produced in Titans atmosphere and on other planetary bodies. The bulk elemental composition of laboratory tholin depends on the exact experimental conditions used for their formation (Imanaka & Smith, 2010). Many of these molecules are likely derivatives of a complex atmospheric chemical manifold using HCN as one of the feedstock (He & Smith, 2013).

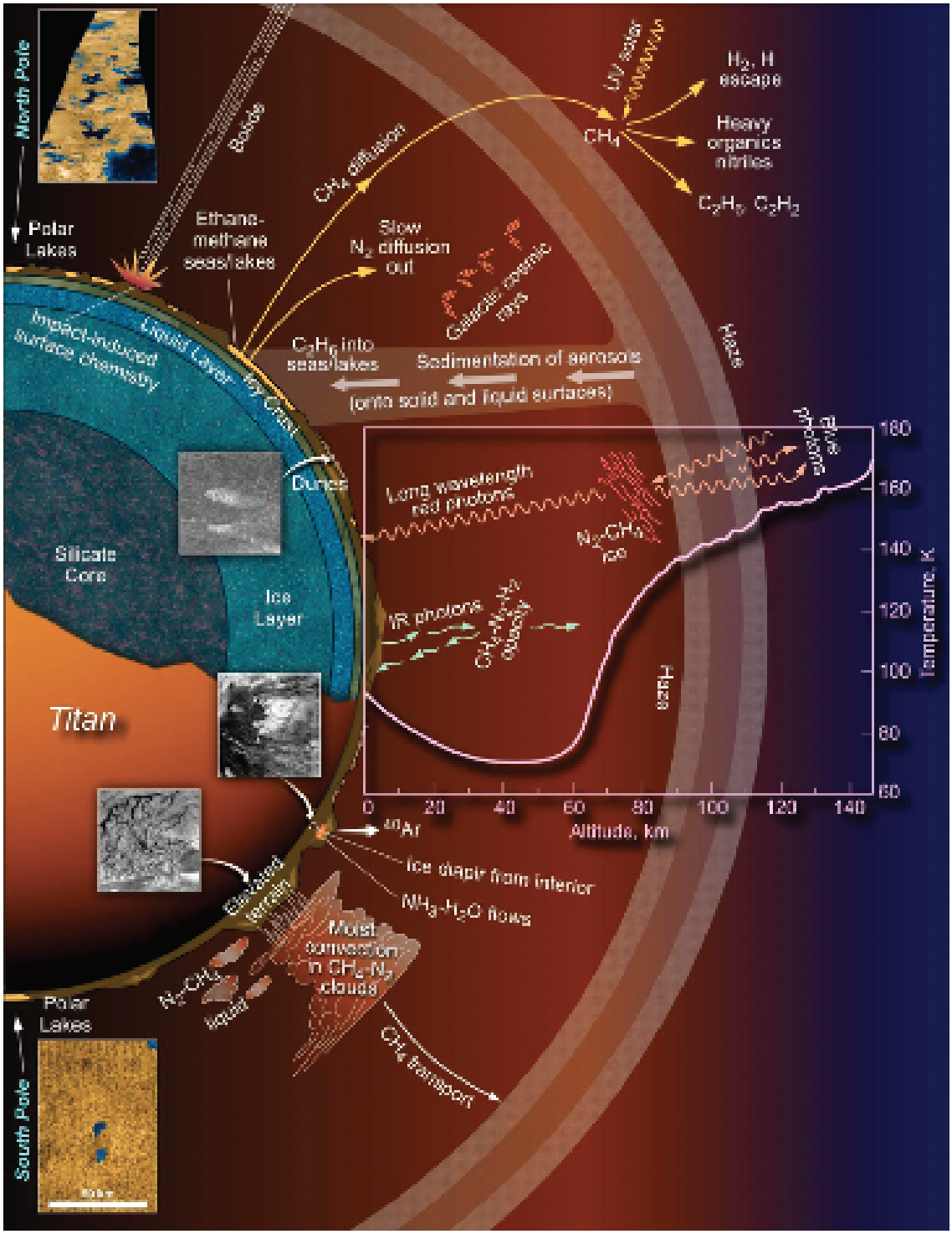

Figure 7.2: Hydrocarbon cycle on Titan (JPL/NASA)

7.1.3 Geomorphology and radar observations

The most dominant unit by surface area on Titan is the mid-latitude plains, in particular the terrain unit referred to as the undifferentiated plains (Lopes et al., 2010). The second largest unit involves the longitudinal dunes, which make up the vast sand seas in the equatorial zone (Lorenz et al., 2006). Previous work has identified dunes and plains as significant repositories of organic materials (Lorenz & Radebaugh, 2009) (Lorenz, 2014). The linear dunes terrain unit is composed of parallel to subparallel radar-dark lines (Figure 7.3). The dark terrains can be seen to onlap or invade neighboring terrain units on the downwind contact. Defects are often observed in the dark lanes as they branch or join together, clear bifurcations and Y-junctions are present. Tapering relationships can be seen with hummocky obstacles, indicating westerly transport direction (Lorenz et al., 2006) (Radebaugh et al., 2008) (Lorenz & Radebaugh, 2009) Rodriguez et al., 2014. Microwave measurements show that the dune areas have a high emissivity. Williams, Radebaugh, Lopes, and Stofan, 2011 interpreted them as longitudinal dunes composed of fine-grained fragmental material deposited by aeolian processes. ISS images of these areas are dark at 0.93 microns and correspond to the VIMS dark brown unit (Soderblom et al., 2007) (Rodriguez et al., 2014). The linear dunes units are found in the equatorial regions and do not extend above 30 degrees latitude. Both microwave emissivity and infrared characteristics are consistent with linear dunes composed of organic materials. A peculiarity in the morphologic expression of these dunes is that they appear to be formed from eastward sediment transport (Lorenz et al., 2006) (Radebaugh et al., 2008), in contrast with the dominant westward wind flow in the equatorial region (as inferred by General Circulation Models) (Tokano, 2010) (Lora, Lunine, & Russell, 2015) (McDonald et al., 2016). Work involving climate modeling, the scaling of terrestrial sediment transport equations, and wind tunnel experiments has shown that high saltation thresholds (with respect to Titans m/s wind speeds) may exist on Titan (Burr et al., 2015).

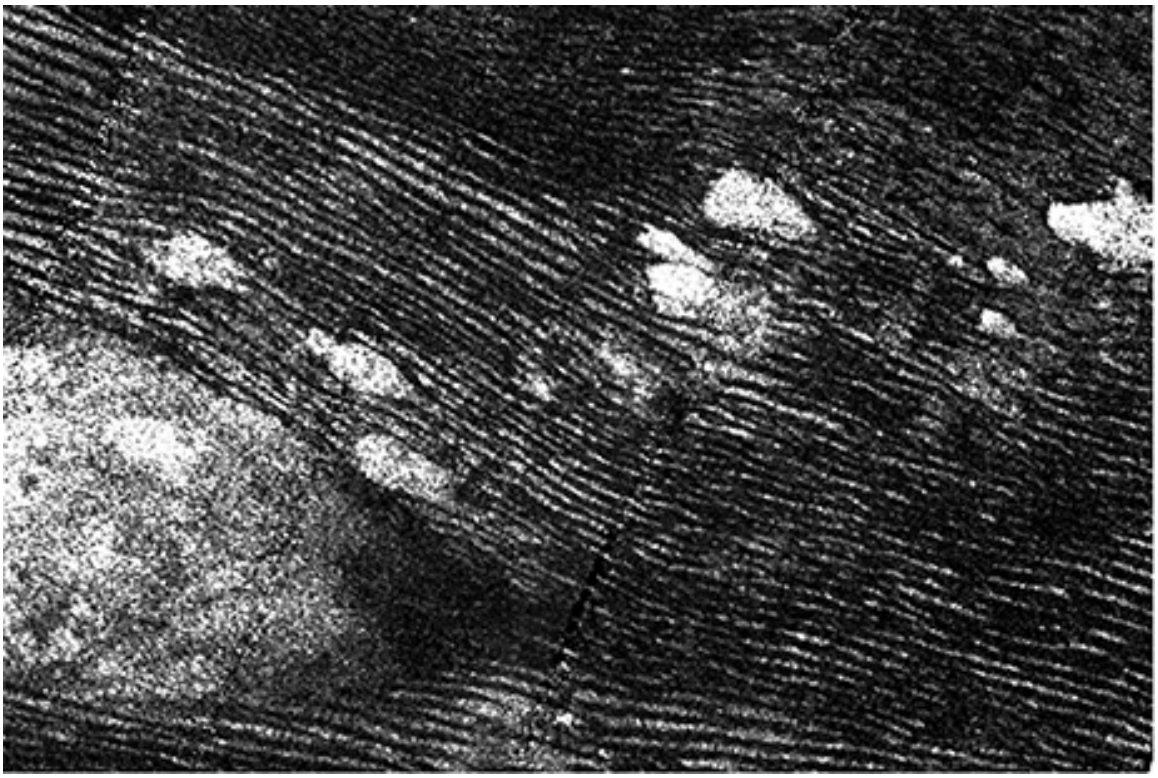

Figure 7.3: Hydrocarbon linear dunes on Titan (NASA)

This conclusion suggests that the dunes are insensitive to slow easterly winds, and respond exclusively to rare, faster or storm winds, proposed to be westerly in nature (Tokano, 2010) (Lora et al., 2015). (Burr et al., 2015) indicate the importance of low particle to fluid density ratio on Titan. An additional parameter affecting saltation on Titan, which has received little attention to date, is that of particle cohesion as a result of interparticle forces. While empirical expressions for the saltation thresholds have included interparticle forces such as van der Waals and electrical double layer forces (Iversen & White, 1982) (Shao & Lu, 2000), only recently have electrostatic forces been shown to have the ability to importantly influence the mobility of sediment in a Titan context, potentially modifying large scale geomophology.

7.1.4 Tribocharging on Titan

During the transport of granular materials, collisions between constituent particles result in electrification. This process, called triboelectric charging, can occur in systems of chemically heterogeneous particles, but is even observed in systems where particles are of the same composition (Lacks & Sankaran, 2011). Triboelectric charging has been described in silicate particles, plastics, agricultural flows, and industrial powders (Matsusaka et al., 2000). In Earths silicate systems, electrostatic forces do not affect the dynamics of most granular flows because the grains are heavy and the charges that can be acquired are quite small Telling and Dufek, 2012 (Telling et al., 2013). Thus, electrostatic forces between grains in silicate systems act over short distances and are usually weak compared to inertial forces. Yet, frictional charging is heavily influenced by particle chemistry, particle morphology, and environmental conditions (Lacks & Sankaran, 2011). On planetary bodies with distinctly unique surface materials and atmospheres sediments may experience radically different charging behaviors than those encountered on Earth. One such place may be Saturns largest moon Titan. Entrenched under Titans haze vast granular reservoirscomposed polyaromatic hydrocarbon grains rather than silicatesblanket the surface in the form of linear dunes and plains. Recent experimental work conducted by our group has demonstrated that these exotic sediments not only charge differently than terrestrial materials when mobilized under aeolian forcing, but that their dynamics are particularly susceptible to electrostatic forces. Triboelectric charging is important on Titan for three main reasons: 1. Hydrocarbon grains are more efficient at retaining charge than silicate grains, 2. Titans atmospheric conditions, including pressure and dry, cold conditions, enable a larger maximum charge on the particles, and 3. The low relative density of hydrocarbon particles permits larger charge-to-mass ratios for these particles. As a result, the dynamics of particles at the surface may be significantly altered as these aggregate into larger particles, thereby increasing the force required

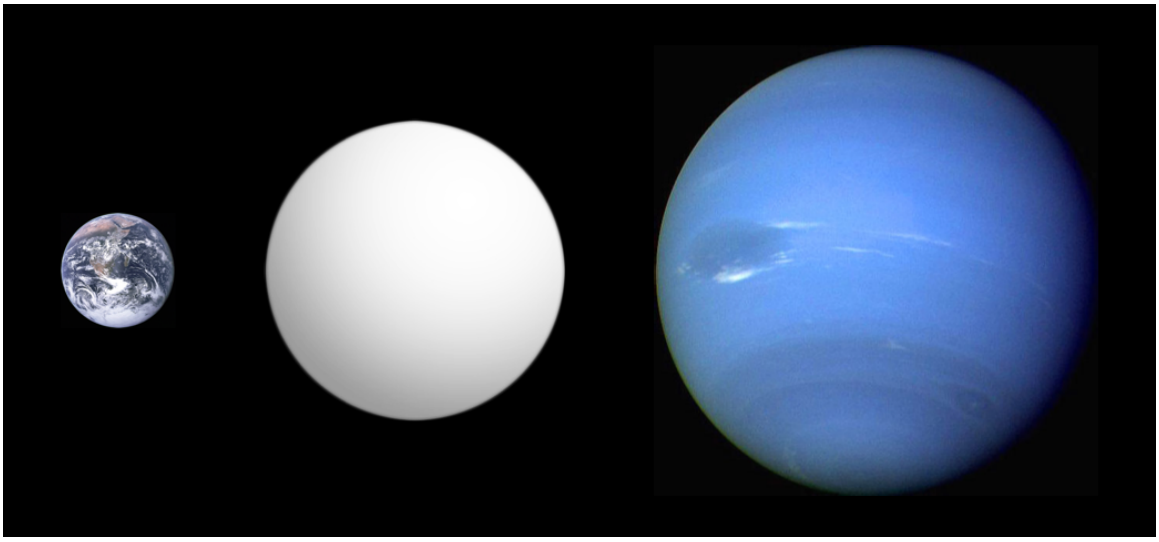

Figure 7.4: Artist's redition of GJ1214b with Earth and Neptune for scale. CC license, Aldaron

to initiate motion of grains (Mendez Harper, Cimarelli, et al., 2017).

7.2 Gliese 1214 b

7.2.1 Introduction

Gliese 1214 b (also GJ1214b) is an exoplanet orbiting Gliese 1214, an M-dwarf star 42 light-years from the Sun, in the constellation Ophiuchus (Charbonneau et al., 2009). Larger than Earth, but smaller than the solar system's gas giants, GJ1214b constitutes a super-Earth. The planet was discovered in 2009 under the auspices of the MEarth Project when dimming (1.5 %) of GJ1214's luminosity was observed every 1.58 days (Charbonneau et al., 2009). Althought, GJ1214b has an inferred radius of 2.7 Earth radii, its density is substantially smaller than that of Earth (1870 kg m^{-3}).

GJ1214b is believed to be a "water world"–i.e. a planet with a hydrogen- or water-rich atmosphere. However, studies with the Hubble Space Telescope have revealed that GJ1214b has a featureless transit spectrum suggesting the presence of thick clouds or hazes at elevations consistent with 0.1 -0.01 mbar depending on atmospheric

metallicity (Kreidberg et al., 2014) (Charnay, Meadows, Misra, Leconte, & Arney, 2015). Hazes may be similar to those found on Titan but a mechanism for their formation has not been explored. Clouds in GJ1214b's atmosphere may be exotic condensates such as potasium chloride (KCl) or zinc sulfide (ZnS) that form deeper in the atmosphere and are then carried to elevation by string atmospheric circulation (Kempton, Zahnle, & Fortney, 2011).

7.2.2 Electrification in the atmosphere of a super-Earth?

Dynamic atmospheres with clouds commonly display lightning. In the atmospheres of the Solar System's gas giants discharges occur in vertically extensive convective clouds. On Venus, cloud to ground lightning is unlikely due to the high atmospheric pressure, but may occur at elevation as intra-cloud lightning. On Earth, discharges occur in many environments, from volcanic plumes to severe weather systems, and are driven by a wide range of electrification mechanisms. Similar diversity likely exists on explanets.

CHAPTER 8

THE ELECTRIC SANDS OF TITAN

Published as: Méndez Harper, J., G. D. McDonald, J. Dufek, M. J. Malaska, D. M. Burr, A. G. Hayes, J. McAdams, and J. Wray (2017a), *Electrification of sand on Titan and its influence on sediment transport*, Nat. Geosci.

8.1 Introduction

Fluidized granular materials readily become electrified as grains rub against and collide with each other(Lowell & Truscott, 1986a)(Lowell & Truscott, 1986b). In some settings, such contact and frictional electrificationcollectively termed triboelectrificationmay generate electrostatic forces between grains that are comparable to gravitational or drag forces, affecting the overall dynamics of the granular system(Matsusaka et al., 2010). These charging effects have been problematic in processes involving low-density pharmaceutical powders, which readily stick to the interior of pipes or agglomerate during transport (Lacks & Sankaran, 2011) (Thomas et al., 2009) (Hendrickson, 2006). Similar processes are sometimes observed in natural contexts(James, Gilbert, & Lane, 2002) (Telling et al., 2013). However, the dynamics of silicate flows on Earth, like volcanic jets and sandstorms, present a degree of immunity to electrostatic forcing because inertia, a function of high gravity and particle density, tends to dominate particle-particle interactions except for very dilute and low-energy systems (small grains and small interaction velocities)(Kok & Renno, 2008) (Telling & Dufek, 2012)(Telling et al., 2013) (Lee et al., 2015). Elsewhere in the solar system, however, reservoirs of non-silicate granular materials under lower gravity may allow for complex electrostatic interactions not commonly observed on Earth. One planetary body with low gravity and vast reservoirs of low density, non-silicate granular materials is Saturns moon Titan (Le Gall et al., 2011) (Lorenz et al., 2006) (Radebaugh et al.,

2008) (Rodriguez et al., 2014). There, linear dunes make up the sediment seas that blanket extensive portions of Titans equatorial provinces, while sprawling undifferentiated plains may be sinks for material carried downstream by wind action (Lopes et al., 2016) (Malaska, Lopes, Hayes, et al., 2016). Unlike the sand reservoirs on Earth and Mars, Titan's dunes have been inferred to consist of low-density organic sands based on their near-infrared spectra and microwave emissivities (Le Gall et al., 2011) (Soderblom et al., 2007) (Barnes et al., 2008) (Malaska, Lopes, Williams, et al., 2016). Titan's vastly different physical environment requires that much of the intuition developed from studies of granular dynamics in the terrestrial context be re-examined or used with care when applied to processes on the Saturnian moon. Specifically, granular electrification may be enhanced on Titan relative to terrestrial conditions for multiple reasons. Firstly, Titans high-pressure surface environment is characterized by an ionization limit 1.5 times higher than that of Earths (Raizer, 2011) (Paschen, 1889) (via Paschens Law), enabling surfaces to achieve greater charge densities before charge is lost to the atmosphere (Lorenz, 2014) (Manning et al., 2010) (Helling et al., 2013). Additionally, the high resistivity of many hydrocarbon materials ($> 14\Omega m$)(Keithley, 2004) and the dry, cold conditions of the atmosphere (95 K and the absence of water vapour at the surface) may allow grains to retain charge for long periods (days to months) (Galembeck et al., 2014) (Greason, 2000). Furthermore, evidence from the Huygens probe suggests an environment of very low conductivity near the surface, resulting in slow charge leakage (Hamelin et al., 2016). Perhaps most importantly, the relatively low density of hydrocarbon grains ($1000 kgm^{-3}$) likely results in electrified particles with larger charge-to-mass ratios, meaning their dynamics respond more favourably to electrostatic forces than heavy silicate grains (Telling & Dufek, 2012) (Telling et al., 2013) (Lee et al., 2015). Quantifying the effectiveness of tribocharging under Titan conditions may contribute to understanding kilometre-scale landforms and aeolian dynamics. A significant question in Titan science involves reconciling the

Table 8.1: Experimental conditions for Titan and Earth cases.

Parameter	**Titan**	**Earth**
Atmosphere	N_2	Air
Pressure	0.145 MPa	0.1 MPa
Humidity	<1%	30-40%
Temperature	300 K	300 K

streamlining of the dunes which suggests westerly sediment transport (Lorenz et al., 2006) (Radebaugh et al., 2008) (Malaska, Lopes, Williams, et al., 2016) (Lorenz & Radebaugh, 2009) with the dominant easterly wind flow at the equator (as inferred by general circulation models (Lora et al., 2015) (Tokano, 2010)). Some considered scenarios for explaining the mismatch invoke high saltation thresholds, implying that sediment transport is controlled by equinoctial storms and/or rare fast westerly winds and not the milder easterly winds (Tokano, 2010) (Lucas et al., 2014) (McDonald et al., 2016) (Charnay, Barth, et al., 2015). If efficient triboelectric processes exists on Titan, large saltation thresholds could be generated via large electrostatic forces. Indeed, strong interparticle forces could influence aeolian processes ranging from entrainment at the grain scale to dune morphology and orientation at the landscape scale (Burr et al., 2015) (Rubin & Hesp, 2009). We note that changes to saltation behaviour resulting from electrostatic forces would be complementary to the effects of the small difference in density between the atmosphere and particles, which has been shown to result in high saltation thresholds(Burr et al., 2015) compared to those predicted by empirical relationships calibrated with terrestrial data(Shao & Lu, 2000) (Iversen & White, 1982).

8.2 Methods

Here, we describe a set of laboratory-scale experiments designed to explore frictional electrification under Titan-like surface conditions and compare these to similar experiments using terrestrial conditions. To recreate granular flows on Titan, we used two organic materials inferred to exist on the surface, naphthalene ($C_{10}H_8$) and biphenyl ($C_{12}H_{10}$), as well polystyrene as an analogue. Naphthalene is the simplest fused polycyclic aromatic hydrocarbon and can be used as an end-member proxy for that entire class of molecules. Naphthalene has been identified in Titans atmosphere from CAPS data byWaite et al., 2007. Delitsky and McKay, 2010 also suggest that polyphenyls are likely to be present in the Titan system. The simplest polyphenyl molecule is biphenyl. Polystyrene, an aromatic compound, serves as a good analogue material with similar physical properties. For terrestrial flows, we employed plagioclase sand, andesitic volcanic ash (Popocatépetl, PUE, México), and basaltic/felsic material from a phreatic base surge (Atéxcac axalapazco, PUE, México). All materials were sieved to obtain size distributions between 300-1000 microns (a note on why this grain size was selected is given below; See Fig. 8.5).

Grains were charged with an open-ended tumbler that simulates a dense granular flow over a substrate of identical chemical composition. Specifically, the interior wall of the tumbler was coated with material of the same composition as that under test (Fig. 8.1; see Methods). Experiments with organic grains were carried out under approximated Titan atmospheric conditions consisting of a nitrogen gas environment with ¡1 relative humidity and a pressure of 0.145 MPa. These studies were conducted at 300 K as opposed to the 95 K surface temperatures of Titan. Previous work (Greason, 2000) has shown that the efficiency of triboelectric charging can increase by as much as 50 % with a 15 K drop in temperature. Thus, experiments conducted at room temperature likely yield conservative estimates of the electrification under colder

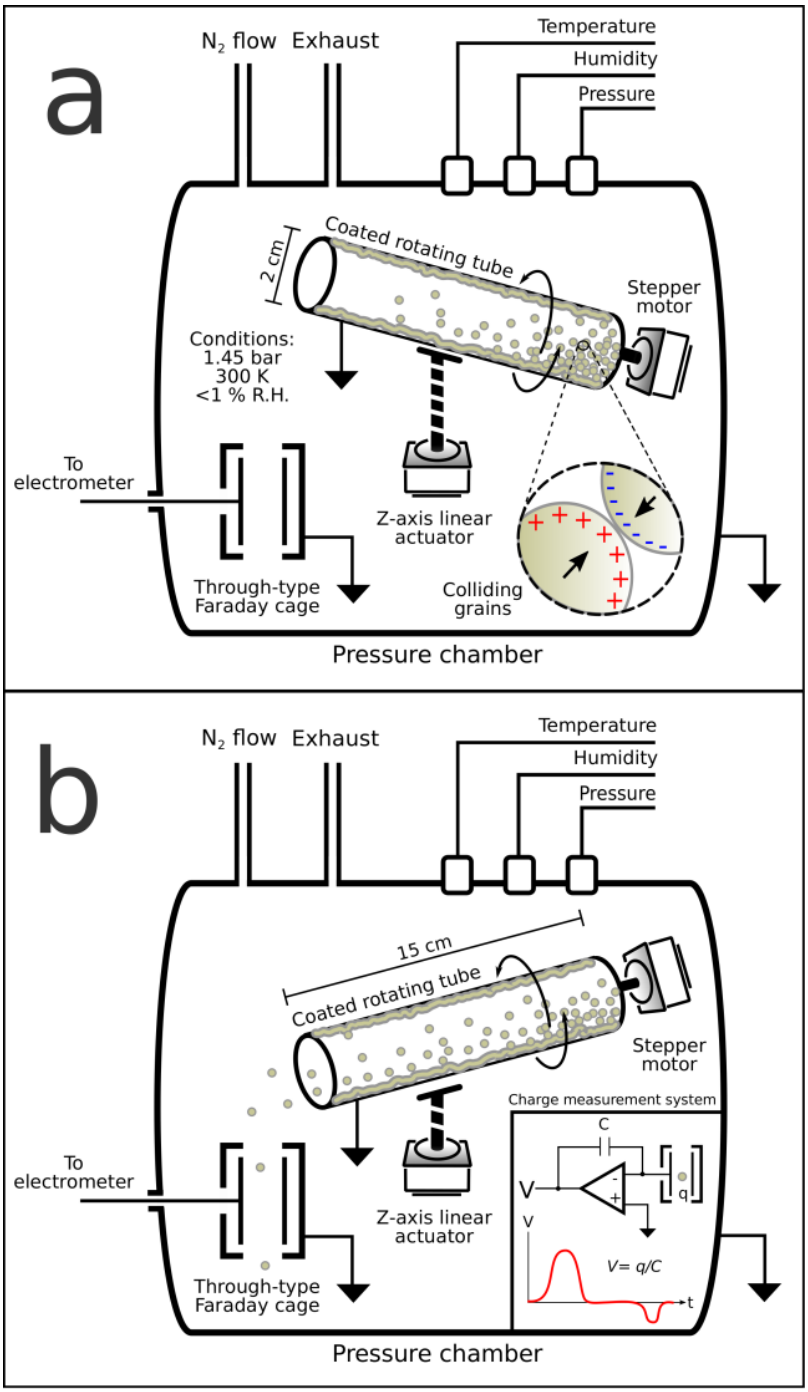

Figure 8.1: Experimental apparatus. Panel A shows the operation during the charging period, while panel B shows the system during the measurement period.

Titan conditions. The terrestrial simulations were run in air at room temperature with 30 % RH and a pressure of 0.1 MPa. Tribolectrification of the granular materials was achieved by driving the tumbler with a stepper motor at constant angular velocities. The rotation rates were selected to produce flows with linear velocities matching the inferred minimum threshold friction speeds for Titan (Burr et al., 2015) and for Earth (Shao & Lu, 2000) (see Methods). Each material was charged for 20 minutes, a period sufficiently long for individual grains to reach charge equilibrium (Mendez Harper & Dufek, 2016)

8.3 Results

After charging, the tumblers open end was inclined downward, allowing grains to roll out and fall into a miniature through-type Faraday cage. This measurement system can characterize the charge on individual sub-millimetre-sized particles with a resolution of 10 fC. While the sensor is able to resolve particles as small as 100 microns, we employed grains with diameters, d , of 300-1000 microns to ensure a good signal-to-noise ratio. Particles acquired charges up to several picocoulombs. Instead of raw charge, however, a more common metric used to assess the amount of electrification in a granular material is the surface charge density or the charge of particles normalized by their surface area, A. As described elsewhere (Mendez Harper & Dufek, 2016), absolute charge density distributions can be obtained by calculating the joint relative frequency of the particle size distributions (assuming spherical particles) and the charge distributions. Charge density distributions for organics and silicates are plotted in Fig. 8.2a and Fig. 8.2b, respectively. Although both classes of materials have distributions that peak near $10^{-7} Cm^{-2}$, the maximum charge densities recorded in the experiments with organics were generally one order of magnitude larger than that for silicates with similar size distributions. We attribute the higher charge densities on organic grains to their elevated resistivities and the

dry atmosphere in which they charged. Electrification in a material can also be evaluated using the specific charge or charge-to-mass ratio (Fig. 8.2c and Fig. 8.2d), computed by dividing the charge on a particle by its mass. Whereas the surface charge density reveals how much charge has been deposited on a surface during a particular mobilization process, the specific charge provides insight into how a charged granular substance responds to external forcing because it also includes information about the material's density. Systems with small specific charges (small Q/m ratio) tend to be dominated by inertia, whereas particles with large Q/m ratios tend to react readily to imposed electric fields. Organic particles with densities near $1000 kgm^{-3}$ easily attain specific charges exceeding $10^{-4} Ckg^{-3}$. Conversely, sand and volcanic ash (with densities ranging between 2400 and $2600 kgm^{-3}$) have maximum Q/m ratios on the order $10^{-5} Ckg^{-3}$ (note that similar charge-to-mass ratio values have been measured on wind-blown sand grains in natural environments). The elevated charge-to-mass ratios indicate that Titan materials, once charged, may be more responsive to electrostatic forces, which can emanate either from the granular flow itself or from an external source, than would the denser silicate grains. We note that previous studies have reported a correlation between the amount of charge collected by a granular material and the kinetic energy of the granular flow (Matsusaka et al., 2010) (Lacks & Sankaran, 2011). Because we excited organic particles at the minimum frictional speed, the charge densities and charge-to-mass ratios reported represent the minimum degree of electrification expected on Titan.

8.4 Discussion

8.4.1 A comparison between electrostatic and inertial forces

We obtained direct evidence for electrostatically-driven processes in the experiments with organic materials; a small fraction of particles (2 to 5 of the total sample) remained adhered onto the wall of the tube due to electrostatic forces and did not fall

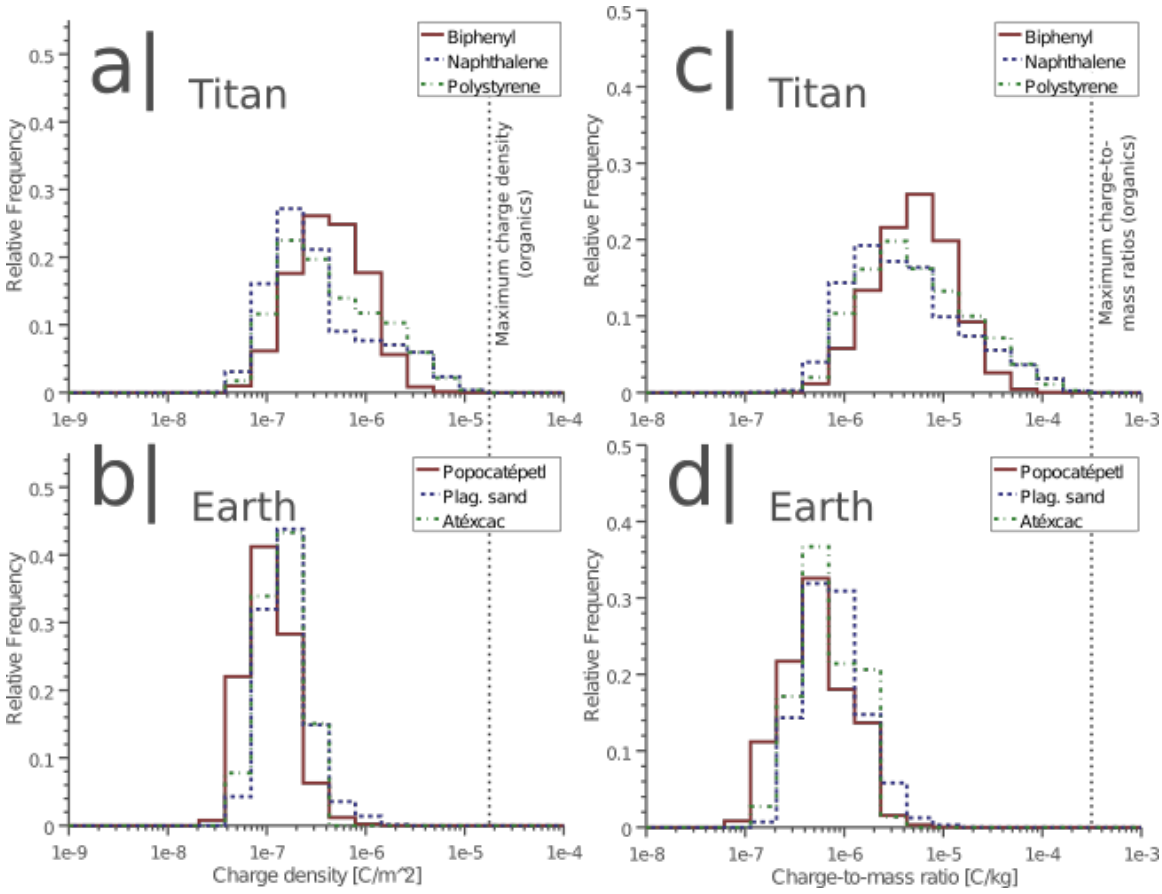

Figure 8.2: Surface charge densities and charge-to-mass ratios A) Charge density distributions for three organic, granular compounds (biphenyl, naphthalene, and polystyrene). B) Charge densities for three silicate samples. C) Charge-to-mass ratio distributions for the same three organic, granular compounds. D) Charge-to-mass ratios for three silicate samples. Note that both the charge densities and charge-to-mass ratios in experiments with organics have maximum magnitudes one order of magnitude higher than those recorded in the experiments with silicates.

out when the tumbler was inclined. This phenomenon occurred in all experiments with materials inferred to exist on Titan. The "aggregates" were typically composed of single immobilized grains on the inner substrate of the tumbler, but both the experiments with polystyrene and biphenyl revealed a number of multi-particle aggregates (Fig. 8.3a). These last structures had diameters exceeding several millimetres. Particles that remained in the tumbler were presumably electrified to a higher degree than those that fell out. Because we only characterized grains that were removed from the apparatus, the distributions depicted in Fig. 8.2 may underestimate the full range of charge densities and Q/m ratios in the organic samples. Such aggregate formation did not occur in experiments with silicate materials. Whether or not two grains will be affected by electrostatic forces upon contact can be determined by evaluating their electrostatic-inertial ratio (EIR) or the ratio of the electrostatic energy, U_E, to the inertial energy U_I, (Telling & Dufek, 2012) (Telling et al., 2013) (Lee et al., 2015)

$$EIR = |U_E|/U_I \tag{8.1}$$

A pair of particles with an EIR smaller than 1 is dominated by inertia. Conversely, a pair of particles with an EIR larger than one is influenced predominantly by electrostatic forces. The collisional kinetic energy in equation 8.1 is computed as $0.5 m_r v^2$, using the reduced mass of the system and the collisional speed. For organic and silicate grains, we set these speeds to the inferred minimum saltation threshold speeds for Earth (0.2 m/s) and Titan (0.06 m/s), respectively (i.e. the linear speeds at which the tumbler was driven). The electrostatic energy between two grains with charges Q_1 and Q_2 is described by $U_e = k_C \frac{Q_1 Q_2}{h} - f(k, r, h)$, where h is the separation between the grains geometrical centres, and k_C is Coulomb's constant (Bichoutskaia, Boatwright, Khachatourian, & Stace, 2010). The second term, $f(k, r, h)$, represents stored energy due to mutual polarisation and is a function of the particles dielectric constants, k_i , their radii r_i, and h. Polarisation effects are important when charged

particles are close together and we calculate this term using a multipole approach based on a spherical coordinate system (see Methods, equation 8.4) (Bichoutskaia et al., 2010). The electrostatic energy is computed for two mechanically identical grains ($r_1 = r_2 = D_p/2$) with the same net charge magnitude ($|Q_1| = |Q_2| = \pi D_p^2 |\sigma|$) that are touching ($h = D_p$ i.e., at the moment of contact). The charge densities used in this calculation were obtained by averaging the charge densities from a given class of materials (either silicates or organics). For two mechanically equivalent particles in contact, the EIR is independent of particle size because both the electrostatic and kinetic energies depend on (See methods). Organic particles were able to attain electrostatic energies comparable to or exceeding their kinetic energies. As revealed in Fig. 8.3b, 11 % of reported charge densities on organic particles result in EIRs larger than one, while 36 % had EIRs exceeding 0.1 (i.e. these particles had electrostatic energies larger than 10 of their kinetic energies). The maximum EIR reported for organic materials was 90. Contrastingly, all silicate grains had EIR smaller than one with a maximum EIR close to 0.05.

8.4.2 The effect of charging on the saltation threshold

The efficient triboelectric charging of organic grains may have important implications for the mobilization of sediment on Titan. In previous wind tunnel simulations, where friction wind speeds were shown to be higher than expected due to the low density ratio between the atmosphere and the solids, it was noted that higher-than-terrestrial interparticle forces would exacerbate the mismatch between modelled and actual threshold wind speeds on Titan35. The elevated charge-to-mass ratios attained by Titan analogue materials indicates that those experimental results may have indeed underestimated Titans threshold friction wind speeds. Although electrostatic forces may be attractive or repulsive, bipolar granular materials tend to cluster because an aggregated system is more energetically stable than a dissociated one (Lee et al.,

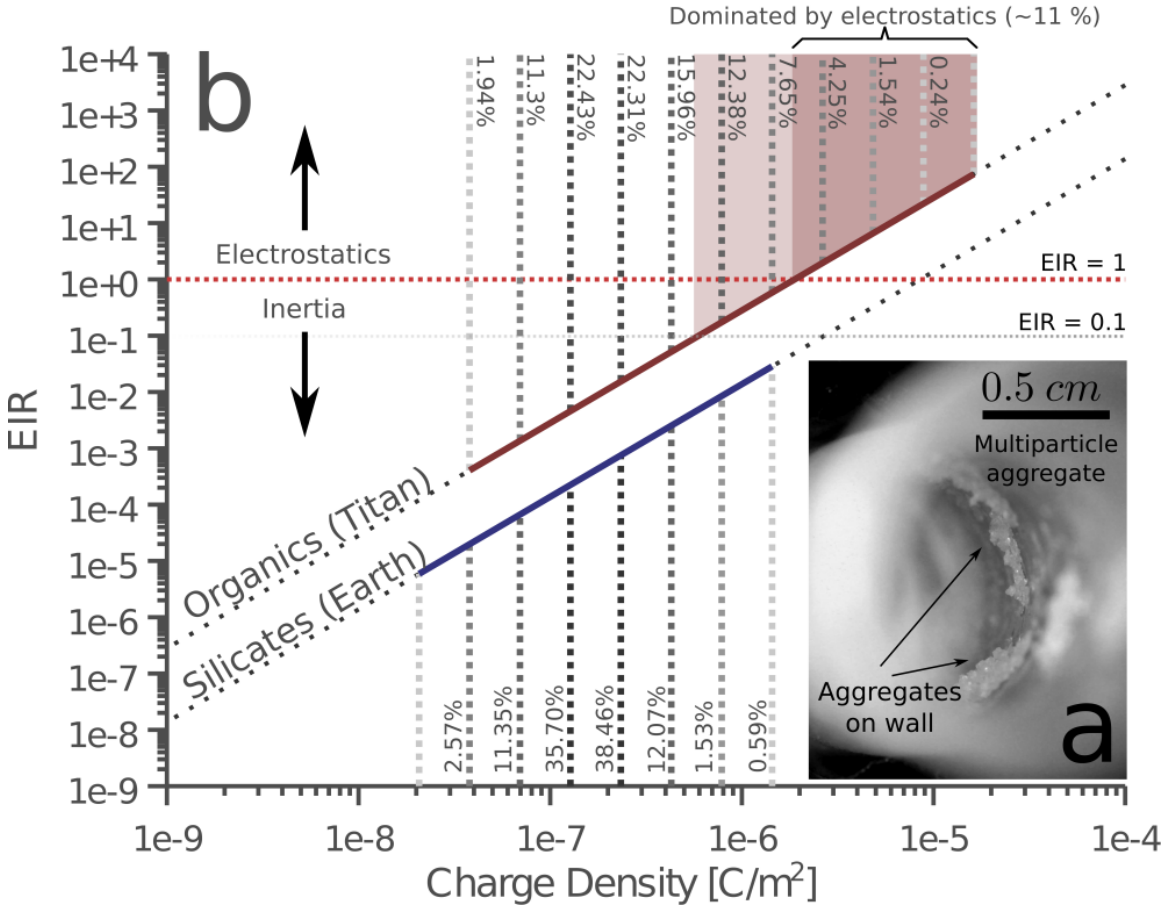

Figure 8.3: A) Photograph of a multiple particle polystyrene aggregate in our experiments. B) The range of EIR as computed from equation (1) for the average ranges of charge densities for organic and silicate materials. The solid portions of the curves bound the expected range of EIRs based on the average spans of charge density estimated for organic (red, labeled "organics) and silicate (blue, labeled "silicates) grains. The bins separated by the vertical, dotted lines report the expected fraction of grains in our experiments with a given charge density. The horizontal dotted line demarcates the boundary between inertia- and electrostatically-dominated systems (EIR = 1).

2015) (Castellanos, 2005). Working under the assumption that grains have reached an aggregated configuration (as depicted in Fig. 8.7), the expression for the threshold friction speed previously derived(Shao & Lu, 2000) can be modified to include an electrostatic force between particles that restricts motion (see Methods for complete derivation):

$$u_*^2 = A[\frac{(\rho_p - \rho_a)D_p g}{\rho_a} + \frac{\gamma}{\rho_a D_p} - \alpha\frac{F_e}{\rho_a D_p^2}] \tag{8.2}$$

Here, A is a constant experimentally found to be close to 0.0123. Parameter γ is a constant related to inter-particle forces other than capillary and electrostatic effects and is close to $10^{-4}Nm^{-1}$ (Burr et al., 2015) (Shao & Lu, 2000). The constant in the third term, α, is a geometrical parameter reflecting the stacking order of the particles and is close to 1. ρ_p, ρ_a, and g are the particle density, fluid density, and gravity, respectively. The electrostatic force in equation 8.2 is $F_e = k_C\frac{Q_1 Q_2}{h^2} - f(k, r, h)$ (Bichoutskaia et al., 2010). Again, the second term in the previous equation represents contributions from mutual polarisation (see Supplementary information, equation 8.13 for additional details). Here, we make the assumption that $Q_2 = -Q_1$. Unlike the EIR, which depends only on the charge density and material density, the addition of gravity in this relationship introduces a size dependence. Using the charge density data rendered in Fig. 8.2 and equation 8.2 the effects of electrostatics on the saltation threshold are rendered in Fig. 8.4a. For Titan conditions, significant increases (defined here to be above 10; red, dotted curve in the left panel of Fig. 8.4a) in the minimum friction threshold speeds (near $D_p = 250\mu m$) are expected to occur when the charge density on grains is greater than $10^{-6}Cm^{-2}$. As can be seen from the histogram in the right panel of Fig. 8.4a (which reflects the charge density distributions in Fig. 8.2a), approximately 26 % of organic materials in the experiments obtained charge densities that exceed this level. For particles with the highest charge densities recorded in experiments with organics under approximate Titan conditions

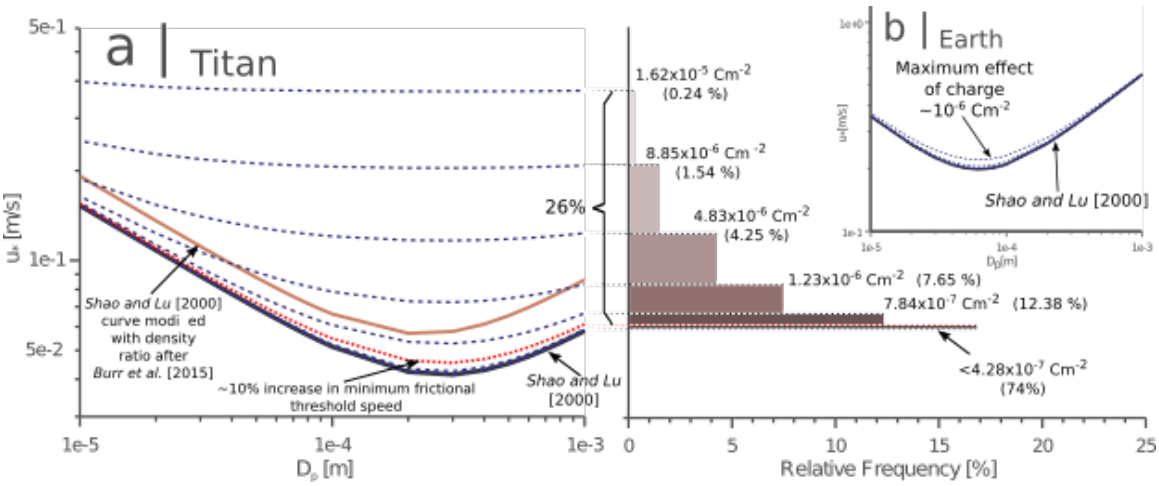

Figure 8.4: Electrostatics and the saltation threshold. A) Titan. The thick, lowest curve in the left panel is the frictional threshold without electrostatic effects taken into account. Dotted curves above this lowest curve show the modified saltation threshold given the charge densities indicated in the right panel (the average charge densities of all 3 organic materials). The lengths of the bins in the right panel give information about the relative frequency at which a specific charge density appeared in our experiments. The solid red curve shows the higher-than-expected saltation threshold including the particle-to-fluid density ratio modification. B) Earth. Even when particles are charged to their highest value, the effects of electrostatics are much less prominent in the terrestrial case.

(on the order of $10^{-5}Cm^{-2}$), the minimum frictional speed was almost an order of magnitude larger than that predicted by the expression of Shao and Lu (Shao & Lu, 2000) (Fig. 8.4a). In stark comparison, the frictional threshold for the terrestrial case remained nearly unaffected by charging, even for the highest charge densities recorded in our experiments (Fig. 8.4b).

8.4.3 Implications for Titans geomorphology

The effects of charged particles on the collective mobility of granular materials on Titan will need to be assessed through future wind tunnel experiments or numerical simulations. Nonetheless, our experiments describe a previously-undisclosed mechanism that potentially explain certain geomorphological aspects of Titan's dunes. Firstly, electrostatic forces appear to increase the frictional thresholds and would re-

sult in dune sands with internal cohesion that would require strong winds in order to become mobile. Such added consistency could help explain the mismatch between dune orientation and predicted wind vectors. Secondly, observed dune orientations have recently been shown to be consistent with a growth mechanism involving duneforms on a non-erodible or armoured bed, i.e. the fingering mode of dune elongation (Lucas et al., 2014) (Charnay, Barth, et al., 2015) (Pont, Narteau, & Gao, 2014) (Gao, Narteau, & Rozier, 2016) (Lucas et al., 2015). That triboelectric charging of aromatic hydrocarbons leads to millimetre-sized aggregates may provide a mechanism for producing this non-erodible bed (we note that an analogous electrostatic armouring occurs frequently during the transport of organic pharmaceutical powders and is called "sheeting(Hendrickson, 2006) (Sowinski, Miller, & Mehrani, 2010)). The majority of Titans dune grains likely do not acquire charges large enough to overcome the effects of wind drag and gravity. However, as demonstrated by the analysis of our experimental data, we expect an important fraction of the material to become sufficiently electrified to present substantial resistance to motion. Indeed, strong interparticle forces may arrest some particles as these stick to the substrate or aggregate to form effectively larger particles (similar to those observed in our experiments, Fig. 8.3a). Thus, sediment could be sorted in such a manner that large aggregates fill the armoured interdune regions while free particles or small, mobile aggregates compose the dunes(Gao et al., 2016) (Lucas et al., 2015). Finally, triboelectric charging may affect the dynamics of organic particles on Titan prior to their incorporation into aeolian bedforms. The fact that near-infrared spectra and the microwave emissivity of the dunes are distinct from all other terrain units on Titan suggests that particles might be sourced from the growth of haze particles, rather than from erosional and fragmentation processes at specific sources (as happens on Earth)(Barnes et al., 2008)(Bonnefoy et al., 2016). Triboelectric charging provides an efficient process for the aggregation of simple aromatic hydrocarbons, and may serve a mechanism for

the formation of dune grains with diameters of several hundred microns from micron-sized haze particles. Although the above hypotheses will need to be tested in detail by future experimental and computational efforts, the work presented here preliminarily suggests that Titan, unlike other bodies in the Solar System, may be a world moulded by grain-scale electrostatic processes.

8.5 Supplementary information

8.5.1 Methods

Particles in the experiments were charged in a rotating tumbler, the interior of which was coated with a layer of material identical in composition to that being tested. The tumbler consists of a grounded aluminum tube 15 cm in length and with an interior diameter of 2 cm. The substrate was created by either vapour deposition (for aromatic organics) or by physically attaching grains using non-volatile adhesives. All materials were sieved to obtain size distributions between 300-1000 microns. Materials were characterized with an optical microscope, revealing that organic and silicate particles have similar morphologies (Extended Data Figure 1). The fact that grains have similar shapes ensures that grain-grain interactions are similar between silicates and organics.

At the onset of an experiment, $0.2cm^3$ of grains of a particular material were inserted into the tumbler and sprayed with a commercial antistatic air gun to neutralize any initial charge. The apparatus was then placed within a pressure vessel where the environment could be finely tuned (see Table 1). Experiments with organic grains were carried out under approximated Titan atmospheric conditions consisting of a nitrogen gas environment at 300 K with <1 % relative humidity and a pressure of 0.145 MPa. Titans troposphere reaches high relative humidities with respect to methane concentration (Niemann et al., 2010), but this molecules non-polar nature makes it unlikely to affect charging as water does. The terrestrial simulations were run in air

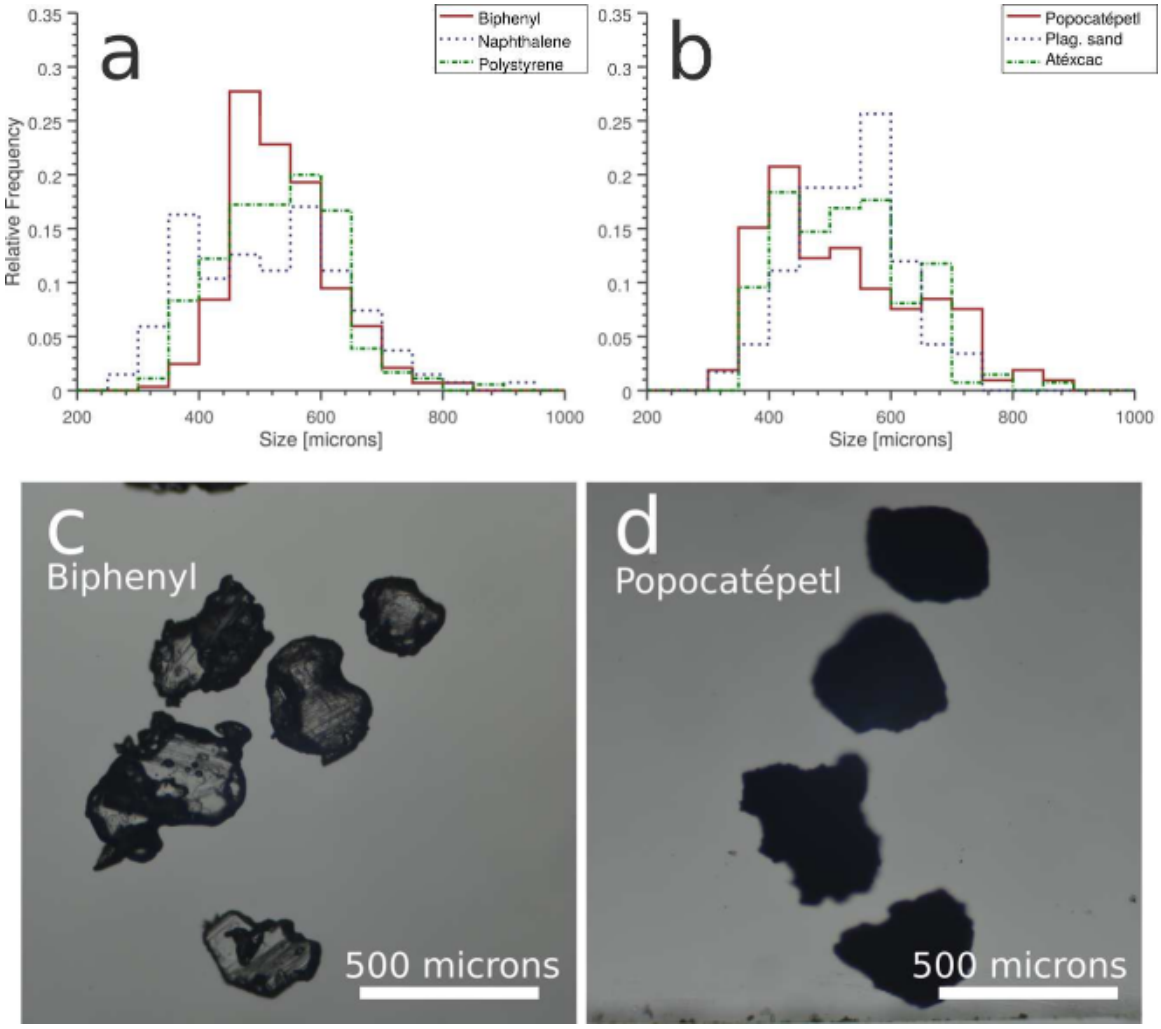

Figure 8.5: Granular materials. A) and B) show the particle size distributions of organic and silicate materials, respectively, used in the experiment. C) and D) show the similar morphology between biphenyl and Popocatépetl ash, respectively.

at room temperature with 30 RH% and a pressure of 0.1 MPa. The tumblers rotation rate was set to match the inferred minimum threshold frictional speeds–for Titan and for Earth–and each experiment lasted 20 minutes. The tumbler was driven with stepper motor to ensure a constant rotation rate. We note that speeds are somewhat lower than thresholds speeds for the used grain sizes. However, because tribocharging has been showed to scales with the kinetic energy of the flow, using the minimum predicted threshold speeds ensures that we established an absolute lower bound for charging. As the tumbler rotated, grains exchanged charge in the tumbler as they collided with each other and with the tube substrate. Once the rotation period expired, the tumbler was inclined downward, causing particles to roll out under the action of gravity (Fig. 8.1). At this point, the rotation rate of the tumbler was increased to 0.5 m/s to more effectively dislodge particles. Upon leaving the tube, particles fell through a miniature open-ended Faraday cage connected to a charge amplifier. The charge amplifier is built around an LMC6001 operational amplifier which is characterized by femtoampere input bias currents. The operation of the charge amplifier is described by:

$$V_o = \frac{-Q}{C_f} \tag{8.3}$$

In equation 8.3, Q is the charge on the particle enclosed by the Faraday tube and C_f is the amplifier feedback capacitance (in this case 100 pF). As particles traverse the Faraday tube, the charge amplifier outputs voltage pulses with magnitudes, V_o, proportional to the charge on the grains (Mendez Harper & Dufek, 2016). The charge amplifier is sampled at 6 kHz and can detect charges as small as 10 fC.

An example of raw charge data from the output of the charge amplifier is plotted in Fig. 8.6. Each peak represents the passage of a single grain through the Faraday tube. Particles charged both negatively and positively, obtaining maximum magnitudes of several picocoulombs. We note that particles preferentially charged

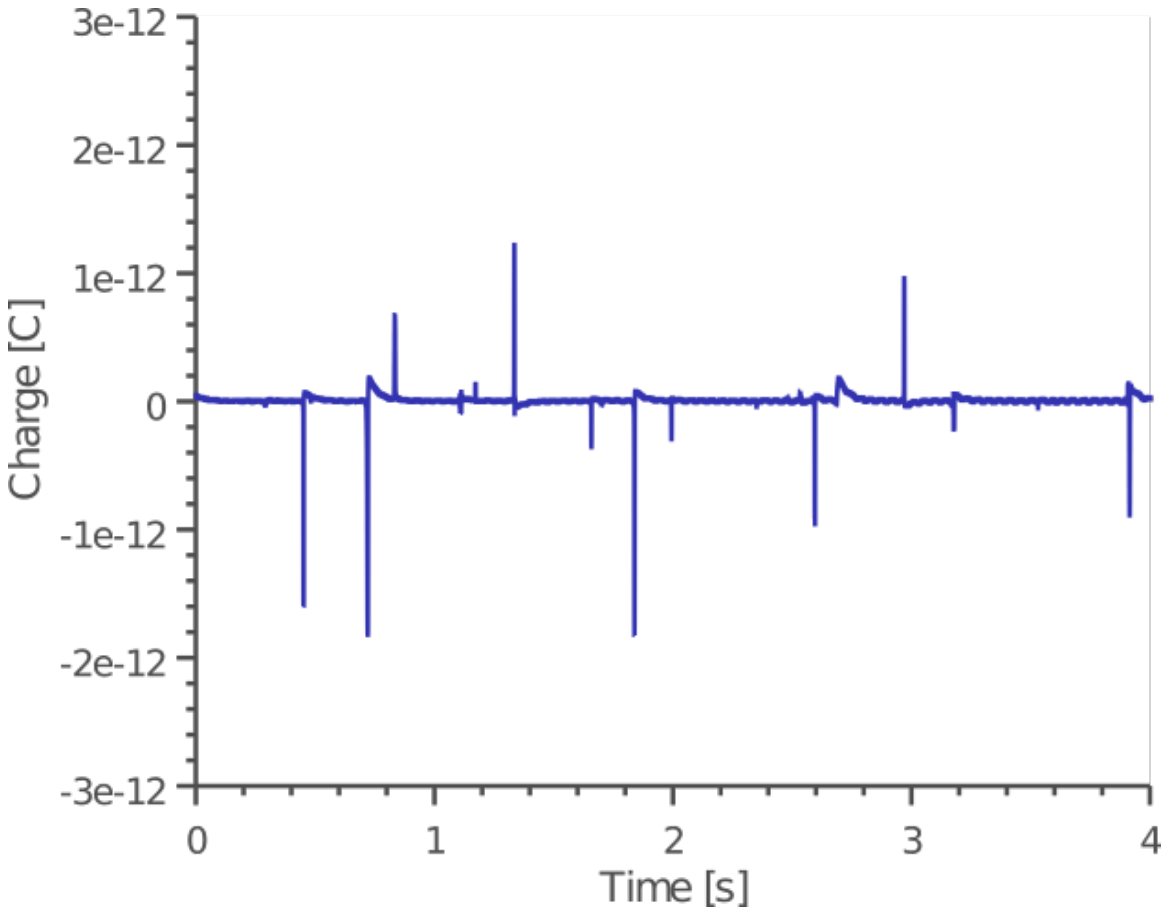

Figure 8.6: Raw charge data collected from the output of the charge amplifier. Each pulse represents the passage of a single particle through the Faraday tube. Free particles generally charge negatively because they have smaller areas than the material adhered to the tumbler wall (substrate), which is inferred to have charged positively.

negatively, implying that an overall positive charge was imparted to the material coating the interior of the tumbler. This charge separation is accounted for by the size-dependent nature of triboelectrification; when two surfaces of identical chemical composition repeatedly impact, the larger surface tends to acquire positive charge while the smaller becomes negatively charged (Lowell & Truscott, 1986a) (Lacks & Levandovsky, 2007) (Forward et al., 2009c). Grains in the experiments preferentially acquire negative charge because they have surface areas which are much smaller than the tumbler substrate. Particles were resized after experiments to determine if significant comminution had taken place. Generally, the size contributions remained unmodified from those rendered in Fig. 8.5 after the experiments. Thus, we are confident that most of the electrification occurring in our experiments are representative of frictional charging and not other processes such as fracto-emission or fragmentation charging (Mendez Harper & Dufek, 2015) (Dickinson et al., 1988).

8.5.2 The electrostatic energy between two charged dielectric spheres

The electrostatic energy between two spheres with charges Q_1 and Q_2 is often expressed simply as $U_E = k_C Q_1 Q_2 / h$ (where h is the separation been the geometric centres of the particles). This last equation, however, is only valid for point charges or non-polarisable spheres. For polarisable particles in close proximity, Bichoutskaia and others (Bichoutskaia et al., 2010) proposes that charge density on a particle σ_T can be written as a sum of contributions from the surface charge density σ_f, and the polarisation charge density σ_p, or $\sigma_T = \sigma_f + \sigma_p$. Under a multipole expansion of Legendre polynomials using spherical coordinates, the electrostatic energy between

two charged particles can be expressed as:

$$\begin{aligned} U_E = k_C \frac{Q_1 Q_2}{h} - Q_1 \sum_{m=1}^{\infty} \sum_{l=0}^{\infty} \frac{(k-1)m}{(k+1)m+1} \frac{(l+m)!}{l!m!} \frac{r^{2m+1}}{h^{2m+l+2}} A_{1,l} \\ - \frac{1}{k_C} \sum_{l=1}^{\infty} \frac{(k+1)l+1}{(k-1)l} \frac{A_{1,l} A_{1,l}}{r^{2l+1}} \end{aligned} \tag{8.4}$$

where

$$\begin{aligned} A_{1,j_1} = r_1 k_C Q_1 - \frac{(k_1-1)j_1}{(k_1+1)j_1+1} \frac{r_1^{2j_1+1}}{h^{j_1+1}} k_C Q_2 \\ + \frac{(k_1-1)j_1}{(k_1+1)j_1+1} \sum_{j_2=0}^{\infty} \sum_{j_3=0}^{\infty} \frac{(k_2-1)j_2}{(k_2+1)j_2+1} \frac{(j_1+j_2)!}{j_1!j_2!} \frac{(j_2+j_3)!}{j_2!j_3!} \\ \times \frac{r_1^{2j_1+1} r_2^{2j_2+1}}{h^{j_1+2j_2+j_3+2}} A_{1,j_3} \end{aligned} \tag{8.5}$$

In equations 8.4 and 8.5, r_i are the radii of the particles k_i and are their dielectric constants. The first term in equation 8.4 is representative of the Coulomb energy between two non-polarisable particles or point charges (with the simplifying assumption that charge is concentrated at the center of the particles). The second and third terms in equation 8.4 are contributions arising from polarisation effects and are always negative (meaning they are representative of attractive forces), and increase in magnitude with dielectric constant. An interesting aspect of polarisations is that, for certain combinations of charge and particle size, attraction between like-charged dielectric particles can occur when these are close to each other. For oppositely charged particles, the energy remains attractive. A consequence of this phenomenon is that, for polydisperse granular flows with varying degrees of charge densities (like those characterized in this work), cohesion processes may dominate over dissociative ones (Stace, Boatwright, Khachatourian, & Bichoutskaia, 2011). We refer the reader to Bichoutskaia and others(Bichoutskaia et al., 2010) for a detailed derivation

of equation 8.4. There, those authors show that the model converges rapidly for low dielectric constants and is stable for particles in contact. Equation 8.4 is used to compute the numerator in equation 8.1 assuming the interaction of two mechanically identical particles ($r_1 = r_2 = D_p/2$) in contact ($h = D_p$) with the same net charge ($|Q_2| = |Q_1| = \pi D_p^2 |\sigma_f|$).

8.5.3 A note on the EIR

The electrostatic-to-inertial ratio (EIR) is given as: $EIR = |U_E|/U_I$. For two mechanically identical particles in contact of the same composition and charge, the EIR does not depend on particle size, because both $U_E \propto r^3$ and $U_E \propto r^3$. Thus the electrostatic-to-inertial ratio depends only on the density of the particle material and the surface charge density. For the sake of briefness, consider the EIR computed only with the first term in of the electrostatic energy (i.e. ignoring the polarization terms): $U_E = k_C \frac{Q_1 Q_2}{h}$. From this, one obtains:

$$EIR = \frac{2k_C Q_1 Q_2}{h m_r v^2}. \tag{8.6}$$

Here, $Q = Q_1 = Q_2$, $m = m_1 = m_2$, $m_r = 0.5m$, $r = r_1 = r_2$ and $h = 2r$. Thus:

$$EIR = \frac{2k_C Q^2}{r m_r v^2}. \tag{8.7}$$

.

Furthermore, $Q = 4\pi r^2 \sigma_f$ (where σ is the surface charge density) and $m = 4/3\pi r^3 \rho_p$. As such, equation 8.7, can be simplified as:

$$EIR = \frac{24k_C \pi \sigma_f^2}{\rho_p v^2}. \tag{8.8}$$

,

which depends only on the density of the particles and their surface charge den-

sities.

8.5.4 An expression for the saltation threshold including inter-particle electrostatic effects

In a flow composed of both negatively and positively charged material, attractive electrostatic interactions dominate because clustering minimizes the electrostatic energy between grains (James et al., 2002) (Lee et al., 2015) (Castellanos, 2005) (Bichoutskaia et al., 2010). The following derivation of the expression for friction threshold speed including electrostatic forces starts from the assumption that grains have coalesced into electrostatically bound clusters.

The derivation of the threshold friction speed parallels the steps described in Shao and Lu(Shao & Lu, 2000). For the three-particle arrangement rendered in Fig. 8.7, the threshold friction speed at the instant saltation is initiated can be obtained from the sum of moments around a pivot point P. All particles are assumed to be mechanically identical. The sum of moments is given as:

$$r_d F_d \approx r_g F_g + r_i F_i \tag{8.9}$$

. Here, r_d, r_g, r_i are the moment arms in Fig. 8.7 and are proportional to the grain size D_p: $r_d = a_d D_p$, $r_g = a_g D_p$, and $r_i = a_i D_p$. Constants a_d, a_g, and a_i depend on the stacking order of the grains. The term on the left side of equation 8.9 is the drag force, F_d, and is given by:

$$F_d = K_t \rho_a D_p^2 u_o^2 \tag{8.10}$$

.

where K_t is a dimensionless parameter, ρ_a is the density of the air ($5.28 kgm^{-3}$ for Titan), and u_o is the surface friction speed. The first term on the right side represents

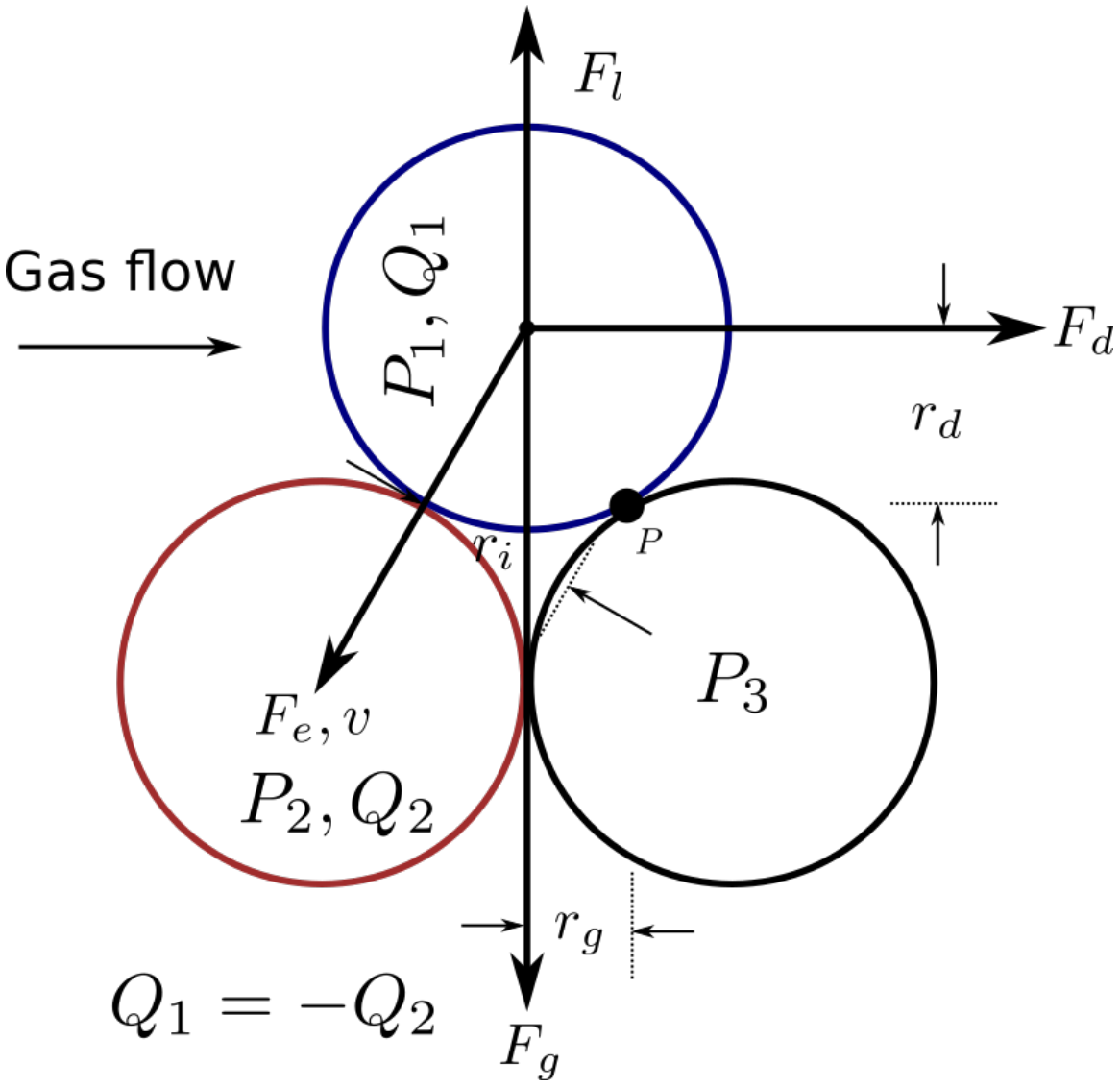

Figure 8.7: Forces acting on a negatively charged particle (blue) resting on a positively charged substrate of particles (red) exposed to a wind stream. F_g is the force due to gravity, F_d is the drag force, F_b is a buoyancy force, and $F_{e,v}$ is the inter-particle force including electrostatic and van der Waals forces. Particles are assumed to be the same size and have equal absolute charge densities.

the effective gravitational force, F_g:

$$F_g = \pi/6(\rho_p - \rho_a)gD_p^3 \tag{8.11}$$

.

where g is the gravitational acceleration ($1.32ms^{-2}$ for Titan) and ρ_p is the particle density ($1000kgm^{-3}$). The second term on the right side, F_i, encompasses interparticle forces. Note that for the selected geometry (Fig. 8.7), only the interparticle forces between the top and bottom-left particles (denoted in Fig. 8.7 as particle P1 and particle P2, respectively) are of concern since the moment arm associated with the interparticle force between P1 and the bottom-right particle, P3, has a length of zero. Thus, the moment around the pivot point is zero. Ignoring capillary and electrostatic forces, Shao and Lu (Shao & Lu, 2000) propose that the particle force, namely van der Waals forces, F_v, could be expressed as:

$$F_v = \beta D_p \tag{8.12}$$

.

In this expression, β is a dimensional parameter on the order of $10^{-4}Nm^{-1}$. The electrostatic force between two polarisable particles has been expounded on by Bichoutskaia and others(Bichoutskaia et al., 2010):

$$\begin{aligned} F_e = k_C\frac{Q_1Q_2}{h^2} - Q_1\sum_{m=1}^{\infty}\sum_{l=0}^{\infty}\frac{(k_2-1)m(m+1)}{(k_2+1)m+1}\frac{(l+m)!}{l!m!}\frac{r_2^{2m+1}}{h^{2m+l+3}}A_{1,l} \\ - \frac{1}{k_C}\sum_{l=1}^{\infty}\frac{(k_1+1)(l+1)+1}{(k_1-1)}\frac{A_{1,l}A_{1,l+1}}{r_l^{2l+3}} \end{aligned} \tag{8.13}$$

.

$A_{1,j}$ is given in equation 8.5. We note that this expression is stable even for

particles in contact. For particles P1 and P2 (Fig. 8.7) we assume that $Q_1 = -Q_2$ These charges can be calculated from the surface charge densities σ_f obtained from experiments:

$$Q_i = \begin{cases} \pi D_p^2 \sigma_f, & i = 1 \\ -\pi D_p^2 \sigma_f, & i = 2 \end{cases} \tag{8.14}$$

.

With the expression for the interparticle force, $F_i = F_e + F_v$, equation 8.9 can now be re-written as:

$$a_d K_t \rho_a u_o^2 D_p^3 = a_g \frac{\pi}{6}(\rho_p - \rho_a) g D_p^4 + a_i D_p(\beta D_p + F_e) \tag{8.15}$$

. Rearranging this expression, we arrive at equation 8.2:

$$u_*^2 = A[\frac{(\rho_p - \rho_a) D_p g}{\rho_a} + \frac{\gamma}{\rho_a D_p} - \alpha \frac{F_e}{\rho_a D_p^2}] \tag{8.16}$$

where

$$A = \frac{\pi}{6}\frac{a_g}{a_d}\frac{1}{K_t} \tag{8.17a}$$

$$\gamma = \frac{6}{\pi}\frac{a_i}{a_g}\beta \tag{8.17b}$$

$$\alpha = \gamma\beta \tag{8.17c}$$

Note that equation 8.2 is identical to that reported in Shao and Lu(Shao & Lu, 2000) except for the addition of the electrostatic term on the right side. Fitting equation equation 8.2 to the experimental data of Iversen and White(Iversen & White, 1982), Shao and Lu found that $A \approx 0.0123$ and $\gamma \approx 10^{-4} kgs^{-1}$ for a broad range of particle sizes (Burr et al., 2015) (Shao & Lu, 2000). Furthermore, $\beta \approx 10^{-4} Nm^{-1}$

40, thus α is approximately 1. Because A and γ have been estimated empirically, there is some uncertainty associated with them. Thus, to make our work compatible with previous saltation calculations relevant to Titan we employ the values reported in Burr and others(Burr et al., 2015). In equation 8.2, the sign of the electrostatic force has been changed to reflect the fact that attractive forces are negative, while repulsive ones are positive.

CHAPTER 9
TRIBOELECTRIFICATION OF KCL AND ZNS PARTICLES WITH APPLICATIONS TO GJ1214B

9.1 Introduction

Electrification and discharge phenomena are common in the Solar System's planetary bodies and likely affect the atmospheres of extrasolar objects such as brown dwarfs and exoplanets (Helling et al., 2013)(Helling et al., 2016) (Vorgul & Helling, 2016). In the Solar System, lightning and, by extension, electrification processes have been confirmed on Earth (Marshall et al., 1995) (McNutt & Williams, 2010) (Dwyer & Uman, 2014), Saturn (Warwick et al., 1982) (Read, 2011), and Jupiter (Rinnert et al., 1998) (Dyudina et al., 2001). Indirect evidence for atmospheric electrification exists for Uranus and Neptune and lightning may be a possibility in the Venusian atmosphere at elevation (Zarka, Farrell, Fischer, & Konovalenko, 2008) (Harrison, Aplin, Leblanc, & Yair, 2008) (Yair, 2008). In many atmospheres, electrical processes are driven by the interaction of liquid droplets and ice crystal composing clouds. However, electrification and discharges may also occur in dusty regimes devoid of volatile components. On Earth, the most dramatic examples of this dusty electrification are perhaps the brilliant displays of lightning that often accompany volcanic eruptions (Pliny The Younger, 1963) (Thomas et al., 2009) (Behnke et al., 2013)(Cimarelli et al., 2016). Granular charging may also occur in dust storms and, certainly, within a wide range of industrial and man-made environments (Hendrickson, 2006) (Matsusaka et al., 2000) (Lacks & Sankaran, 2011). In Martian dust devils, charging may lead to small-scale discharges or corona (Krauss et al., 2003) (Farrell et al., 2015). Similar processes– either spark or corona discharges–are likely active on extrasolar planets with mineral hazes and clouds such as HD189733b, Kepler 7b, or GJ1214b (Sing et al., 2009) (Pont, Knutson, Gilliland, Moutou, & Charbonneau, 2008)(Helling et al., 2013).

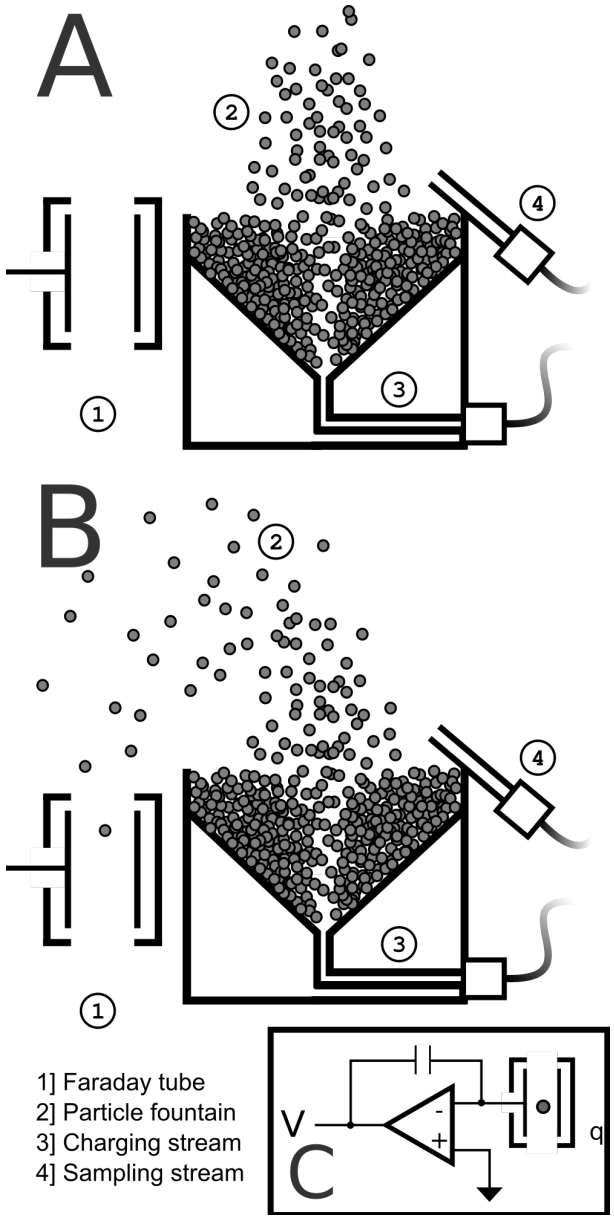

Figure 9.1: Experimental apparatus. Particles are charged in fluidized bed that generates many particle-particle collisions, while minimizing interactions with foreign surfaces. The design has been describe in detail in Forward, Lacks, and Sankaran, 2009c, Bilici, Toth, Sankaran, and Lacks, 2014 and Mendez Harper and Dufek, 2016. Panel A shows the operation during the charging period, while panel B shows the system during the measurement period.

Unlike the charging processes that occur in thunderclouds, which are driven by grauple, ice, and super-cooled water droplets (Marshall et al., 1995) (Dwyer, 2005), charging in dry granular flows may be a consequence of frictional collisions between particles (Lowell & Truscott, 1986a) (Lacks & Levandovsky, 2007) (Apodaca et al., 2010), fragmentation of particles (Dickinson et al., 1984)(Donaldson et al., 1990) (James et al., 2000) (Mendez Harper, Cimarelli, et al., 2017), through induction (Pahtz et al., 2010), the photoelectric effect (Yair, 2008), or radioactivity (Houghton et al., 2013). Frictional electrification–also referred to as triboelectrification–is "the oldest manifestation of electricity known to man, [yet] it still remains today quite obscure as to the mechanisms active" (Kunkel, 1950). Indeed, the nature of the charge carriers being exchanged when two surfaces come into contact (Lacks & Sankaran, 2011) has not been resolved. One model–the trapped electron model–suggests that particles become charged as electrons trapped in unfavorable energy states on one surface migrate to low energy states on another particle during particle-particle collisions (Lowell & Rose-Innes, 1980) (Lowell & Truscott, 1986a) (Lowell & Truscott, 1986b). Such model has gained a considerable degree of acceptance because it not only accounts for electrification in systems of chemically identical grains, but can explain why smaller grains tend to charge negatively while larger ones gain positive charge (i.e. the size-dependent bi-polar charging of chemically-identical substances) (Forward et al., 2009a) (Lacks & Sankaran, 2011) (Bilici et al., 2014).

Recently, Kreidberg et al., 2014 showed that the flat transit spectrum associated with GJ1214b could be explained by the presence of high altitude (1 - 0.1 kPa) clouds or organic hazes. The pressure and temperature conditions at GJ1214b, which orbits closely around a M4.5-class red dwarf (Charbonneau et al., 2009), indicate that if clouds are present, volatile species do not comprise them. Instead, clouds may be composed of condensed (solid) salts such as potassium chloride (KCl) or zinc sulfide (ZnS). While organic hazes, similar to those found in the atmosphere of Titan, have

also been invoked to account for observations, a mechanism for their formation has not been proposed (Kreidberg et al., 2014). If salt clouds are, in fact, the source of the GJ1214b's flat transmission spectrum, Gao and Benneke, 2016 suggest that constituent particles must form at depth (where the pressure is 100 - 10 kPa) and are then lofted by strong atmospheric circulation. During advection, grains likely undergo energetic particle-particle collisions, driving efficient triboelectrification. Because the ascent rate depends on particle size, small, negative grains likely become concentrated at the top of the clouds while large, positive grains remain at lower elevation. Much like in thunderclouds and volcanic plumes (Kikuchi & Endoh, 1982) (James et al., 1998) (Cimarelli et al., 2014) (Mendez Harper, Cimarelli, et al., 2017), this separation of charge may set up coherent electric fields which could drive spark discharges–lightning–either through conventional breakdown of the gas (Paschen, 1889) or via runaway electron avalanche (Dwyer, 2005) (Helling et al., 2013).

In this work, we explore the triboelectrification of KCl and ZnS grains under approximated GJ1214b conditions. We show that both materials become charged when fluidized and attain charge densities comparable to those observed on ash particles falling out of volcanic plumes and thunderstorm water droplets.

9.2 Methods

Triboelectrification of KCl and ZnS grains was achieved using an apparatus similar to that previously described in Forward et al., 2009b and Mendez Harper and Dufek, 2016. The device the consisted of a spouted bed contained within an environmental chamber (Figure 9.1a and 9.1b). The spouted bed was made from a machined steel cup (width = 6 cm, depth = 6 cm) capable of holding 100 g of particles. A 500 micron-hole milled in the center of the cup's base allowed a stream of gas to enter the granular bed and generate particle motion (fountaining). The geometry of the cup was selected to generate copious particle-particle collisions, while minimizing particle-

wall contacts. Thus, triboelectric charging in this work stems overwhelmingly from the interaction of chemically-identical surfaces (Figure 9.1 and Figure 9.2).

We used commercially available KCl and ZnS powders in our experiments. The materials were sieved to obtain nominal sized distributions ranging between 125-500 μm (nominal). True size distributions are rendered in Figure 9.2. The apparatus was placed in a closed-loop controlled furnace where the temperature was maintained at 550-600 K (within the range of temperatures suggested for GJ1214b), 100 kPa of air (1 bar), and a relative humidity of <1%. Once the experimental setup equilibrated with the surrounding atmosphere (4 hours), a valve was opened allowing a jet of air to pass through the hole in the base of the cup, resulting in a particle fountain 3-4 cm high (Figure 9.3). Fountaining under these conditions was allowed to proceed for 20 minutes, a period long enough to ensure that particles reached an electrostatic steady state (Forward et al., 2009a) (Mendez Harper & Dufek, 2016). At the conclusion of the charging period, a second air stream was generated nearly perpendicular to the base of the fountain, catapulting suspended grains out of the fountain and into a micro-machined through-type Faraday cup (TTFC; see Figure 9.2a and 9.1b). The aperture of the Faraday cup is 1 mm in diameter, allowing only a few particles to traverse into its interior at a time. When a charged grain entered the cup it produced a current that flowed from the cup's interior electrode to a charge amplifier. The amplifier then generated a voltage pulse proportional to the charge on the particle. In this manner, we were able to characterize the charge on individual particles with a resolution of 10 fC.

While GJ1214b has an atmosphere that is either water-rich or of solar composition (H_2 or He), the use of dry air in our experiments was justified by the analysis presented in Helling et al., 2013. These investigators found the electrostatic processes on exoplanets are not largely dependent on gas composition. While we continue their reasoning in our experiments, we do so with caution given that the effect of envi-

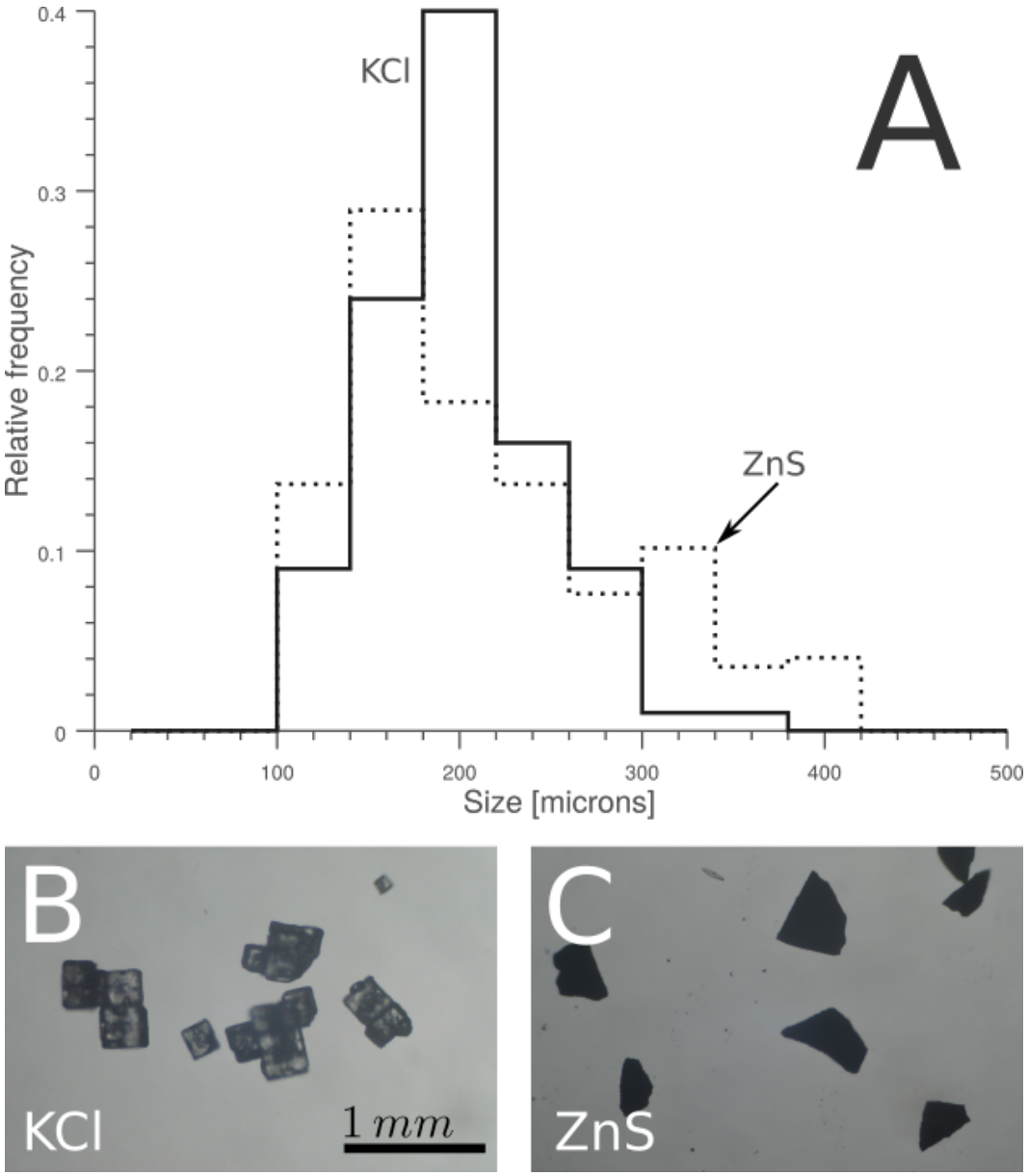

Figure 9.2: A) Grain size distributions (spherical-particle equivalents) used in these experiments for KCl (solid curve) and ZnS (dashed curve). B) Micrograph of KCl particles. C) Micrograph of ZnS particles.

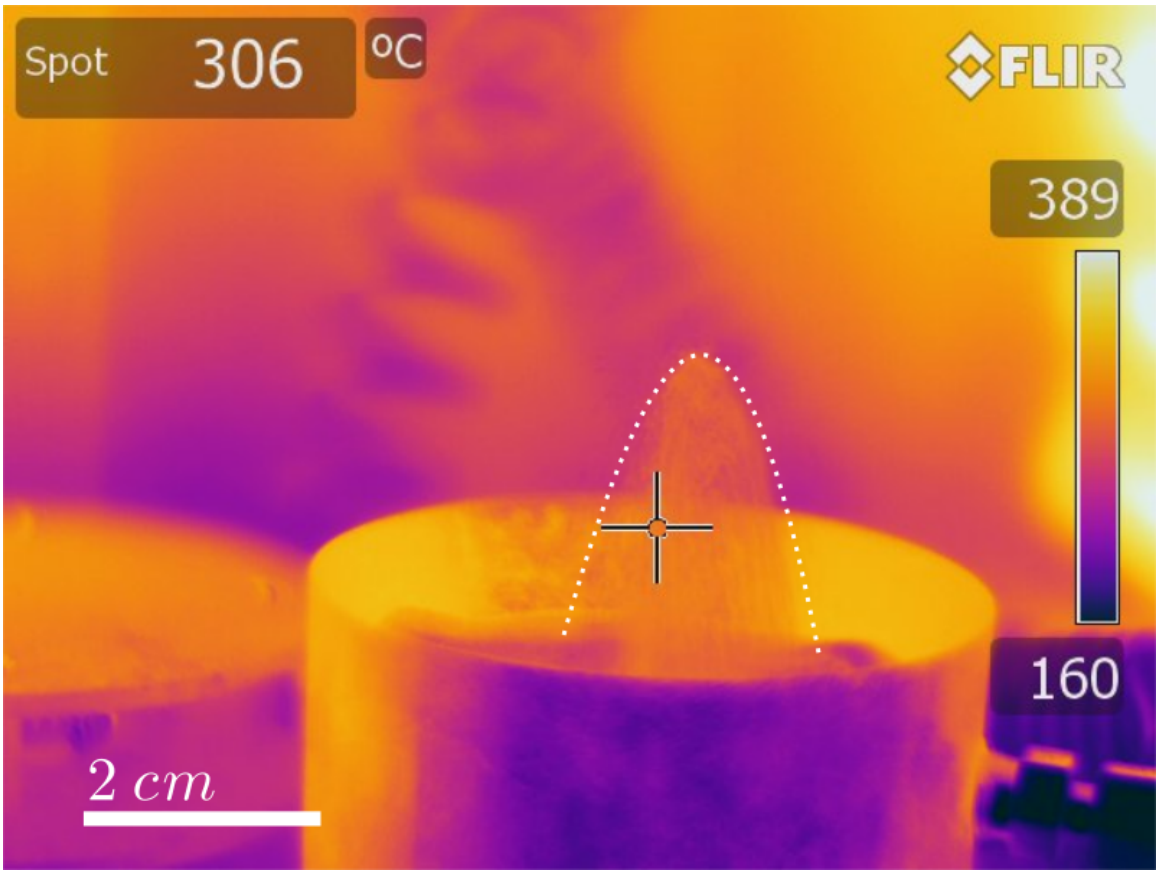

Figure 9.3: Thermal infrared image of the experimental apparatus in the furnace. Spot temperature of the fountain (outlined by dotted curve) is 300 °C (580 K)

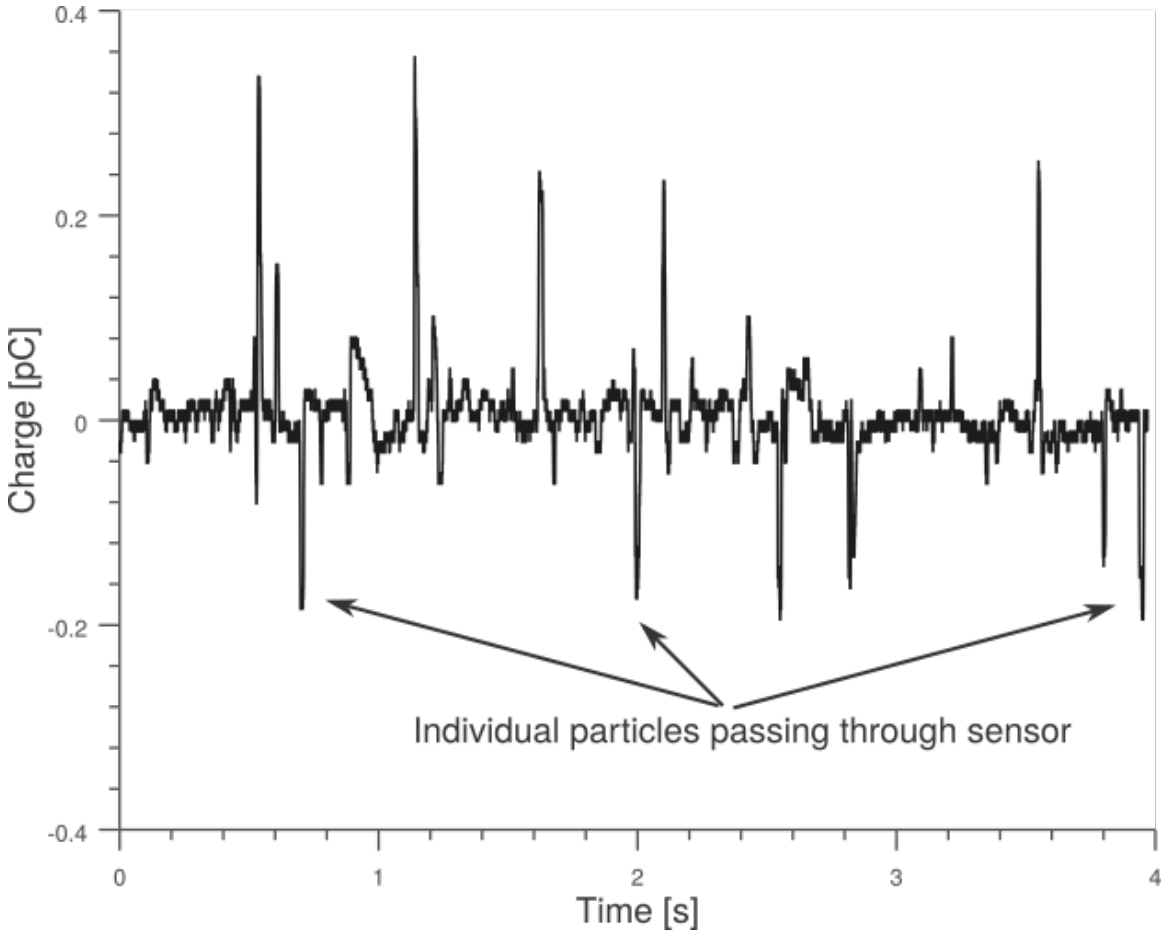

Figure 9.4: Raw charge data collected from the output of the charge amplifier. Each pulse represents the passage of a single particle through the Faraday tube.

ronmental conditions on triboelectric charging are poorly constrained. Indeed, some experiments have found no correlation between granular electrification and gas composition (Merrison et al., 2012) while others have reported clear dependencies (Mendez Harper & Dufek, 2016) (Matsuyama & Yamamoto, 1995). Until such questions are resolved definitely, the results presented here should be considered preliminary and of first order.

9.3 Results

Raw data from an experiment with KCl is shown in Figure 9.3. Each pulse represents a single particle traversing the TTFC. Particles of both materials attained maximum

charges of several 100 to 1000 fC. Note that particles charged both negatively and positively, satisfying conservation of charge. For each substance, we characterized the charge on 700-800 particles. A standard way of assessing the chargeability of a material, however, is to analyze its *charge density* or its charge normalized by its surface area. Here, charge densities for both KCl and ZnS were obtained by dividing the particle the charge distributions by the average particle area (Figure 9.2). Comparable to those reported in experiments with volcanic ash and sand, the charge densities for both KCl and ZnS range between 10^{-9} - 10^{-6} Cm^{-2} (See Figure 9.5a). Indeed, Miura et al., 2002 found that ash particles falling out of volcanic plumes held maximum charge densities ranging between 10^{-6} - 10^{-5} Cm^{-2}. Similar values were observed during experiments by James et al., 2002 and Mendez Harper and Dufek, 2016. While both substances attained similar maximum charge densities, the charge density distribution for KCl is broader than that of ZnS, meaning that a greater number of KCl particles held elevated charge densities. This discrepancy may be attributed to differences in particle morphology. While KCl grains are cubic in shape, ZnS grains are much more angular (Figure 9.2b). Sharp tips on these grains may promote charge loss resulting in overall smaller charge densities for ZnS grains.

9.4 Discussion

In dusty atmospheres, breakdown processes can occur on a wide range of scales and are controlled by a variety or microphysical mechanisms. Spark discharges between two charged surfaces (two capacitor plates, say) may occur when the electric field between these surfaces exceeds the dielectric breakdown of air, creating a conducting channel that carries charge between the two. Lightning is a natural example of a spark discharge. The presence of a single, highly charged object in a fluid may also produce a discharge, by creating a region of plasma in the vicinity of its surface in which charge is lost directly to the surface (Cross, 1987). Partial discharges of this

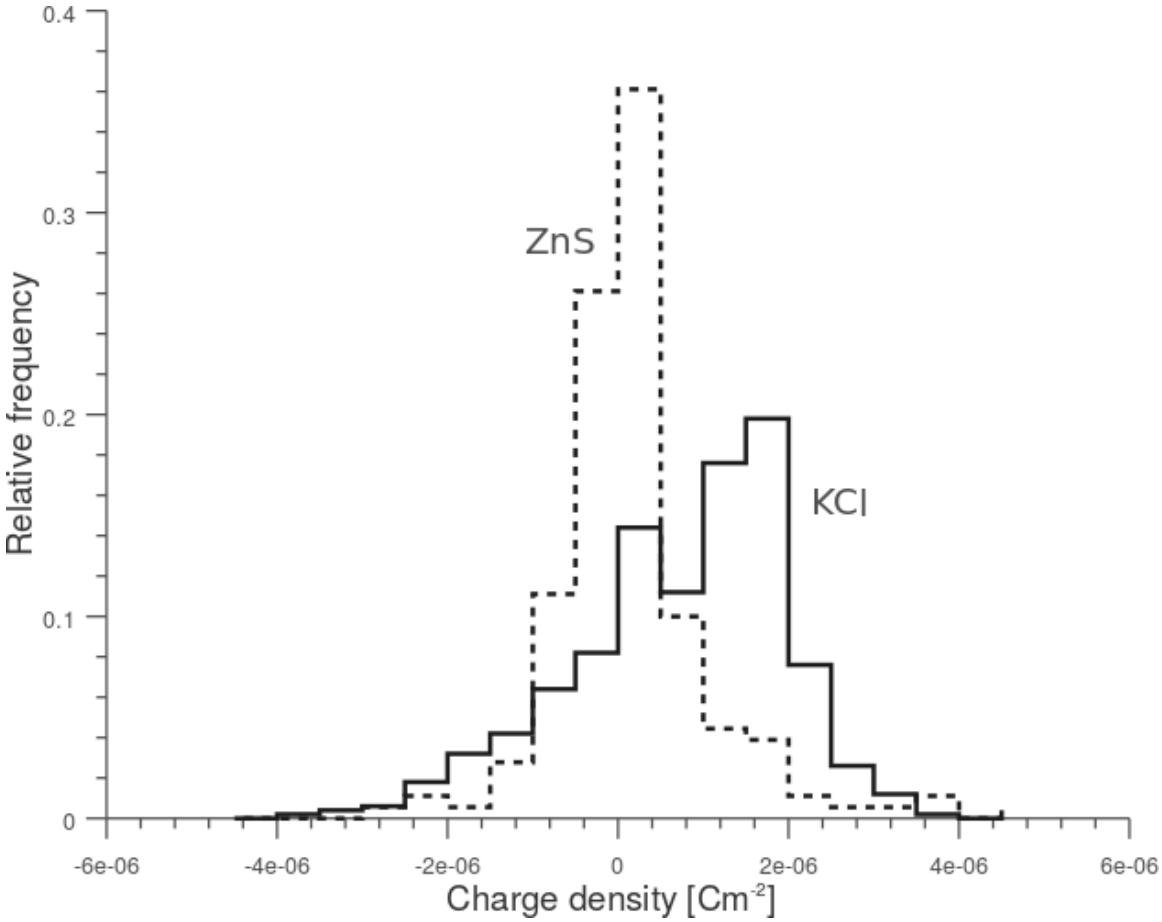

Figure 9.5: A) Mean charge density distributions for KCl (solid) and ZnS (dashed). Note that while both materials have comparable maximum charge densities, KCl has an overall broader distribution that ZnS. The higher chargeability of observed in the KCl flow may be attributed to particle shape. While KCl grains are cubic, ZnS particles are much more angular. Charge on ZnS may be lost at sharp particle tips, reducing the charge densities on grains (9.2b and c). B) From the charge density distributions, the maximum absolute charge on particles composing the GJ1214b's clouds can be determined. The maximum charge on particles ranges between a femptocoulomb for 1-10 μm grains to less than an attocoulomb for the smallest particles (0.1 μm)

sort often create visble, crown-like glows around the charged object and are known as corona discharges. During the age of square-rigged sailing ships, corona was often observed during foul weather surrounding mastheads and yardarms–Saint Elmo's fire. Partial discharge may also cause losses along high-voltage power lines if these are not properly designed (Bartnikas, 1990).

Using the charge densities measured in our experiments we can explore the conditions that will lead to electrostatic breakdown in a cloud composed of KCl or ZnS particles. The maximum voltage, V_b that can be sustained between two charged surfaces–again, the plates of an imaginary capacitor–is dependent on the composition of the enveloping gas and its pressure (Paschen, 1889) (Mendez Harper, McDonald, et al., 2017). This relation is known as Paschen's law:

$$V_b = \frac{Bpd}{\ln(\frac{Apd}{\ln(1/\gamma+1)})} \tag{9.1}$$

In equation 9.1, p is pressure, A and B are constants that give Townsend's ionization coefficient, and γ is Townsend's second ionization coefficient with a value of 0.01 (Kok & Renno, 2009). These constants are listed for a number of gases in Table 9.1 (Raizer, 2011) (Helling et al., 2013). For the present application, however, it is more useful to describe the dielectric strength of the atmosphere in terms of a breakdown electric field E_b rather than a voltage (Kok & Renno, 2009):

$$E_b = \frac{Bp}{\ln(\frac{Apd}{\ln(1/\gamma+1)})} \tag{9.2}$$

From equation 9.2, it follows that the breakdown field on Earth (with a pressure of 100 kPA or 1 bar) across a distance of 1 m is on the order of 10^6 Vm^{-1}. Exceeding these fields causes the gas to conduct. On GJ1214b, whose atmosphere is likely of solar-composition or water-rich (Charnay, Meadows, et al., 2015), Paschen's curve predicts lower breakdown fields for the same gas pressure. For H_2 and He, E_b = 8

Table 9.1: Paschen curve parameters for a number of gases

Gas	**A (m^{-1} Pa^{-1})**	**B (V m^{-1} Pa^{-1})**
H_2	3.75	97.50
He	2.25	25.50
H_2O	9.75	217.50
Air	11.25	273.77

$\times$ 10^5 Vm^{-1} and E_b = 2.5 $\times$ 10^5 Vm^{-1}, respectively, while a water-rich atmosphere would breakdown at 1.8 $\times$ 10^6 Vm^{-1}. For each of these three gases (H_2, He, H_2O) and air, the variations in breakdown field with pressure are rendered in figure 9.6a. Note that for all pressures, helium is the weakest gas (i.e. it breaks down at lower electric fields for a given pressure), while air is the strongest. Between atmospheric compositions considered here, E_b has a variation close to an order of magnitude.

Given a breakdown field, one can compute the maximum charge density that can be supported on the two surfaces of the hypothetical capacitor (Hamamoto et al., 1992):

$$\sigma_b = \epsilon_r \epsilon_o E_b \tag{9.3}$$

where ϵ_r is the relative dielectric constant of the gas and ϵ_o is the permittivity of free space. For Earth (at 100 kPa), this expression yields 2.7 $\times$ 10^{-5} Cm^{-1}. In hydrogen, helium, and water atmospheres (again, at 100 kPa), the breakdown charge densities are 7.6 $\times$ 10^{-6} Cm^{-1}, 2.0 $\times$ 10^{-6} Cm^{-1}, 1.6 $\times$ 10^{-5} Cm^{-1}, respectively. The variation of the maximum charge density with pressure is rendered in figure 9.6b for the four gases. On this same plot, we superimpose the highest charge densities observed in our experiments which have magnitudes of 4 $\times$ 10^{-6} Cm^{-2} (for both KCl and ZnS). While the charge densities associated with KCL and ZnS remain below the breakdown limits for an air or a water atmosphere at 100 kPa, they approach

or exceed those of He and H_2 (at 100 kPa). In the case of GJ1214b, theoretical considerations and numerical models have suggested that salt clouds are generated within the atmosphere at pressures close to 100-10 kPa, but are then lofted to elevations where the pressures range between 1 and 0.1 kPa (Kreidberg et al., 2014) (Charnay, Meadows, et al., 2015) (Gao & Benneke, 2016). Thus, surfaces that achieve charge densities comparable to those in our experiments while at depth likely become charge-saturated when they are advected to more rarefied regions. Exceeding the Paschen limit, such surfaces would require to shed charge through either spark or partial discharge processe (See fig 9.6b).

However, in a cloud, charge is not distributed across a continious surface (as would be the case for the capacitor plate we have been using as an analogy), but among many discrte particle surfaces. Consider a spherical cloud with surface area S_c and volume V_c. To generate a discharge at the cloud's surface, the superposition of the electric fields associated with individual grains must produce a total field E_s that exceeds the breakdown value E_b:

$$\oint E_s dS_c = Q(n, \sigma_p)/\epsilon \tag{9.4}$$

Here, Q is the total charge in the cloud which depends on both the number of grains with area A_p per unit volume n and their charge densities σ_p:

$$Q = \sigma_p A_p V_c n \tag{9.5}$$

Solving equation 9.4 (which is nothing more than a rendition of Gauss's Law) for the particle charge density and setting $E_S = E_b$, yeilds:

$$\sigma_p = \frac{3E_b(p)\epsilon}{\pi D_p^2 n R} \tag{9.6}$$

Equation 9.6 shows that the maximum charge density that can be supported on an

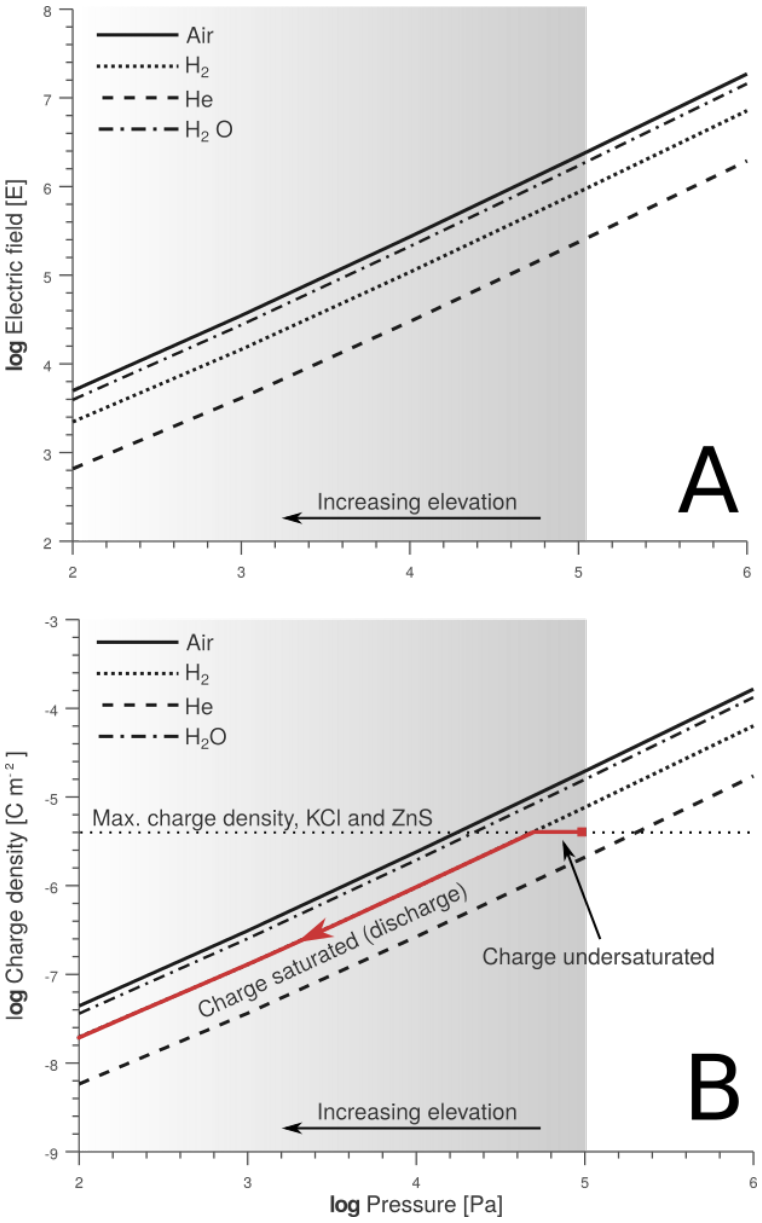

Figure 9.6: A) Maximum electric field across a 1 m spacing for air (solid), H_2O (dashed-dotted), H (dotted), and H_2 (dashed) as a function of pressure. B) Maximum charge density for a surface in air (solid), H_2O (dashed-dotted), H (dotted), and H_2 (dashed) as a function of pressure. Horizontal dotted line is representative of maximum charge densities measured in our experiments. The shaded area is representative of pressures expected in the clouds of GJ1214b. The thick, solid red curve staring with a square represents the electrostatic narrative of a charged particle as it is advected to elevations with lower pressure in an H_2 atmosphere

individual particle in the cloud σ_p may be smaller or larger than that given by equation 9.3 (σ_b) depending on the size and abundance of grains. Indeed, σ_p will be smaller than σ_b if $3/\pi D_p^2 nR < 1$. In other words, the discharge threshold becomes easier to attain in spatially extensive clouds with a high number density of large particles. Such conclusion makes intuitive sense; to generate a given electric field at the cloud surface, a cloud with many, large particles within a given volume requires constituent particles to carry less charge per grain than a small, dilute cloud with few small particles. Based on the insight gained from equation 9.6, how do the charge densities obtained from our experiments compare to those required to produce breakdown in the atmosphere of Gj1214b? From numerical models, Gao and Benneke, 2016 suggest that the maximum number density in the clouds of GJ1214b range between 10^4 and 10^5 m^{-3} and have sizes ranging from 0.1 to 1 μm. Assuming a cloud 10 km in diameter, the charge densities per particle required to generate an electric field equal to E_b (for P = 0.1, 1, 10, and 100 kPa) at the edge of the cloud are rendered in figures 9.7 and 9.8 for hydrogen and helium atmospheres, respectively. The charge densities for a particle number density of 10^4 m^{-3} are plotted in figures 9.7a and 9.8a, while those assuming concentrations of 10^5 m^{-3} are shown in figures 9.7b and 9.8b. The horizontal dotted lines indicate the maximum charge densites obtained from our experiments. As expected, for a given concentration, clouds with larger particles harbor grains with smaller surface charge densities. Because gravitational separation tends to concentrate large grains lower in the atmosphere, breakdown may proceed with greater ease in these regions despite the increased dielectric strength of the gas. Conversely, for clouds with very small particle sizes (assuming a constant concentration), individual grains must carry charge densities that exceed the theoretical maximum (27 μC m^{-2}) by several orders of magnitude to allow E_s to exceed E_b. While it may seem folly to suggest that grains hold charge densities greater than the theoretical maximum, we note that the limiting value quoted above only holds for large surfaces (Hamamoto et al., 1992).

As the radius of grains becomes increasingly small, so does the region of very high electric field surrounding it. Indeed, nanometer- to micron-sized grains have been observed to retain charge densities as high as 1000 μC m^{-2} (Hamamoto et al., 1992). Thus, we expect dilute clouds to have the ability to maintain large charge densities before entering breakdown conditions.

From the discussion up until this point, it would appear that the charge densities derived from our experiments may be insufficient to generate breakdown in the higher regions of the clouds. Yet, we have only considered discharge processes resulting from the direct dielectric failure of the gas. When charge is distributed across many surfaces in large volumes, alternate processes may allow for discharges under weaker electrical stresses. Dispersed particles in a gas, for instance, tend to lower the breakdown field by acting as lenses that concentrate electric field lines at their surfaces (Cookson & Farish, 1970) (Schroeder, Baker, & Latham, 1999)(Solomon, Schroeder, & Baker, 2001). Such focusing becomes more important as the contrast between the atmospheric dielectric constant and that of the grains increases. In thunderstorms, for instance, the maximum electric field may be reduced by a factor of 3 in the presence of particles. Furthermore, when charge is dispersed across large volumes, discharge may be controlled by mechanisms that are not present at smaller scales. On Earth, for example, the electric fields in lightning-producing clouds rarely, if ever, exceed values of 10^5 Vm^{-1} (corrected for altitude) which is one order of magnitude smaller than the conventional breakdown field of 3×10^6 Vm^{-1} (Marshall et al., 1995) (Schroeder et al., 1999) (Solomon et al., 2001) (Dwyer, 2005). In these regimes, the initiation of discharges in clouds may not be controlled by the dielectric breakdown of the gas, but by a runaway electron avalanche (e.g. Gurevich, Milikh, and Roussel-Dupre, 1992 Dwyer, 2005 Dwyer and Uman, 2014). Runaway electrons are produced when the electric field in a charged particle cloud is strong enough give electrons generated by cosmic rays the energy needed to overcome the losses associ-

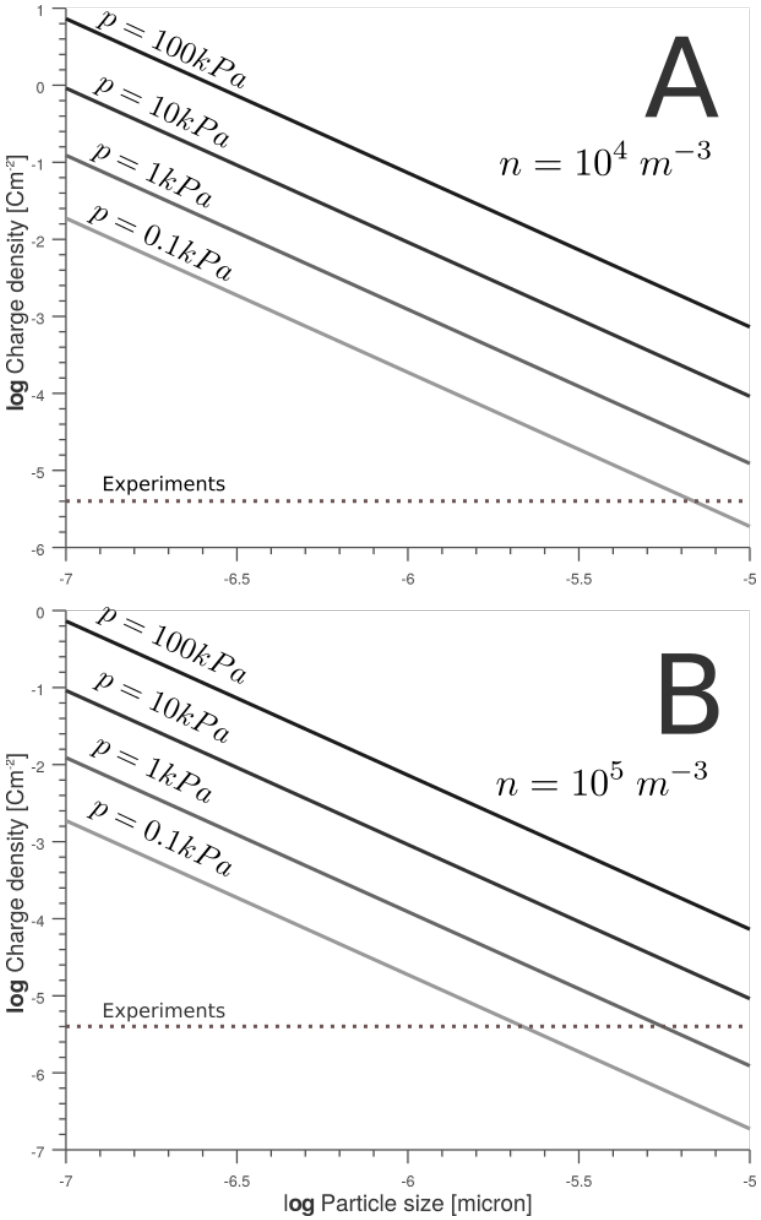

Figure 9.7: Charge densities on particles required to produce the breakdown field at the edge of a 10 km-wide cloud as a function of particle size and pressure for a hydrogen environment. A) $n = 10^4 m^{-3}$. B) $n = 10^5 m^{-3}$. The horizontal dotted line represent the maximum charge densities observed in our experiments.

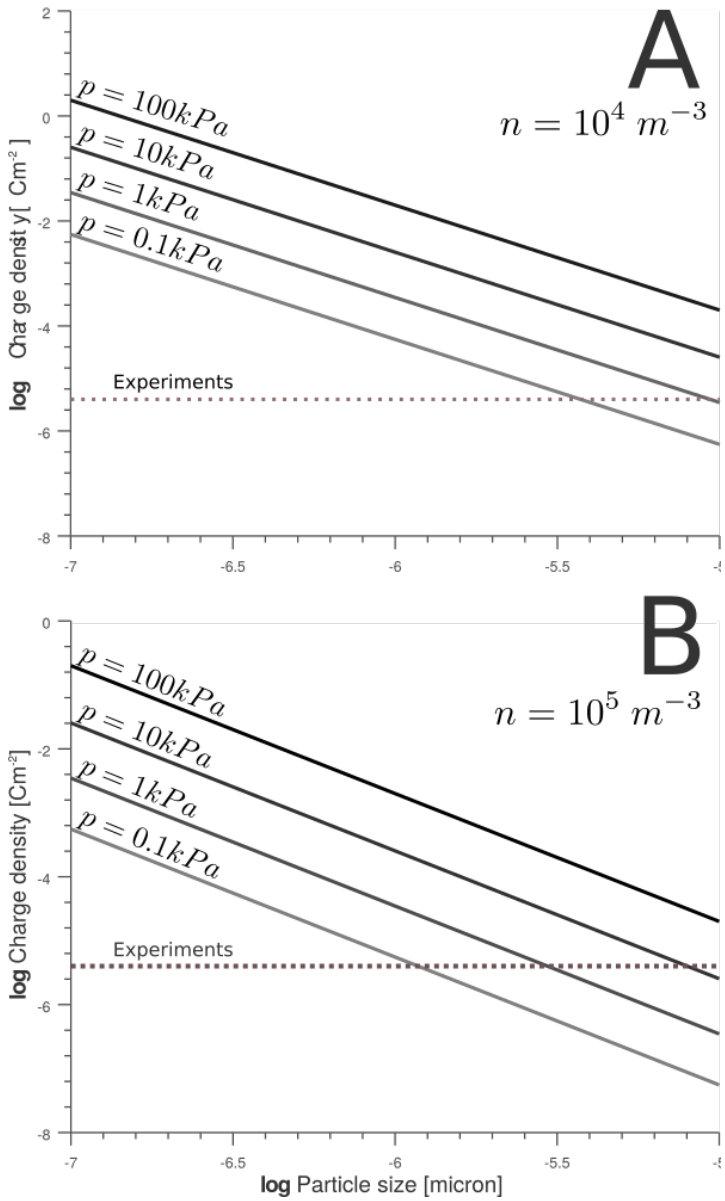

Figure 9.8: Charge densities on particles required to produce the breakdown field at the edge of a 10 km-wide cloud as a function of particle size and pressure for a helium environment. A) $n = 10^4 m^{-3}$. B) $n = 10^5 m^{-3}$. The horizontal dotted line represent the maximum charge densities observed in our experiments.

ated with collisions and accelerate them to relativistic speeds. These electrons then collide with neutrals to generate more electrons that eventually lead to breakdown. In terrestrial environments, similar processes are likely to occur in other large-scale multiphase systems such as volcanic plumes and dust storms (McNutt & Williams, 2010). If such mechanisms are active in the clouds of GJ1214b, putative salt grains are not require to carry charge densities as high as the Paschen limit to produce large spark discharges. However, outside of this discussion, such considerations are beyond the scope of this work.

9.5 Conclusions

Given the electrical diversity observed in our own solar system, an exoplanent with a dynamic, particle-bearing atmosphere (such as that inferred to exist on GJ1214b) will almost certainly be characterized by complex electrostatic processes (Helling et al., 2013) (Vorgul & Helling, 2016). In this work, we have characterized the triboelectric behavior of potassium chloride and zinc sulfide under temperatures relevant to GJ1214b. The charge densities observed in our experiments are consistent with those measured on lightning-producing volcanic ash particles. Furthermore, we showed that the charge densities on grains may result in electric fields which exceed the breakdown limit under certain conditions. Together, these results provide further evidence that electrified salt grains in the atmosphere of GJ1214b could drive discharge processes. Whether or not such activity can be detected on an exosolar object remains contentious subject. Lightning on worlds with charged, dusty atmospheres may be detected through excess radio emissions observed during transit (Vorgul & Helling, 2016), or through abnormal spectral signals modulated by lightning-induced disequilibrium chemistry (Bailey, Helling, Hodosan, Bilger, & Stark, 2014) (Xue, Yuan, Cen, Li, & Wang, 2015). Hodosan, Helling, Asensio-Torres, Vorgul, and Rimmer, 2016 has suggested that a world's daytime spectrum could be cross-correlated with

known lightning spectra to infer the presence of large-scale discharges. Yet, even for a world with an extremely high flash-rate, such signals may be too small to be detected even with a state-of-the-art instrument like James Webb Space Telescope(Ardaseva et al., 2017). Definite detection of electrostatic processes may have to wait until the next generation of telescopes such as the European Extremely Large Telescope.

CHAPTER 10
FUTURE WORK

The work present in this thesis has been purely experimental. Moving forward, I plan to compliment these experiments with both field campaigns and numerical modeling.

10.1 Field work

To explore electrification in volcanic plumes using a robust, long-term sensor network combining both stationary electric field sensors and in-situ probes. The two components of the system are the *Ad-hoc Network for high Density Electric field Studies of Igneous Thunderstorms in Eruptions* (ANDESITE) and the *Three-axis Electric Field sensor for Re-enty Applications* (TEFRA). ANDESITE is composed of twenty sensor nodes placed in close proximity to an eruptive vent. Each node will harbor a custom-built electric field mill, a three-axis Honeywell magnetometer, and a particle detector to measure the charge on individual particles falling out of the plume (described in Mendez Harper and Dufek, 2016). The instruments are wireless and use ZigBee (based on IEEE 802.15.4) enabled radios to transmit data back and receive commands from a base station. These sensors can be rapidly deployed either by hand or can be delivered to their locations using drones. The field mill in each node uses a novel reciprocating design to conserve power and reduce mechanical wear and, thus, can be run off small solar panels. Once these nodes are deployed, they can be operated remotely for years. Designed and constructed in-house, I have tested their operation at the Tonaltépetl volcano in M exico. The ground-based measurements will be complimented with TEFRA, a probe designed for in-situ plume measurements. The device consists of a 15 cm aluminum sphere containing 6 miniature electric field mills lying on orthogonal axes (Figure 10.1) and can be dropped through a plume from an aircraft or drone. The total ambient field, E_T, surrounding the probe can be

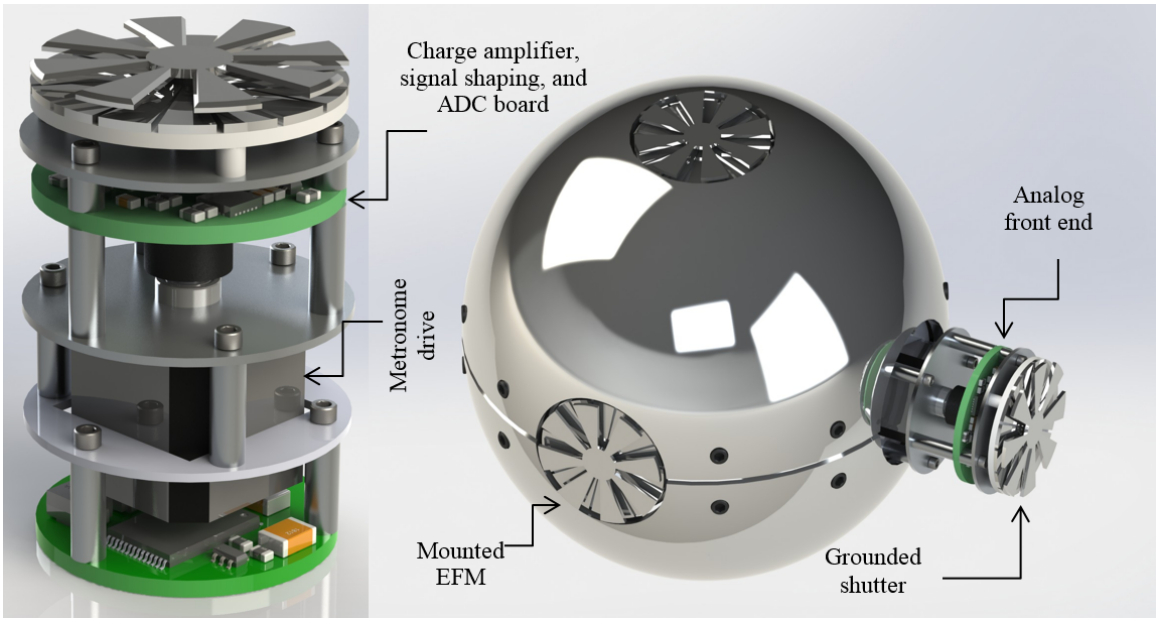

Figure 10.1: Digital rendition of the TEFRA probe. Left panel: Individual field mill sensor. Right panel: Integrated probe

determined from the electric fields measurements, E'_x , E_x ,E'_y ,E_y ,E'_z ,E_z , taken by the six orthogonal field mills as:

$$E_T = 1/6[(E_x - E'_x)^2 + (E_y - E'_y)^2 + (E_z - E'_z)^2]^(1/2) \tag{10.1}$$

Furthermore, the charge deposited on the probe as it falls through the charged plume can also be determined:

$$Q = 1/6[(E_x + E_x) + (E_y + E_y) + (E_z + E_z)] \times 4\pi\epsilon_o R_s^2 \tag{10.2}$$

Fiber optic sensors passed through small apertures in the sensors hull allow the size and concentration of particles surrounding the sensor to be computed. Humidity and temperature sensors will assess the weather inside of the plume and a three-axis magnetometer will make measurements of the ambient magnetic field. An inertial measurement unit with six degrees of freedom (composed of 3-axis accelerometer and 3-axis gyroscope) and a GPS unit allow the orientation and position of the sphere to

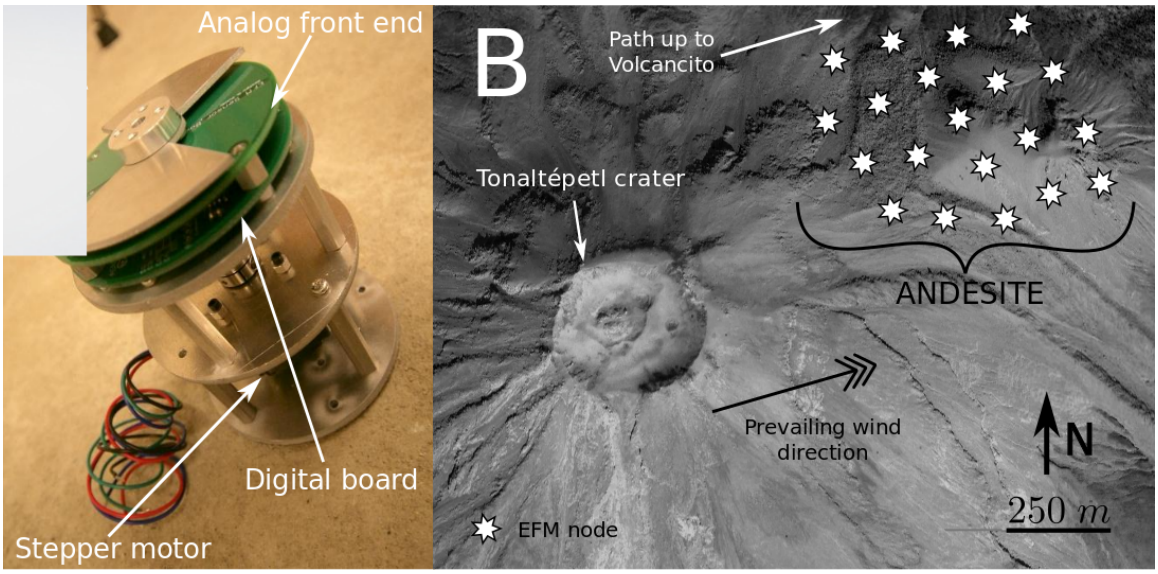

Figure 10.2: A) Single ANDESITE electric field mill without weather-proof casing. B) ANDESITE concept of operations.

be determined as it falls through the ash-laden cloud. While the system is not recoverable, data is transmitted to a base station using a wireless 900 MHz link as the probe falls through the plume. Furthermore, the system is inexpensive, costing less than 500 USD, and multiple units can be readily produced. The TEFRA measurements will represent the first in-situ studies of charging in proximal volcanic plumes Studies with ANDESITE and TEFRA will conducted at the Tonaltpetl (Fuego de Colima) volcano in Xalixco and Colliman, México. Tonaltépetl is a small stratovolcano at the western terminus of the Trans-Mexican Volcanic Belt. It represents an ideal place to study electrification of ash given that it erupts between 5-10 times a day, often produces lightning, and is only a two hour drive from Guadalajara, a major Mexican city. Additionally, Tonaltépetl is a very well instrumented volcano, allowing me to collect complimentary geophysical data, including seismic, infrasonic, and thermal, as well as facilitating the emplacement of a base station to receive wireless data from ANDESITE and TEFRA. Furthermore, I have worked closely with the faculty of la Universidad de Colima (Dr. Nick Varley) responsible for monitoring the mountain.

The concept of operations for the network deployment is shown in Figure 10.2.

ANDESITE nodes will be deployed on a parasitic dome called Volcanito 1 km ENE and 400 m below of Tonaltépetls crater. Volcancitos summit is relatively flat and has an approximate area of 25000 m^2, allowing us to place sensors on a regular grid. The dome can be easily accessed from service road that runs along the northern tallus of Tonaltépetl. During the winter months, winds carry volcanic material of the dome. As the plume flows over the network, nodes will detect variations in the electric field. Because large particles are believed to carry positive charge and these heavier grains fall out of the plume close to the vent, we expect sensors downstream to detect a progressively more negative plume. Data from sensors will be transmitted to an internet-enabled base station located in the volcano observatory run by the Universidad de Colima a kilometer north of Volcancito. Each TEFRA unit will be dropped from a small aircraft flying over the volcanic plume. Four probes will be deployed per eruption.

10.2 Numerical Modelling

The second phase of this project consists of integrating constituent relationships from experimental efforts into a large-scale volcanic plume model to quantitatively relate particle dynamics, varying water contents, and environmental conditions to electrification and the generation of lightning . The model is a modified version of the open-source Multiphase Flow with Interphase eXchanges (MFIX) developed by the American National Energy and Technology Lab to simulate evolving particle concentration, thermal environment, and physical dynamics in volcanic plumes (Syamlal, 1994). The code follows an eularian-eularian-lagrangian approach. This means that gas, volatiles, and small particle phases are treated as inter-penetrating media, although each have their own momentum and energy equations (eulerian-eularian aspect). The ash phase approximates particles generated both from the initial fragmentation event as well as those generated by post fragmentation conduit processes.

The solid eularian phase is representative of particles with diameters of 100 microns and Stoke numbers on the order of 0.1. The particle and gas phases are two-way coupled by drag forces. Large clasts such as bombs are treated as discrete particles (lagrangian) and are tracked throughout the simulation. The model can also account for a stratified atmosphere with varying degrees of water content. This plume model is optimized to run on high-performance architectures and has been run on large clusters such as the NSCA Blue Waters Supercomputer. Although individual collisions between particles in the ash (small-particle) phase cannot be resolved in the model, kinetic theory can be used to estimate parameters such a granular temperature and collisions rates. This information can then be employed in conjunction with the charging rates extracted from experiments. Knowing the charge structure of the plume will allow us to compute perturbation to the ambient electric field. This output can then be compared to field studies conducted around active volcanoes with lightning. Furthermore, we will integrate the plume model with atmospheric lightning model of Riousset, Pasko, Krehbiel, Thomas, and Rison, 2007). The lightning model uses the electric field calculated from EEL simulations. This coupled model will be used to study two large eruptions that displayed copious amounts of electrical activity: Mount Redoubt (2009) and Eyjafjallajokull (2010). Detailed descriptions of these volcanoes electrical storms can be found in a number of recent publications. These two eruptions were also chosen due to the relative abundance of satellite observations, ash sampling and modern atmospheric data associated with them. Such information will help constrain the inputs to the model. Secondly, previous computational efforts at Georgia Tech have already produced working simulations of these eruptions (without the electrostatic microphysics and not coupled to the lightning model) which will serve as templates for the proposed work.

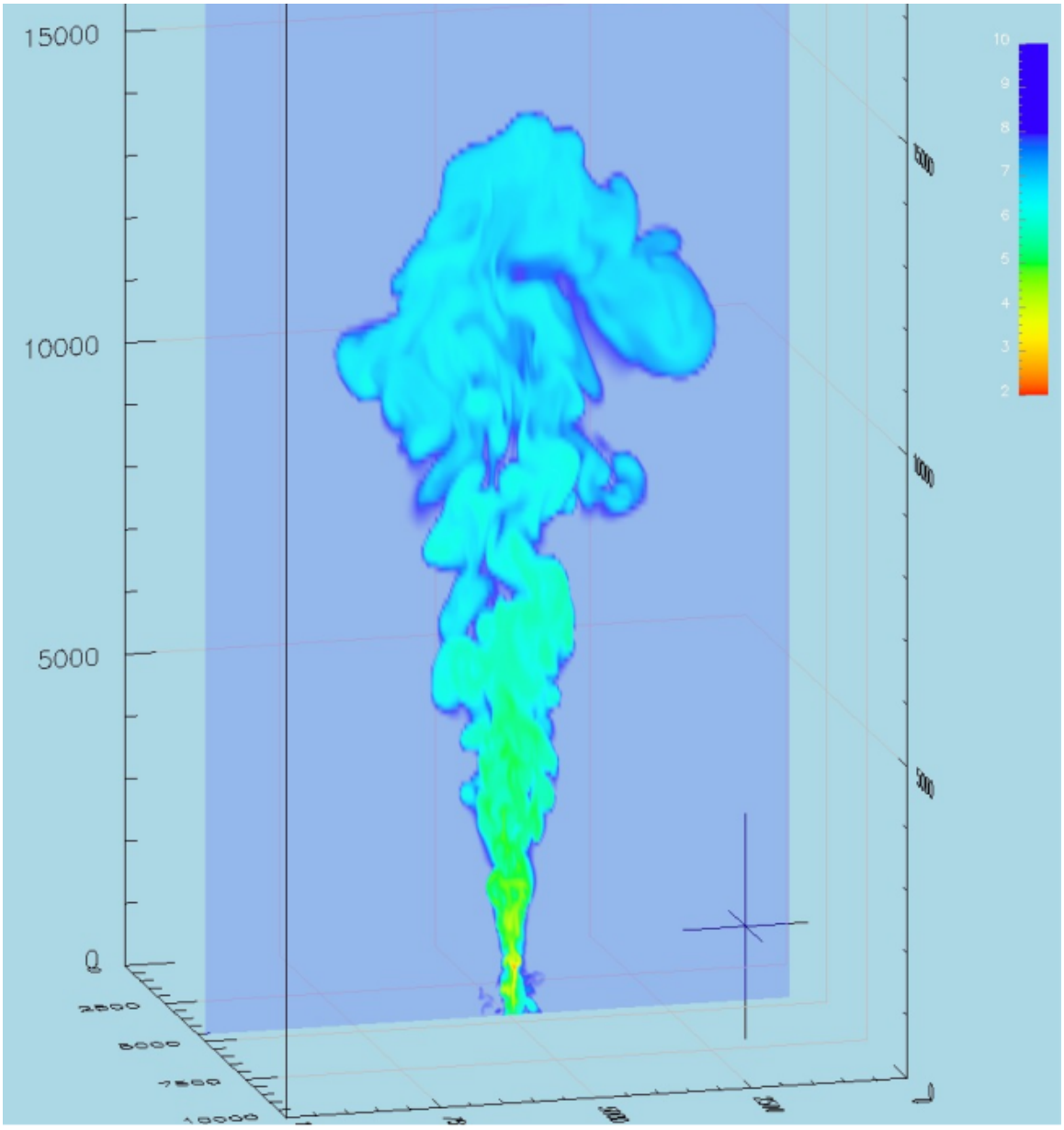

Figure 10.3: Output of multiphase model showing particle concentration

REFERENCES

Abbas, M., Tankosic, D., Craven, P., Spann, J., LeClair, A., & West, E. (2007). Lunar dust charging by photoelectric emissions. *Planetary and Space Science*, *55*(7), 953–965.

Adamson, T. C. & Nicholls, J. A. (1959). On the Structure of Jets from Highly Underexpanded Nozzles Into Still Air. *Journal of the Aerospace Sciences*, *26*(1), 16–24.

Aizawa, K., Cimarelli, C., Alatorre-Ibarguengoitia, M. A., Yokoo, A., Dingwell, D. B., & Iguchi, M. (2016). Physical properties of volcanic lightning: Constraints from magnetotelluric and video observations at Sakurajima volcano, Japan. *Earth and Planetary Science Letters*, *444*, 45–55.

Apodaca, M. M., Wesson, P. J., Bishop, K. J., Ratner, M. A., & Grzybowski, B. A. (2010). Contact electrification between identical materials. *Angewandte Chemie*, *122*(5), 958–961.

Al-Arainy, A., Malik, N., & Qureshi, M. (1994). Influence of sand/dust contamination on the breakdown of asymmetrical air gaps under switching impulses. *IEEE transactions on dielectrics and electrical insulation*, *1*(2), 305–314.

Arason, P., Bennett, A. J., & Burgin, L. E. (2011). Charge mechanism of volcanic lightning revealed during the 2010 eruption of Eyjafjallajokull. *Journal of Geophysical Research: Solid Earth*, *116*(B9), B00C03.

Ardaseva, A., Rimmer, P. B., Waldmann, I., Rocchetto, M., Yurchenko, S. N., Helling, C., & Tennyson, J. (2017). Lightning chemistry on earth-like exoplanets. *arXiv preprint arXiv:1704.07917*.

Bailey, R., Helling, C., Hodosan, G., Bilger, C., & Stark, C. R. (2014). Ionization in atmospheres of brown dwarfs and extrasolar planets vi: Properties of large-scale discharge events. *The Astrophysical Journal*, *784*(1), 43.

Baquedano, E. (2015). *Tezcatlipoca: Trickster and supreme deity*. University Press of Colorado.

Barnes, J. W., Brown, R. H., Soderblom, L., Sotin, C., Le Mouelic, S., Rodriguez, S., ... Nicholson, P. (2008). Spectroscopy, morphometry, and photoclinometry of titan's dunefields from Cassini/VIMS. *Icarus*, *195*(1), 400–414.

Bartknecht, W. (2012). *Dust explosions: Course, prevention, protection*. Springer Science & Business Media.

Bartnikas, R. (1990). Detection of partial discharges (Corona) in electrical apparatus. *IEEE Transactions on Electrical Insulation*, *25*(1), 111–124.

Baytekin, H. T., Patashinski, A. Z., Branicki, M., Baytekin, B., Soh, S., & Grzybowski, B. A. (2011). The Mosaic of Surface Charge in Contact Electrification. *Science*, *333*(6040), 308–312.

Behnke, S. A. & Bruning, E. C. (2015). Changes to the turbulent kinematics of a volcanic plume inferred from lightning data. *Geophysical Research Letters*, *42*(10).

Behnke, S. A., Thomas, R. J., Krehbiel, P. R., & McNutt, S. R. (2012). Spectacular lightning revealed in 2009 Mount Redoubt eruption. *Eos, Transactions American Geophysical Union*, *93*(20), 193–194.

Behnke, S. A., Thomas, R. J., McNutt, S. R., Schneider, D. J., Krehbiel, P. R., Rison, W., & Edens, H. E. (2013). Observations of volcanic lightning during the 2009 eruption of Redoubt Volcano. *Journal of Volcanology and Geothermal Research*. The 2009 Eruption of Redoubt Volcano, Alaska, *259*, 214–234.

Bichoutskaia, E., Boatwright, A. L., Khachatourian, A., & Stace, A. J. (2010). Electrostatic analysis of the interactions between charged particles of dielectric materials. *The Journal of Chemical Physics*, *133*(2), 024105.

Bilici, M. A., Toth, J. R., Sankaran, R. M., & Lacks, D. J. (2014). Particle size effects in particle-particle triboelectric charging studied with an integrated fluidized bed and electrostatic separator system. *Review of Scientific Instruments*, *85*(10), 103903.

Bonnefoy, L. E., Hayes, A. G., Hayne, P. O., Malaska, M. J., Le Gall, A., Solomonidou, A., & Lucas, A. (2016). Compositional and spatial variations in Titan dune and interdune regions from Cassini VIMS and RADAR. *Icarus*. Titan's Surface and Atmosphere, *270*, 222–237.

Burgo, T. A., Rezende, C. A., Bertazzo, S., Galembeck, A., & Galembeck, F. (2011). Electric potential decay on polyethylene: Role of atmospheric water on electric charge build-up and dissipation. *Journal of electrostatics*, *69*(4), 401–409.

Burr, D. M., Bridges, N. T., Marshall, J. R., Smith, J. K., White, B. R., & Emery, J. P. (2015). Higher-than-predicted saltation threshold wind speeds on Titan. *Nature*, *517*(7532), 60–63.

Cable, M. L., Horst, S. M., Hodyss, R., Beauchamp, P. M., Smith, M. A., & Willis, P. A. (2011). Titan tholins: Simulating titan organic chemistry in the cassini-huygens era. *Chemical Reviews*, *112*(3), 1882–1909.

Carey, P. (1989). *Oscar & lucinda*. ISIS large print books. Harper & Row.

Carter, B. J. (1992). Size and stress gradient effects on fracture around cavities. *Rock Mechanics and Rock Engineering*, *25*(3), 167–186.

Castellanos, A. (2005). The relationship between attractive interparticle forces and bulk behaviour in dry and uncharged fine powders. *Advances in Physics*, *54*, 263–376.

Chandrasekar, S. & Chaudhri, M. (1994). The explosive disintegration of prince rupert's drops. *Philosophical Magazine B*, *70*(6), 1195–1218.

Chang, J.-S., Kelly, A. J., & Crowley, J. M. (1995). *Handbook of electrostatic processes*. CRC Press.

Charbonneau, D., Berta, Z. K., Irwin, J., Burke, C. J., Nutzman, P., Buchhave, L. A., ... Udry, S., et al. (2009). A super-earth transiting a nearby low-mass star. *Nature*, *462*(7275), 891–895.

Charnay, B., Barth, E., Rafkin, S., Narteau, C., Lebonnois, S., Rodriguez, S., ... Lucas, A. (2015). Methane storms as a driver of titan's dune orientation. *Nature Geoscience*, *8*(5), 362–366.

Charnay, B., Meadows, V., Misra, A., Leconte, J., & Arney, G. (2015). 3d modeling of gj1214b's atmosphere: Formation of inhomogeneous high clouds and observational implications. *The Astrophysical Journal Letters*, *813*(1), L1.

Chaudhri, M. M. (2009). The role of residual stress in a prince rupert's drop of soda-lime glass undergoing a self-sustained and stable destruction/fracture wave. *physica status solidi (a)*, *206*(7), 1410–1413.

Chen, Z., Liu, F., Wang, L., Li, Y., Wang, R., & Chen, Z. (2014). Tribocharging properties of wheat bran fragments in air–solid pipe flow. *Food research international*, *62*, 262–271.

CIA. (2016). Distribution of family income - gini index. *CIA - World Factbook*.

Cimarelli, C., Alatorre-Ibarguengoitia, M. A., Aizawa, K., Yokoo, A., Diaz-Marina, A., Iguchi, M., & Dingwell, D. B. (2016). Multiparametric observation of volcanic lightning: Sakurajima Volcano, Japan. *Geophysical Research Letters*, *43*(9), 2015GL067445.

Cimarelli, C., Alatorre-Ibarguengoitia, M. A., Kueppers, U., Scheu, B., & Dingwell, D. B. (2014). Experimental generation of volcanic lightning. *Geology*, *42*(1), 79–82.

Cohen, E. H. (1956). The electric strength of highly compressed gases. *Proceedings of the IEE - Part A: Power Engineering*, *103*(7), 57–68.

Cookson, A. & Farish, O. (1970). Particle initiated breakdown in compressed sf 6. In *Electrical insulation & dielectric phenomena-annual report 1970, conference on* (pp. 179–186). IEEE.

Cross, J. (1987). Electrostatics: Principles, problems and applications.

Dascalescu, L., Samuila, A., & Tobazeon, R. (1996). Dielectric behaviour of particle-contaminated air-gaps in the presence of corona. *Journal of electrostatics*, *36*(3), 253–275.

Delitsky, M. L. & McKay, C. P. (2010). The photochemical products of benzene in Titan's upper atmosphere. *Icarus*, *207*(1), 477–484.

Deng, H., He, Z., Xu, Y., Ma, J., Liu, J., & Guo, R. (2010). An investigation on two-phase mixture discharges: The effects of macroparticle sizes. *Journal of Physics D: Applied Physics*, *43*(25), 255203.

Dickinson, J. T., Jensen, L. C., & Jahan-Latibari, A. (1984). Fractoemission: The role of charge separation. *Journal of Vacuum Science & Technology A*, *2*(2), 1112–1116.

Dickinson, J. T., Langford, S. C., Jensen, L. C., McVay, G. L., Kelso, J. F., & Pantano, C. G. (1988). Fractoemission from fused silica and sodium silicate glasses. *Journal of Vacuum Science & Technology A*, *6*(3), 1084–1089.

Dickinson, J., Donaldson, E., & Park, M. (1981). The emission of electrons and positive ions from fracture of materials. *Journal of Materials Science*, *16*(10), 2897–2908.

Donaldson, E. E., Dickinson, J. T., & Wu, N. (1990). Fractemission-induced electrical breakdown in vacuum. *IEEE Transactions on Electrical Insulation*, *25*(3), 549–556.

Dufek, J., Manga, M., & Patel, A. (2012). Granular disruption during explosive volcanic eruptions. *Nature Geoscience*, *5*(8), 561–564.

Duff, N. & Lacks, D. J. (2008). Particle dynamics simulations of triboelectric charging in granular insulator systems. *Journal of Electrostatics*, *66*(1-2), 51–57.

Dwyer, J. R. (2005). The initiation of lightning by runaway air breakdown. *Geophysical Research Letters*, *32*(20), L20808.

Dwyer, J. R. & Uman, M. A. (2014). The physics of lightning. *Physics Reports*. The Physics of Lightning, *534*(4), 147–241.

Dyudina, U., Ingersoll, A., Danielson, G., Baines, K., Carlson, R., NIMS, T. G., & Teams, S. (2001). Interpretation of nims and ssi images on the jovian cloud structure. *Icarus*, *150*(2), 219–233.

Enomoto, Y. & Chaudhri, M. M. (1993). Fractoemission during fracture of engineering ceramics. *Journal of the American Ceramic Society*, *76*(10), 2583–2587.

Farrell, W. M., McLain, J. L., Collier, M. R., Keller, J. W., Jackson, T. J., & Delory, G. T. (2015). Is the electron avalanche process in a martian dust devil self-quenching? *Icarus*, *254*, 333–337.

Finkelstein, D., Hill, R., & Powell, J. R. (1973). The piezoelectric theory of earthquake lightning. *Journal of Geophysical Research*, *78*(6), 992–993.

Forbes. (2016). Anne cox chambers - the richest person in america's 50 largest cities. *Forbes Profiles*.

Forward, K. M., Lacks, D. J., & Sankaran, R. M. (2009a). Charge Segregation Depends on Particle Size in Triboelectrically Charged Granular Materials. *Physical Review Letters*, *102*(2), 028001.

Forward, K. M., Lacks, D. J., & Sankaran, R. M. (2009b). Particle-size dependent bipolar charging of Martian regolith simulant. *Geophysical Research Letters*, *36*(13), L13201.

Forward, K. M., Lacks, D. J., & Sankaran, R. M. (2009c). Triboelectric Charging of Granular Insulator Mixtures Due Solely to Particle-Particle Interactions. *Industrial & Engineering Chemistry Research*, *48*(5), 2309–2314.

Forward, K. M., Lacks, D. J., & Sankaran, R. M. (2009d). Triboelectric charging of lunar regolith simulant. *Journal of Geophysical Research: Space Physics*, *114*(A10), A10109.

Galembeck, F., Burgo, T. A. L., Balestrin, L. B. S., Gouveia, R. F., Silva, C. A., & Galembeck, A. (2014). Friction, tribochemistry and triboelectricity: Recent progress and perspectives. *4*(109), 64280–64298.

Gao, P. & Benneke, B. (2016). Microphysics of kcl and zns clouds on gj 1214 b. In *Aas/division for planetary sciences meeting abstracts* (Vol. 48).

Gao, X., Narteau, C., & Rozier, O. (2016). Controls on and effects of armoring and vertical sorting in aeolian dune fields: A numerical simulation study. *Geophysical Research Letters*, *43*(6), 2016GL068416.

Genareau, K., Wardman, J. B., Wilson, T. M., McNutt, S. R., & Izbekov, P. (2015). Lightning-induced volcanic spherules. *Geology*, *43*(4), 319–322.

Gilbert, J. S., Lane, S. J., Sparks, R. S. J., & Koyaguchi, T. (1991). Charge measurements on particle fallout from a volcanic plume. *Nature*, *349*(6310), 598–600.

Glor, M., Lüttgens, G., Maurer, B., & Post, L. (1989). Discharges from bulked polymeric granules during the filling of silos-characterization b by measurements and influencing factors. *Journal of Electrostatics*, *23*, 35–43.

Gonzalez, A. C. & Pantano, C. G. (1990). Fractoemission during crack propagation in glass. *Applied Physics Letters*, *57*(3), 246–248.

Greason, W. D. (2000). Investigation of a test methodology for triboelectrification. *Journal of Electrostatics*, *49*(3-4), 245–256.

Grzybowski, B. A., Winkleman, A., Wiles, J. A., Brumer, Y., & Whitesides, G. M. (2003). Electrostatic self-assembly of macroscopic crystals using contact electrification. *Nature Materials*, *2*(4), 241–245.

Gu, Z., Wei, W., Su, J., & Yu, C. W. (2013). The role of water content in triboelectric charging of wind-blown sand. *Scientific Reports*, *3*, 1337.

Gurevich, A. V., Milikh, G. M., & Roussel-Dupre, R. (1992). Runaway electron mechanism of air breakdown and preconditioning during a thunderstorm. *Physics Letters A*, *165*(5), 463–468.

Hamamoto, N., Nakajima, Y., & Sato, T. (1992). Experimental discussion on maximum surface charge density of fine particles sustainable in normal atmosphere. *Journal of Electrostatics*, *28*(2), 161–173.

Hamelin, M., Lethuillier, A., Le Gall, A., Grard, R., Beghin, C., Schwingenschuh, K., ... Ciarletti, V. (2016). The electrical properties of Titan's surface at the Huygens landing site measured with the PWA-HASI Mutual Impedance Probe. New approach and new findings. *Icarus*. Titan's Surface and Atmosphere, *270*, 272–290.

Harrison, R. G., Nicoll, K. A., Ulanowski, Z., & Mather, T. A. (2010). Self-charging of the Eyjafjallajokull volcanic ash plume. *Environmental Research Letters*, *5*(2), 024004.

Harrison, R., Aplin, K., Leblanc, F., & Yair, Y. (2008). Planetary atmospheric electricity. *Space Science Reviews*, *137*(1), 5–10.

Hasegawa, T. & Takeuchi, M. (2000). Effects of particle size and atmosphere on tribocharging of polymer powders. In *Nip & digital fabrication conference* (Vol. 2000, *2*, pp. 723–726). Society for Imaging Science and Technology.

Hatakeyama, H. (1947). On the Variation of the Atmospheric Potential Gradient caused by the Cloud of Smoke of the Volcano Asama. (The Fourth Report.) *Journal of the Meteorological Society of Japan. Ser. II*, *25*(1-3), 39–39.

Hatakeyama, H. & Uchikawa, K. (1951). On the Disturbance of the Atmospheric Potential Gradient caused by the Eruption-smoke of the Volcano Aso. *Papers in Meteorology and Geophysics*, *2*(1), 85–89.

He, C. & Smith, M. A. (2013). Identification of nitrogenous organic species in titan aerosols analogs: Nitrogen fixation routes in early atmospheres. *Icarus*, *226*(1), 33–40.

Helling, C., Jardine, M., Stark, C., & Diver, D. (2013). Ionization in Atmospheres of Brown Dwarfs and Extrasolar Planets. III. Breakdown Conditions for Mineral Clouds. *The Astrophysical Journal*, *767*(2), 136.

Helling, C., Rimmer, P., Rodriguez-Barrera, I., Wood, K., Robertson, G., & Stark, C. R. (2016). Ionisation and discharge in cloud-forming atmospheres of brown dwarfs and extrasolar planets. *Plasma Physics and Controlled Fusion*, *58*(7), 074003.

Hendrickson, G. (2006). Electrostatics and gas phase fluidized bed polymerization reactor wall sheeting. *Chemical Engineering Science*, *61*(4), 1041–1064.

Herzog, M., Graf, H.-F., Textor, C., & Oberhuber, J. M. (1998). The effect of phase changes of water on the development of volcanic plumes. *Journal of Volcanology and Geothermal Research*, *87*(1), 55–74.

Hodosan, G., Helling, C., Asensio-Torres, R., Vorgul, I., & Rimmer, P. B. (2016). Lightning climatology of exoplanets and brown dwarfs guided by solar system data. *Monthly Notices of the Royal Astronomical Society*, *461*(4), 3927–3947.

Hogue, M. D., Calle, C. I., Weitzman, P. S., & Curry, D. R. (2008). Calculating the trajectories of triboelectrically charged particles using discrete element modeling (dem). *Journal of Electrostatics*, *66*(1), 32–38.

Horenstein, M. N., Mazumder, M., & Sumner Jr., R. C. (2013). Predicting particle trajectories on an electrodynamic screen - Theory and experiment. *Journal of*

Electrostatics. Journal of ELECTROSTATICS, Electrostatics 2013 12th International Conference on Electrostatics, *71*(3), 185–188.

Horn, R. G., Smith, D., & Grabbe, A. (1993). Contact electrification induced by monolayer modification of a surface and relation to acid–base interactions.

Horwell, C. J. (2007). Grain-size analysis of volcanic ash for the rapid assessment of respiratory health hazard. *Journal of Environmental Monitoring*, *9*(10), 1107–1115.

Houghton, I. M. P., Aplin, K. L., & Nicoll, K. A. (2013). Triboelectric Charging of Volcanic Ash from the 2011 Gr\'{\i}msv\otn Eruption. *Physical Review Letters*, *111*(11), 118501.

Imanaka, H. & Smith, M. A. (2010). Formation of nitrogenated organic aerosols in the titan upper atmosphere. *Proceedings of the National Academy of Sciences*, *107*(28), 12423–12428.

Ireland, P. M. (2007). The role of changing contact in sliding triboelectrification. *Journal of Physics D: Applied Physics*, *41*(2), 025305.

Ireland, P. M. (2009). Contact charge accumulation and separation discharge. *Journal of Electrostatics*, *67*(2), 462–467.

Iuga, A., Calin, L., Neamtu, V., Mihalcioiu, A., & Dascalescu, L. (2005). Tribocharging of plastics granulates in a fluidized bed device. *Journal of Electrostatics*, *63*(6), 937–942.

Iversen, J. D. & White, B. R. (1982). Saltation threshold on Earth, Mars and Venus. *Sedimentology*, *29*(1), 111–119.

James, M. R., Gilbert, J. S., & Lane, S. J. (2002). Experimental investigation of volcanic particle aggregation in the absence of a liquid phase. *Journal of Geophysical Research: Solid Earth*, *107*(B9), 2191.

James, M. R., Lane, S. J., & Gilbert, J. S. (2000). Volcanic plume electrification: Experimental investigation of a fracture-charging mechanism. *Journal of Geophysical Research: Solid Earth*, *105*(B7), 16641–16649.

James, M. R., Lane, S. J., & Gilbert, J. S. (2003). Density, construction, and drag coefficient of electrostatic volcanic ash aggregates. *Journal of Geophysical Research: Solid Earth*, *108*(B9), 2435.

James, M. R., Lane, S., & Gilbert, J. (1998). Specialvolcanic plume monitoring using atmospheric electric potential gradients. *Journal of the Geological Society*, *155*(4), 587–590.

James, M., Wilson, L., Lane, S., Gilbert, J., Mather, T., Harrison, R., & Martin, R. (2008). Electrical charging of volcanic plumes. In *Planetary atmospheric electricity* (pp. 399–418). Springer.

Jones, T. B. & Tang, K.-M. (1987). Charge relaxation in powder beds. *Journal of electrostatics*, *19*(2), 123–136.

Kanazawa, S., Ohkubo, T., Nomoto, Y., & Adachi, T. (1995). Electrification of a pipe wall during powder transport. *Journal of electrostatics*, *35*(1), 47–54.

Keithley. (2004). *6th Edition Keithley's Low Level Measurements Handbook*.

Kempton, E. M.-R., Zahnle, K., & Fortney, J. J. (2011). The atmospheric chemistry of gj 1214b: Photochemistry and clouds. *The Astrophysical Journal*, *745*(1), 3.

Kieffer, S. (1981). *Fluid dynamics of the May 18 blast at Mount St. Helens*. U.S. Government Printing Office.

Kikuchi, K. & Endoh, T. (1982). Atmospheric electrical properties of volcanic ash particles in the eruption of Mt. Usu Volcano, 1977. *Journal of the Meteorological Society of Japan*, *1*(60), 548–561.

Kok, J. F. & Lacks, D. J. (2009). Electrification of granular systems of identical insulators. *Physical Review E*, *79*(5), 051304.

Kok, J. F. & Renno, N. O. (2008). Electrostatics in Wind-Blown Sand. *Physical Review Letters*, *100*(1), 014501.

Kok, J. F. & Renno, N. O. (2009). Electrification of wind-blown sand on mars and its implications for atmospheric chemistry. *Geophysical Research Letters*, *36*(5), n/a–n/a. L05202.

Krasnopolsky, V. A. (2009). A photochemical model of titan's atmosphere and ionosphere. *Icarus*, *201*(1), 226–256.

Krasnopolsky, V. A. (2014). Chemical composition of titan's atmosphere and ionosphere: Observations and the photochemical model. *Icarus*, *236*, 83–91.

Krauss, C. E., Horanyi, M., & Robertson, S. (2003). Experimental evidence for electrostatic discharging of dust near the surface of Mars. *New Journal of Physics*, *5*(1), 70.

Kreidberg, L., Bean, J., Desert, J., Benneke, B., Deming, D., Stevenson, K., ... Homeier, D. (2014). Clouds in the atmosphere of the super-earth exoplanet gj 1214b. *Nature*, *505*(7481), 69–72.

Kunkel, W. (1950). The static electrification of dust particles on dispersion into a cloud. *Journal of Applied Physics*, *21*(8), 820–832.

Kwetkus, B., Sattler, K., & Siegmann, H.-C. (1992). Gas breakdown in contact electrification. *Journal of Physics D: Applied Physics*, *25*(2), 139.

Lacanna, G. & Ripepe, M. (2013). Influence of near-source volcano topography on the acoustic wavefield and implication for source modeling. *Journal of Volcanology and Geothermal Research*, *250*, 9–18.

Lacks, D. J. & Levandovsky, A. (2007). Effect of particle size distribution on the polarity of triboelectric charging in granular insulator systems. *Journal of Electrostatics*, *65*(2), 107–112.

Lacks, D. J. & Sankaran, R. M. (2011). Contact electrification of insulating materials. *Journal of Physics D: Applied Physics*, *44*(45), 453001.

Lajtai, E. Z. (1972). Effect of tensile stress gradient on brittle fracture initiation. *International Journal of Rock Mechanics and Mining Sciences & Geomechanics Abstracts*, *9*(5), 569–578.

Lane, S. J. & Gilbert, J. S. (1992). Electric potential gradient changes during explosive activity at Sakurajima volcano, Japan. *Bulletin of Volcanology*, *54*(7), 590–594.

Lang, T. J., Rutledge, S. A., Dolan, B., Krehbiel, P., Rison, W., & Lindsey, D. T. (2013). Lightning in Wildfire Smoke Plumes Observed in Colorado during Summer 2012. *Monthly Weather Review*, *142*(2), 489–507.

Laurentie, J., Traoré, P., & Dascalescu, L. (2013). Discrete element modeling of triboelectric charging of insulating materials in vibrated granular beds. *Journal of Electrostatics*, *71*(6), 951–957.

Lavvas, P., Coustenis, A., & Vardavas, I. (2008). Coupling photochemistry with haze formation in titan's atmosphere, part ii: Results and validation with cassini/huygens data. *Planetary and Space Science*, *56*(1), 67–99.

Le Gall, A., Janssen, M. A., Wye, L. C., Hayes, A. G., Radebaugh, J., Savage, C., ... Farr, T. (2011). Cassini SAR, radiometry, scatterometry and altimetry observations of Titan's dune fields. *Icarus*, *213*(2), 608–624.

Lee, V. & Jaeger, H. (2016). Using acoustic levitation to study tribocharging of submillimeter particles. *Proc. 2016 Electrostatics Joint Conference*.

Lee, V., Waitukaitis, S. R., Miskin, M. Z., & Jaeger, H. M. (2015). Direct observation of particle interactions and clustering in charged granular streams. *Nature Physics*, *11*(9), 733–737.

Liao, C.-C., Hsiau, S.-S., & Huang, T.-Y. (2011). The effect of vibrating conditions on the electrostatic charge in a vertical vibrating granular bed. *Powder technology*, *208*(1), 1–6.

Liu, E. J., Cashman, K. V., Rust, A. C., & Gislason, S. R. (2015). The role of bubbles in generating fine ash during hydromagmatic eruptions. *Geology*, *43*(3), 239–242.

Lopes, R., Stofan, E., Peckyno, R., Radebaugh, J., Mitchell, K., Mitri, G., ... Lunine, J., et al. (2010). Distribution and interplay of geologic processes on titan from cassini radar data. *Icarus*, *205*(2), 540–558.

Lopes, R. M. C., Malaska, M. J., Solomonidou, A., Le Gall, A., Janssen, M. A., Neish, C. D., ... Lawrence, K. J. (2016). Nature, distribution, and origin of Titan's Undifferentiated Plains. *Icarus*. Titan's Surface and Atmosphere, *270*, 162–182.

Lora, J. M., Lunine, J. I., & Russell, J. L. (2015). GCM simulations of Titan's middle and lower atmosphere and comparison to observations. *Icarus*, *250*, 516–528.

Lorenz, R. D., Wall, S., Radebaugh, J., Boubin, G., Reffet, E., Janssen, M., ... West, R. (2006). The Sand Seas of Titan: Cassini RADAR Observations of Longitudinal Dunes. *Science*, *312*(5774), 724–727.

Lorenz, R. D. (2014). Physics of saltation and sand transport on titan: A brief review. *Icarus*. Third Planetary Dunes Systems, *230*, 162–167.

Lorenz, R. D. & Radebaugh, J. (2009). Global pattern of Titan's dunes: Radar survey from the Cassini prime mission. *Geophysical Research Letters*, *36*(3), L03202.

Lowell, J. & Rose-Innes, A. (1980). Contact electrification. *Advances in Physics*, *29*(6), 947–1023.

Lowell, J. & Truscott, W. S. (1986a). Triboelectrification of identical insulators. I. An experimental investigation. *Journal of Physics D: Applied Physics*, *19*(7), 1273.

Lowell, J. & Truscott, W. S. (1986b). Triboelectrification of identical insulators. II. Theory and further experiments. *Journal of Physics D: Applied Physics*, *19*(7), 1281.

Lucas, A., Narteau, C., Rodriguez, S., Rozier, O., Callot, Y., Garcia, A., & Pont, S. C. d. (2015). Sediment flux from the morphodynamics of elongating linear dunes. *Geology*, *43*(11), 1027–1030.

Lucas, A., Rodriguez, S., Narteau, C., Charnay, B., du Pont, S. C., Tokano, T., ... Aharonson, O. (2014). Growth mechanisms and dune orientation on Titan. *Geophysical Research Letters*, *41*(17), 6093–6100.

Mahi, I. N., Senouci, K., Tilmatine, A., Messafeur, R., Miloua, F., & Dascalescu, L. (2015). Premises of using triboelectric charge for identification of the granular product flowing in a pneumatic transport system. In *Industry applications society annual meeting, 2015 ieee* (pp. 1–6). IEEE.

Malaska, M. J., Lopes, R. M. C., Williams, D. A., Neish, C. D., Solomonidou, A., Soderblom, J. M., ... Turtle, E. P. (2016). Geomorphological map of the Afekan Crater region, Titan: Terrain relationships in the equatorial and mid-latitude regions. *Icarus*. Titan's Surface and Atmosphere, *270*, 130–161.

Malaska, M. J., Lopes, R. M., Hayes, A. G., Radebaugh, J., Lorenz, R. D., & Turtle, E. P. (2016). Material transport map of Titan: The fate of dunes. *Icarus*. Titan's Surface and Atmosphere, *270*, 183–196.

Mammino, J., Johnson, T. F., Walters, D. W., & Perez, S. R. (1980). Electrophotographic carrier powder coated by resin dry-mixing process. US Patent 4,233,387. Google Patents.

Manning, H. L. K., ten Kate, I. L., Battel, S. J., & Mahaffy, P. R. (2010). Electric discharge in the Martian atmosphere, Paschen curves and implications for future missions. *Advances in Space Research*, *46*(10), 1334–1340.

Marshall, T. C., McCarthy, M. P., & Rust, W. D. (1995). Electric field magnitudes and lightning initiation in thunderstorms. *Journal of Geophysical Research: Atmospheres*, *100*(D4), 7097–7103.

Mason, P. (2016). *Postcapitalism: A guide to our future*. Macmillan.

Matsusaka, S., Maruyama, H., Matsuyama, T., & Ghadiri, M. (2010). Triboelectric charging of powders: A review. *Chemical Engineering Science*, *65*(22), 5781–5807.

Matsusaka, S., Ghadiri, M., & Masuda, H. (2000). Electrification of an elastic sphere by repeated impacts on a metal plate. *Journal of Physics D: Applied Physics*, *33*(18), 2311.

Matsusyama, T. & Yamamoto, H. (2006). Impact charging of particulate materials. *Chemical Engineering Science*, *61*(7), 2230–2238.

Matsuyama, T. & Yamamoto, H. (1995). Charge relaxation process dominates contact charging of a particle in atmospheric conditions. *Journal of Physics D: Applied Physics*, *28*(12), 2418.

Matsuyama, T. & Yamamoto, H. (2010). Maximum electrostatic charge of powder in pipe flow. *Advanced Powder Technology*, *21*(3), 350–355.

Mayr, M. & Barringer, S. (2006). Corona compared with triboelectric charging for electrostatic powder coating. *Journal of food science*, *71*(4).

Mazumder, M., Wankum, D., Sims, R., Mountain, J., Chen, H., Pettit, P., & Chaser, T. (1997). Influence of powder properties on the performance of electrostatic coating process. *Journal of Electrostatics*, *40*, 369–374.

McDonald, G. D., Hayes, A. G., Ewing, R. C., Lora, J. M., Newman, C. E., Tokano, T., ... Chen, G. (2016). Variations in Titan's dune orientations as a result of orbital forcing. *Icarus*. Titan's Surface and Atmosphere, *270*, 197–210.

McNutt, S. R., Thompson, G., West, M. E., Fee, D., Stihler, S., & Clark, E. (2013). Local seismic and infrasound observations of the 2009 explosive eruptions of Redoubt Volcano, Alaska. *Journal of Volcanology and Geothermal Research*. The 2009 Eruption of Redoubt Volcano, Alaska, *259*, 63–76.

McNutt, S. R. & Williams, E. R. (2010). Volcanic lightning: Global observations and constraints on source mechanisms. *Bulletin of Volcanology*, *72*(10), 1153–1167.

McNutt, S., Tytgat, G., Estes, S., & Stihler, S. (2010). A Parametric Study of the January 2006 Explosive Eruptions of Augustine Volcano, Alaska, Using Seismic, Infrasonic, and Lightning Data. *U.S. Geological Survey Professional Paper*, 85–102.

Medici, E. F., Allen, J. S., & Waite, G. P. (2014). Modeling shock waves generated by explosive volcanic eruptions. *Geophysical Research Letters*, *41*(2), 414–421.

Mendez Harper, J., Cimarelli, C., Cigala, V., Kueppers, U., Dufek, J., & Gauidin, D. (2017). Differentiating the roles of triboelectric and fractoelectric charging in the generation of volcanic lightning. *Sub.*

Mendez Harper, J. & Dufek, J. (2015). The Electrification of Volcanic Particles during the Brittle Fragmentation of the Magma Column. *Proc. ESA Annual Meeting on Electrostatics 2015*.

Mendez Harper, J. & Dufek, J. (2016). The effects of dynamics on the triboelectrification of volcanic ash. *Journal of Geophysical Research: Atmospheres*, 2015JD024275.

Mendez Harper, J., McDonald, G. D., Dufek, J., Malaska, M. J., Burr, D. M., Hayes, A. G., ... Wray, J. (2017). Electrification of sand on titan and its influence on sediment transport. *Nature Geoscience*.

Merrison, J. P., Gunnlaugsson, H. P., Hogg, M., Jensen, M., Lykke, J., Madsen, M. B., ... Pedersen, R., et al. (2012). Factors affecting the electrification of wind driven dust studied with laboratory simulations. *Planetary and Space Science*, *60*(1), 328–335.

Miura, T., Koyaguchi, T., & Tanaka, Y. (1996). Atmospheric electric potential gradient measurements of ash clouds generated by pyroclastic flows at Unzen Volcano, Japan. *Geophysical Research Letters*, *23*(14), 1789–1792.

Miura, T., Koyaguchi, T., & Tanaka, Y. (2002). Measurements of electric charge distribution in volcanic plumes at sakurajima volcano, japan. *Bulletin of volcanology*, *64*(2), 75–93.

Moore, P. J., Portugues, I., & Glover, I. A. (2003). A nonintrusive partial discharge measurement system based on RF technology. In *2003 IEEE Power Engineering Society General Meeting (IEEE Cat. No.03ch37491)* (Vol. 2, 633 Vol. 2).

Moughrabiah, W. O., Grace, J. R., & Bi, X. T. (2012). Electrostatics in gas–solid fluidized beds for different particle properties. *Chemical engineering science*, *75*, 198–208.

Mountain, J. R., Mazumder, M. K., Sims, R. A., Wankum, D. L., Chasser, T., & Pettit, P. (2001). Triboelectric charging of polymer powders in fluidization and transport processes. *IEEE Transactions on Industry Applications*, *37*(3), 778–784.

Murtomaa, M., Rasanen, E., Rantanen, J., Bailey, A., Laine, E., Mannermaa, J.-P., & Yliruusi, J. (2003). Electrostatic measurements on a miniaturized fluidized bed. *Journal of electrostatics*, *57*(1), 91–106.

Nagata, T., Sakuma, S., & Fukushima, N. (1948). On the lava flow newly ejected from sakurajima volcano.

Ndama, A. T., Guigon, P., & Saleh, K. (2011). A reproducible test to characterise the triboelectric charging of powders during their pneumatic transport. *Journal of Electrostatics*, *69*(3), 146–156.

Nicora, M. G., Burgesser, R. E., Rosales, A., Quel, E. J., & Avila, E. E. (2013). Actividad electrica asociada a la erupcion del complejo volcanico Cordon Caulle durante 2011. *www.scielo.ar*.

Niemann, H. B., Atreya, S. K., Demick, J. E., Gautier, D., Haberman, J. A., Harpold, D. N., ... Raulin, F. (2010). Composition of Titan's lower atmosphere and simple surface volatiles as measured by the Cassini-Huygens probe gas chromatograph mass spectrometer experiment. *Journal of Geophysical Research: Planets*, *115*(E12), E12006.

Nomura, T., Satoh, T., & Masuda, H. (2003). The environment humidity effect on the tribo-charge of powder. *Powder Technology*, *135*, 43–49.

Ogden, D. E., Wohletz, K. H., Glatzmaier, G. A., & Brodsky, E. E. (2008). Numerical simulations of volcanic jets: Importance of vent overpressure. *Journal of Geophysical Research: Solid Earth*, *113*(B2), B02204.

Ohsawa, A. (2003). Computer simulation for assessment of electrostatic hazards in filling operations with powder. *Powder technology*, *135*, 216–222.

Olivier, G. (2003). *Mockeries and metamorphoses of an aztec god: Tezcatlipoca, lord of the smoking mirror*. University Press of Colorado.

Orescanin, M. M. & Austin, J. M. (2010). Exhaust of Underexpanded Jets from Finite Reservoirs. *Journal of Propulsion and Power*, *26*(4), 744–753.

Orescanin, M. M., Austin, J. M., & Kieffer, S. W. (2010). Unsteady high-pressure flow experiments with applications to explosive volcanic eruptions. *Journal of Geophysical Research: Solid Earth*, *115*(B6), B06206.

Owen, P. & Thornhill, C. (1948). The flow in an axially symmetric supersonic jet from a nearly sonic orifice into a vacuum. *Ministry of Supply, Armament Research Establishment, Physical Research Division*.

Pahtz, T., Herrmann, H. J., & Shinbrot, T. (2010). Why do particle clouds generate electric charges? *Nature Physics*, *6*(5), 364–368.

Park, S. K. (1996). Precursors to earthquakes: Seismoelectromagnetic signals. *Surveys in Geophysics*, *17*(4), 493–516.

Paschen, F. (1889). Ueber die zum Funkenubergang in Luft, Wasserstoff und Kohlensaure bei verschiedenen Drucken erforderliche Potentialdifferenz. *Annalen der Physik*, *273*(5), 69–96.

Pei, C., Wu, C.-Y., England, D., Byard, S., Berchtold, H., & Adams, M. (2013). Numerical analysis of contact electrification using dem–cfd. *Powder technology*, *248*, 34–43.

Piketty, T., Goldhammer, A., & Ganser, L. (2014). Capital in the twenty-first century.

Pliny The Younger, P. t. (1963). *The Letters of the Younger Pliny* (Reissue edition) (B. Radice, Trans.). Penguin Classics.

Ponczek, S. & Lu, W. (2016). The 10 most unequal cities in america. *Bloomberg Markets*.

Pont, F., Knutson, H., Gilliland, R., Moutou, C., & Charbonneau, D. (2008). Detection of atmospheric haze on an extrasolar planet: The 0.55–1.05 μm transmission spectrum of hd 189733b with the hubble space telescope. *Monthly Notices of the Royal Astronomical Society*, *385*(1), 109–118.

Pont, S. C. d., Narteau, C., & Gao, X. (2014). Two modes for dune orientation. *Geology*, *42*(9), 743–746.

Radebaugh, J., Lorenz, R. D., Lunine, J. I., Wall, S. D., Boubin, G., Reffet, E., ... Team, t. C. R. (2008). Dunes on Titan observed by Cassini Radar. *Icarus*, *194*(2), 690–703.

Raizer, Y. P. (2011). *Gas Discharge Physics*. Springer Berlin Heidelberg.

Read, P. (2011). Saturn: Storm-clouds brooding on towering heights. *Nature*, *475*(7354), 44–45.

Reid, A. J., Judd, M. D., Fouracre, R. A., Stewart, B. G., & Hepburn, D. M. (2011). Simultaneous measurement of partial discharges using IEC60270 and radio-frequency techniques. *IEEE Transactions on Dielectrics and Electrical Insulation*, *18*(2), 444–455.

Revel, J., Gatumel, C., Dodds, J. A., & Taillet, J. (2003). Generation of static electricity during fluidisation of polyethylene and its elimination by air ionisation. *Powder Technology*, *135*, 192–200.

Rinnert, K., Lanzerotti, L., Uman, M., Dehmel, G., Gliem, F., Krider, E., & Bach, J. (1998). Measurements of radio frequency signals from lightning in jupiter's atmosphere. *Journal of Geophysical Research: Planets*, *103*(E10), 22979–22992.

Riousset, J. A., Pasko, V. P., Krehbiel, P. R., Thomas, R. J., & Rison, W. (2007). Three-dimensional fractal modeling of intracloud lightning discharge in a New Mexico thunderstorm and comparison with lightning mapping observations. *Journal of Geophysical Research: Atmospheres*, *112*(D15), D15203.

Rodriguez, S., Garcia, A., Lucas, A., Appere, T., Le Gall, A., Reffet, E., ... Turtle, E. P. (2014). Global mapping and characterization of Titan's dune fields with Cassini: Correlation between RADAR and VIMS observations. *Icarus*. Third Planetary Dunes Systems, *230*, 168–179.

Rubin, D. M. & Hesp, P. A. (2009). Multiple origins of linear dunes on Earth and Titan. *Nature Geoscience*, *2*(9), 653–658.

Schroeder, V., Baker, M., & Latham, J. (1999). A model study of corona emission from hydrometeors. *Quarterly Journal of the Royal Meteorological Society*, *125*(557), 1681–1693.

Schwindt, N., von Pidoll, U., Markus, D., Klausmeyer, U., Papalexandris, M., & Grosshans, H. (2017). Measurement of electrostatic charging during pneumatic conveying of powders. *Journal of Loss Prevention in the Process Industries*.

Shao, Y. & Lu, H. (2000). A simple expression for wind erosion threshold friction velocity. *Journal of Geophysical Research: Atmospheres*, *105*(D17), 22437–22443.

Shaw, P. (1917). Experiments on tribo-electricity. i. the tribo-electric series. *Proceedings of the Royal Society of London. Series A, Containing Papers of a Mathematical and Physical Character*, *94*(656), 16–33.

Shinbrot, T., Komatsu, T. S., & Zhao, Q. (2008). Spontaneous tribocharging of similar materials. *EPL (Europhysics Letters)*, *83*(2), 24004.

Sickafoose, A., Colwell, J., Horanyi, M., & Robertson, S. (2001). Experimental investigations on photoelectric and triboelectric charging of dust. *Journal of Geophysical Research: Space Physics*, *106*(A5), 8343–8356.

Sing, D. K., Desert, J.-M., Des Etangs, A. L., Ballester, G., Vidal-Madjar, A., Parmentier, V., ... Henry, G. (2009). Transit spectrophotometry of the exoplanet hd 189733b-i. searching for water but finding haze with hst nicmos. *Astronomy and Astrophysics*, *505*(2), 891–899.

Soares, L. C., Bertazzo, S., Burgo, T. A., Baldim, V., & Galembeck, F. (2008). A new mechanism for the electrostatic charge build-up and dissipation in dielectrics. *Journal of the Brazilian Chemical Society*, *19*(2), 277–286.

Soderblom, L. A., Kirk, R. L., Lunine, J. I., Anderson, J. A., Baines, K. H., Barnes, J. W., ... Wall, S. D. (2007). Correlations between cassini vims spectra and radar sar images: Implications for titan's surface composition and the character of the huygens probe landing site. *Planetary and Space Science*. Titan as seen from Huygens, *55*(13), 2025–2036.

Solomon, R., Schroeder, V., & Baker, M. (2001). Lightning initiation–conventional and runaway-breakdown hypotheses. *Quarterly Journal of the Royal Meteorological Society*, *127*(578), 2683–2704.

Sowinski, A., Miller, L., & Mehrani, P. (2010). Investigation of electrostatic charge distribution in gas-solid fluidized beds. *Chemical Engineering Science*, *65*(9), 2771–2781.

Stace, A. J., Boatwright, A. L., Khachatourian, A., & Bichoutskaia, E. (2011). Why like-charged particles of dielectric materials can be attracted to one another. *Journal of Colloid and Interface Science*, *354*(1), 417–420.

Stentman, D. (2004). Electrical Breakdown Parameters for Neutral Atmospheres of the Solar System. *ISUAL Workshop Proc.*

Syamlal, M. (1994). *Mfix Documentation: User's Manual* (tech. rep. No. DOE/METC–95/1013). EG and G Technical Services of West Virginia, Inc., Morgantown, WV (United States).

Symons, G. J. (J., Judd, J. W. (W., Strachey, R., Wharton, W. J. L. (J. L., Evans, F. J. (J., Russell, F. A. R., ... Whipple, G. M. (1888). *The eruption of Krakatoa, and subsequent phenomena*. London, Trubner & co.

Tada, Y. & Murata, Y. (1995). Direct charge leakage through humid air. *Japanese journal of applied physics*, *34*(4R), 1926.

Takahashi, S., Kobayashi, N., & Yamazaki, T. (1990). Triboelectrification and toner surface-charge density in the two-component development system of electrophotography. *Triboelectrification and toner surface-charge density in the two-component development system of electrophotography*.

Takeuchi, A. & Nagahama, H. (2002). Interpretation of charging on fracture or frictional slip surface of rocks. *Physics of the Earth and Planetary Interiors*, *130*(3-4), 285–291.

Takeuchi, A., Nagahama, H., & Hashimoto, T. (2004). Surface electrification of rocks and charge trapping centers. *Physics and Chemistry of the Earth, Parts A/B/C*, *29*(4), 359–366.

Taube, K. A. (1992). Art, ideology, and the city of teotihuacan. In *Art, ideology, and the city of teotihuacan: A symposium at dumbarton oaks, 8th and 9th october 1988* (p. 169). Dumbarton Oaks.

Telko, M. J., Kujanpaa, J., & Hickey, A. J. (2007). Investigation of triboelectric charging in dry powder inhalers using electrical low pressure impactor (elpi). *International journal of pharmaceutics*, *336*(2), 352–360.

Telling, J. & Dufek, J. (2012). An experimental evaluation of ash aggregation in explosive volcanic eruptions. *Journal of Volcanology and Geothermal Research*, *209-210*, 1–8.

Telling, J., Dufek, J., & Shaikh, A. (2013). Ash aggregation in explosive volcanic eruptions. *Geophysical Research Letters*, *40*(10), 2355–2360.

Thomas, A., Saleh, K., Guigon, P., & Czechowski, C. (2009). Characterisation of electrostatic properties of powder coatings in relation with their industrial application. *Powder Technology*. Selection of Papers from the Symposium Powder Science and Technology - Powders and Sintered Material STP-PMF 2007Symposium on Powder Science and Technology - Powders and Sintered Material STP-PMF 2007, *190*(1-2), 230–235.

Thomas, R. J., Krehbiel, P. R., Rison, W., Edens, H. E., Aulich, G. D., Winn, W. P., ... Clark, E. (2007). Electrical Activity During the 2006 Mount St. Augustine Volcanic Eruptions. *Science*, *315*(5815), 1097–1097.

Tokano, T. (2010). Relevance of fast westerlies at equinox for the eastward elongation of Titan's dunes. *Aeolian Research*, *2*(2-3), 113–127.

Van Eaton, A. R., Amigo, a., Bertin, D., Mastin, L. G., Giacosa, R. E., Gonzalez, J., ... Behnke, S. A. (2016). Volcanic lightning and plume behavior reveal evolving hazards during the april 2015 eruption of calbuco volcano, chile. *Geophysical Research Letters*, *43*(7), 2016GL068076.

Vorgul, I. & Helling, C. (2016). Flash ionization signature in coherent cyclotron emission from brown dwarfs. *Monthly Notices of the Royal Astronomical Society*, *458*(1), 1041–1056.

Waite, J. H., Young, D. T., Cravens, T. E., Coates, A. J., Crary, F. J., Magee, B., & Westlake, J. (2007). The Process of Tholin Formation in Titan's Upper Atmosphere. *Science*, *316*(5826), 870–875.

Waitukaitis, S. R., Lee, V., Pierson, J. M., Forman, S. L., & Jaeger, H. M. (2014). Size-dependent same-material tribocharging in insulating grains. *Physical Review Letters*, *112*(21), 218001.

Warwick, J., Evans, D., Romig, J., Alexander, J., Desch, M., Kaiser, M., ... Pedersen, B. (1982). Planetary radio astronomy observations from voyager 2 near saturn. *Science*, *215*(4532), 582–587.

Watanabe, H., Samimi, A., Ding, Y. L., Ghadiri, M., Matsuyama, T., & Pitt, K. G. (2006). Measurement of Charge Transfer due to Single Particle Impact. *Particle & Particle Systems Characterization*, *23*(2), 133–137.

Williams, D. A., Radebaugh, J., Lopes, R. M., & Stofan, E. (2011). Geomorphologic mapping of the menrva region of titan using cassini radar data. *Icarus*, *212*(2), 744–750.

Woodhouse, M. J. & Behnke, S. A. (2014). Charge structure in volcanic plumes: A comparison of plume properties predicted by an integral plume model to observations of volcanic lightning during the 2010 eruption of Eyjafjallajokull, Iceland. *Bulletin of Volcanology*, *76*(8).

Xie, L., Bao, N., Jiang, Y., & Zhou, J. (2016). Effect of humidity on contact electrification due to collision between spherical particles. *AIP Advances*, *6*(3), 035117.

Xue, S., Yuan, P., Cen, J., Li, Y., & Wang, X. (2015). Spectral observations of a natural bipolar cloud-to-ground lightning. *Journal of Geophysical Research: Atmospheres*, *120*(5), 1972–1979.

Yair, Y. (2008). Charge generation and separation processes. In *Planetary atmospheric electricity* (pp. 119–131). Springer.

Yao, J., Zhang, Y., Wang, C.-H., Matsusaka, S., & Masuda, H. (2004). Electrostatics of the granular flow in a pneumatic conveying system. *Industrial & engineering chemistry research*, *43*(22), 7181–7199.

Yao, W., He, Z., Deng, H., Li, J., & Li, J. (2011). Experimental investigation of two-phase mixture discharges under dc voltage from effects of macroparticle sizes. *IEEE Transactions on Plasma Science*, *39*(3), 856–864.

Yokoo, A., Suzuki, Y. J., & Iguchi, M. (2014). Dual infrasound sources from a vulcanian eruption of sakurajima volcano inferred from cross array observation. *Seismological Research Letters*, *85*(6), 1212–1222.

Zarka, P., Farrell, W., Fischer, G., & Konovalenko, A. (2008). Ground-based and space-based radio observations of planetary lightning. *Space Science Reviews*, *137*(1-4), 257–269.

Zhao, H., Castle, G. P., Inculet, I. I., & Bailey, A. G. (2003). Bipolar charging of polydisperse polymer powders in fluidized beds. *IEEE Transactions on Industry Applications*, *39*(3), 612–618.

VITA

Joshua Méndez was born in the Federal District, capital of the United Mexican States. He was raised in San Mateo Oxtotitlan, a suburb Tollocan (State of México) by Meredith Harper and Austreberto Méndez Iturbide, musicians at the National Autonomous University of México's Philharmonic Orchestra. Josh attended high school at the Instituto Tecnológico y de Estudios Superiores de Monterrey, where he was first exposed to engineering concepts. Graduating high school, he moved to Boston to pursue a degree in electrical engineering at Boston University. In 2011, Josh relocated to Atlanta to complete a PhD in Geophysics and Ms in electrical and computer engineering at the Georgia Institute of Technology.